

Naval Research Laboratory

Washington, DC 20375-5000



2

NRL Memorandum Report 6817

**AD-A234 390**

**X-Ray Laser Program Final Report for FY 90**

*Radiation Hydrodynamics Branch and Pulsed Power Physics Branch  
Plasma Physics Division*

April 18, 1991

This work was supported by the Strategic Defense Initiative Organization under  
Job Title, Ultra Short Wavelength Laser Research

Approved for public release; distribution unlimited.

# REPORT DOCUMENTATION PAGE

Form Approved  
OMB No. 0704-0188

Public reporting burden for this collection of information is estimated to average 1 hour per response, including the time for reviewing instructions, searching existing data sources, gathering and maintaining the data needed, and completing and reviewing the collection of information. Send comments regarding this burden estimate or any other aspect of this collection of information, including suggestions for reducing this burden, to Washington Headquarters Services, Directorate for Information Operations and Reports, 1215 Jefferson Davis Highway, Suite 1204, Arlington, VA 22202-4302, and to the Office of Management and Budget, Paperwork Reduction Project (0704-0188), Washington, DC 20503

<b>1. AGENCY USE ONLY (Leave blank)</b>		<b>2. REPORT DATE</b> 1991 April 18	<b>3. REPORT TYPE AND DATES COVERED</b> Interim 10-01-89 - 09/30/90	
<b>4. TITLE AND SUBTITLE</b>  X-Ray Laser Program Final Report for FY 90			<b>5. FUNDING NUMBERS</b>  Program Element No. 63220C	
<b>6. AUTHOR(S)</b>  Listed in individual chapters				
<b>7. PERFORMING ORGANIZATION NAME(S) AND ADDRESS(ES)</b>  Naval Research Laboratory Code 4720 and 4770 Washington, D. C. 20375-5000			<b>8. PERFORMING ORGANIZATION REPORT NUMBER</b>  NRL Memorandum Report 6817	
<b>9. SPONSORING / MONITORING AGENCY NAME(S) AND ADDRESS(ES)</b>  Strategic Defense Initiative Organization T/IS Washington, D. C. 20301-7100			<b>10. SPONSORING / MONITORING AGENCY REPORT NUMBER</b>	
<b>11. SUPPLEMENTARY NOTES</b>  This work was supported by the Strategic Defense Initiative Organization under Job Title, Ultra Short Wavelength Laser Research.				
<b>12a. DISTRIBUTION / AVAILABILITY STATEMENT</b>  Approved for public release; distribution unlimited.			<b>12b. DISTRIBUTION CODE</b>	
<b>13. ABSTRACT (Maximum 200 words)</b>  This report details the progress achieved by the Radiation Hydrodynamics and Pulsed Power Physics Branches in X-Ray Laser experiments and modeling during FY 90. It is divided into five sections whose authors are separately identified. Topics presented in detail include resonant photoexcitation experiments and modeling, pumping kinetics, and plasma uniformity for neonlike lasers, and use of ultrashort driver laser pulses to produce gain in the x-ray region. Principal accomplishments are summarized in the Executive Program Summary.				
<b>14. SUBJECT TERMS</b>  X-Ray Laser Population inversion			<b>15. NUMBER OF PAGES</b> 153	
			<b>16. PRICE CODE</b>	
<b>17. SECURITY CLASSIFICATION OF REPORT</b>  Unclassified		<b>18. SECURITY CLASSIFICATION OF THIS PAGE</b>  Unclassified	<b>19. SECURITY CLASSIFICATION OF ABSTRACT</b>  Unclassified	<b>20. LIMITATION OF ABSTRACT</b>

TABLE OF CONTENTS

Executive Program Summary ..... iv

I. Calculations of Photoionization, Photoexcitation, and Gain  
Production in a Neon Gas Cell Irradiated by a Sodium Z-Pinch  
on Saturn ..... 1

II. NRL Experimental Pulsed Power X-Ray Laser Program ..... 8

III. Improving Plasma Uniformity in Z-Pinch Driven Neonlike Krypton  
X-Ray Lasers ..... 67

IV. Analysis of Pumping Mechanisms Significantly Affecting the Gain  
of Soft X-Ray Lines in Neonlike Selenium ..... 109

V. Prospects for X-Ray Lasing in Ultra Short-Pulse Laser/Plasma  
Interactions ..... 139

A-1

## EXECUTIVE PROGRAM SUMMARY

This NRL Memorandum Report presents in detail the research accomplishments of the Radiation Hydrodynamics and Pulsed Power Physics Branches of the Plasma Physics Division during Fiscal Year 1990. It is divided into five sections whose individual authors are identified at the beginning of each section.

During FY 90, several landmark achievements were recorded in the development of the sodium-neon photoresonant laser system. In this scheme the alpha resonance line of heliumlike Na at  $11 \text{ \AA}$  (Na He- $\alpha$ ) pumps the 1-4 transition in heliumlike neon (Ne He- $\gamma$ ), leading to inversion and possible gain in some 4-3 and 4-2 lines of Ne IX. For the first time, sufficient pump power for gain and inversion (100-200 GW in Na He- $\alpha$ ) has been achieved- and on two separate devices. On the 3-MA-current Double Eagle generator at Physics International Corporation, powers of  $> 100$  GW in the pump line were obtained. NRL personnel from both Branches were heavily involved in this effort. During this past year, we initiated a collaboration with Sandia National Laboratories, which with its 10-MA Saturn generator possesses the world's most powerful Z pinch driver. At Sandia, pump powers near 200 GW were consistently produced on Saturn. Furthermore, time integrated spectra of a neon gas cell located 2 cm from the pumping sodium pinch plasma have provided very persuasive evidence of not only photopumping and fluorescence but an actual population inversion in the neon. If confirmed during FY 91, this accomplishment constitutes the first achievement of population inversion in a Z pinch, and possibly the first x-ray population inversion ever achieved by photopumping. It is doubly significant in that the neon gas cell contains no current and the design therefore eliminates the troublesome problem of current-driven instabilities ruining the lasing medium. NRL's work with Sandia is described in Section I, and the collaborative effort with Physics International in Section II.

In this dual component radiation-pumped x-ray laser, the conditions and properties of the laser medium are of equal importance to the pumping capabilities of the driving sodium pinch. The Pulsed Power Physics Branch has conducted a careful effort to characterize the neon medium using a test stand at NRL, and this work is detailed in Appendix B of Section II.

As mentioned above, the presence of instabilities in current driven pinches seriously complicates their use as lasing media. If this difficulty could be surmounted, powerful, long lived neonlike x-ray lasers would become feasible in these plasmas. Section III presents a detailed study of the possible use of plasma mixtures to radiatively stabilize krypton gas puff pinches, possibly leading to a neonlike krypton soft x-ray laser. It is concluded that the mixing of helium with krypton would be useful in high-current pinches which implode relatively massive loads. Since the specific radiative cooling rate is reduced by inclusion of a low-atomic-number element, the lower compression yields more moderate densities favorable to inversion and gain.

Laboratory x-ray lasers have existed since 1984, and neonlike ions, which naturally lase on the  $3p-3s$  transitions, have proven to be perhaps the most robust atomic system for obtaining gain in the soft x-ray spectral region. Ten neonlike ions from atomic number 28 (nickel) to 47 (silver) have exhibited gain in linear laser-driven plasmas. However, after six years of intensive experimental and theoretical work, the relative magnitudes of the gains in the various laser lines are at best partially understood. In Section IV, a new and important contribution to this ongoing effort examines in detail all the atomic processes affecting the gain coefficients. It is shown that the metastable  $3d$  levels greatly affect the pumping of the  $J=2$  levels, whereas the  $J=0$  upper laser levels are very sensitive to the ground state collisional excitation rates. By increasing the  $3d$  populations and reducing the direct ground state collisional excitation rates, the gains are modified to much closer agreement with experiment.

The final section of this report concentrates on one of the newest and most exciting areas of physics directly relevant to the development of ultrashort wavelength lasers. The recent deployment of powerful subpicosecond driver lasers at several laboratories has enabled the production of plasmas whose departure from equilibrium is extreme. In Section V, the feasibility of obtaining recombination-pumped gain in the  $3-2$  transition of hydrogenic fluorine is examined with radiation-hydrodynamics models. It is found that gain is produced in narrow regions of space and time dominated by low temperatures and densities. This favorable initial investigation is being augmented with an expanded atomic model for a more thorough mapping of the gain regions.

Calculations of Photoionization, Photoexcitation, and Gain Production in  
a Neon Gas Cell Irradiated by a Sodium Z-Pinch on Saturn

J. P. Apruzese, R. W. Clark, and J. Davis

Naval Research Laboratory  
Washington, D. C. 20375-5000 USA

and

J. L. Porter, R. B. Spielman, M. K. Matzen, S. F. Lopez, J. S. McGurn,  
L. E. Ruggles, M. Vargas, D. K. Derzon, T. W. Hussey, and E. J. McGuire

Sandia National Laboratories  
Albuquerque, New Mexico 87185 USA

ABSTRACT: The sodium-neon resonantly photopumped system is one of the most attractive possibilities for development of a photon pumped soft x-ray laser. Using a one-dimensional self-consistent radiation hydrodynamics model the time-dependent temperature, density, ionization state, and gain for a neon gas cell exposed to an intense sodium Z-pinch is calculated. Time-integrated K shell neon spectra obtained on Saturn at Sandia National Laboratories show strong evidence of photopumping.

## 1. INTRODUCTION

The existence of x-ray lines whose wavelength coincides to about a Doppler width provides a potentially promising path to the realization of a photopumped x-ray laser. One of the most attractive of these coincidences is the resonance between the  $1s^2-1s2p\ ^1P_1$  line of Na X (Na He- $\alpha$ ) and the  $1s^2-1s4p\ ^1P_1$  line of Ne IX (Ne He- $\gamma$ ). These 11 Å (1127 eV) lines coincide to about 2 parts in  $10^4$ , Ne He- $\gamma$  being the more energetic by 0.24 eV. The usefulness of this resonance was pointed out by Vinogradov et al (1975) and the conditions required for pumping and gain have been analyzed in detail (Hagelstein 1981, 1983; Apruzese et al 1982, 1985, 1987). The principal requirement for the sodium component is that the pump line power be maximized. For the neon lasant, the number of ions in the pumped heliumlike ground state should be maximized, collisional excitation to the lower laser levels minimized, and density should be sufficient for gain without quenching the inversion. Typically  $T_e = 50-100$  eV with electron densities around  $10^{19}$  cm $^{-3}$  provide such conditions for neon. Since a hotter, denser sodium plasma is needed to maximize pump line power, spatially separate sodium and neon components are necessary. The pumped 4p singlet level of Ne IX quickly redistributes population to 4d and 4f via electron collisions. The line most readily amplified is the 4f-3d singlet transition at 231 Å.

## 2. PUMP LINE POWER

It is obviously important that the sodium He  $\alpha$  pump power be maximized. To this end, experiments have been conducted with both laser plasmas (Hagelstein 1983; Matthews et al 1983) and pulsed-power driven sodium-bearing Z-pinchs. The power of the Na He- $\alpha$  line emitted from Z-pinchs (to  $4\pi$  steradians) has varied from 25 GW on the Naval Research Laboratory's Gamble-II generator at a current of 1 MA (Young et al 1987; Stephanakis et al 1988) to 100-150 GW at 3 MA on the Double-EAGLE device at Physics International Corp. (Deeney et al 1990; Young et al 1990). Recently pump line powers near 200 GW

have been consistently achieved at 10 MA on the world's most powerful Z-pinch driver, Saturn, at Sandia National Laboratories. Saturn's parameters and capabilities have been described by Spielman et al (1989). The analyses of Apruzese et al (1982, 1985, 1987) imply that pump line powers of 100-200 GW are required to achieve unity gain at  $231 \text{ \AA}$  in a neon laser plasma separated by 2-4 cm from the sodium pinch. The actual gain achieved, of course, depends on the detailed properties of the neon plasma. The remainder of this paper is devoted to an analysis of the sodium-neon x-ray laser experiments performed on the Saturn accelerator.

### 3. EXPERIMENTS AND ANALYSIS

The sodium-neon configuration on Saturn is illustrated in Figure 1. A neon gas cell is situated outside the return current path, 2 cm from the sodium wire pinch. To eliminate the problem of plasma instabilities in the laser, no current is driven through the neon, which is to be ionized to the heliumlike stage by the broadband radiation from the pinch and resonantly pumped by the 200 GW Na He- $\alpha$  line. The pinch emits approximately 10 TW

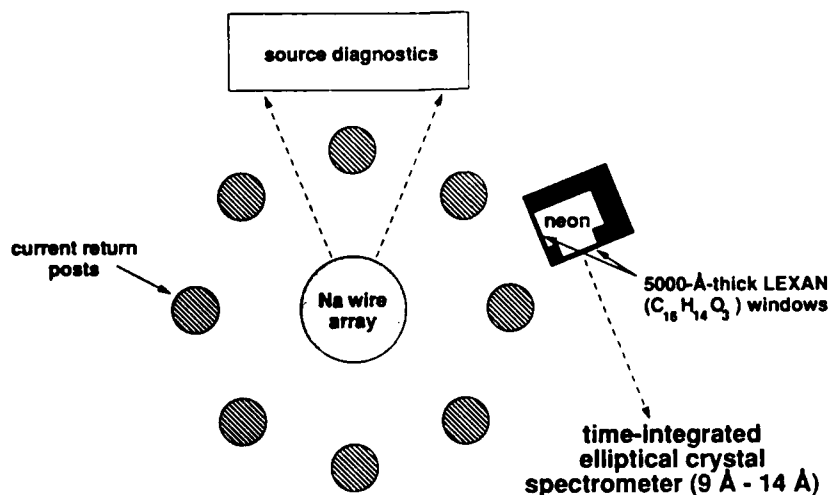


Fig. 1. Experimental configuration for sodium-neon resonant photopumping on Saturn.

peak total x-ray power, in a full-width-half-maximum (FWHM) of 35 ns. Most of this radiation is sub-keV photons, and this broadband component is modeled as a 94 eV blackbody (which would radiate 10 TW from a 2 mm diameter 2 cm length pinch). The only spectral lines assumed incident on the neon are the Na He- $\alpha$  transition (200 GW) and Na Ly- $\alpha$  (400 GW). The lines are taken as Gaussian in time with 20 ns FWHM, whose peak power coincides with that of the continuum. The source of the pure sodium pinch is an array of extruded wires as described by Deeney et al (1990). In the simulation, the sodium radiation is diluted to account for the 2 cm Na/Ne separation, and the response of the neon is calculated using the one-dimensional planar self-consistent radiation-hydrodynamics model described by Duston et al (1983). The neon atomic model includes 29 levels and 52 lines concentrated in Ne VIII, IX and X.

The calculations show that the 0.5  $\mu\text{m}$ -thick plastic window explodes and compresses the neon. An initial fill density of  $4 \times 10^{17}$  neon atoms/cm<sup>3</sup> was chosen to prevent excessive densities in the compressed region at the peak of the sodium radiation pulse. The state of the neon at the radiative peak is given in Figure 2. Even though temperatures of just 10-35 eV prevail, most of the neon is in the heliumlike ground state due to photoionization by the intense soft x-ray radiation produced by Saturn. The compressional heating and density raise are evident between 0.25 and 0.50 cm in Figure 2. Gain in the 4f-3d singlet transition at 231  $\text{\AA}$  is predicted at  $2 \text{ cm}^{-1}$  for a Na He- $\alpha$  linewidth of 8 m $\text{\AA}$ , expected from the combination of opacity and Doppler broadening. The pumped transition, Ne He- $\gamma$ , is calculated as 40% brighter than the usually more intense He- $\beta$  line.

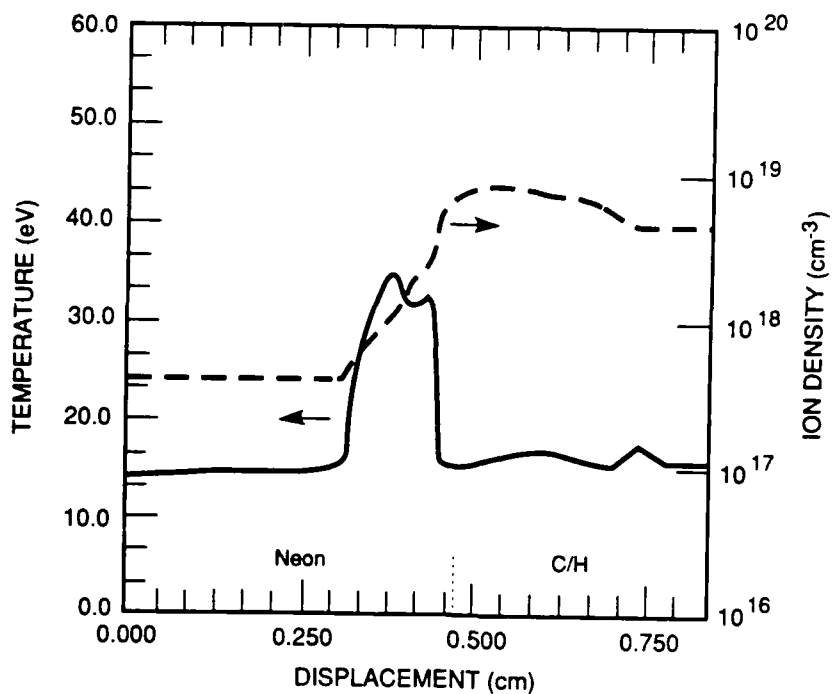


Fig. 2. Neon temperature and ion density are plotted vs. position in the gas cell at the peak of the sodium radiation pulse. Sodium photons are incident from the right.

Strong evidence for resonant photopumping has been obtained in several time-integrated spectra obtained at Sandia from an elliptical crystal spectrometer that looks only at the neon. A typical spectrum (Porter et al 1990) is presented in Figure 3 showing the  $\gamma$  line brighter than  $\beta$ , as predicted by the calculation. Moreover, neon spectra obtained by irradiating the neon gas cell with a Mg Z pinch, where no photoresonance exists, invariably show a more normal pattern where the Ne IX lines diminish in brightness with increasing quantum number. When the neon is irradiated by sodium, no hydrogenic lines have been seen.

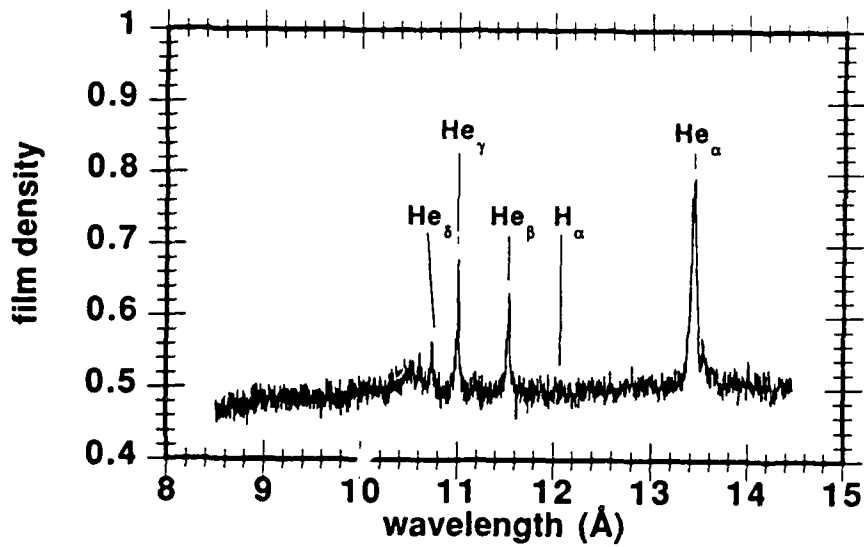


Fig. 3. Time integrated neon K shell spectrum on Saturn showing the pumped  $\gamma$  line to be more intense than adjacent lines.

#### 4. ACKNOWLEDGEMENTS

Work supported by SDIO/T/IS and the U. S. Department of Energy under contract No. DE-AC04-76DP00789. Valuable insights on heliumlike atomic physics were obtained in conversations with M. Blaha and M. Buie at NRL.

## 5. REFERENCES

1. Apruzese, J. P., Davis, J. and Whitney, K. G. 1982 J. Appl. Phys. 53 4020.
2. Apruzese, J. P., and Davis, J., 1985 Phys. Rev. A 31 2976.
3. Apruzese, J. P. et al 1987 Phys. Rev. A 35 4896.
4. Deeney, C., Prasad, R. R., Nash T, and Knobel, N. 1990 Rev. Sci. Instrum. 61 1551.
5. Duston, D., Clark, R. W., Davis, J. and Apruzese, J. P. 1983 Phys. Rev. A 27 1441.
6. Hagelstein, P. L. 1981 University of California Report No. UCRL-53100
7. Hagelstein, P. L. 1983 Plasma Phys. 25 1345.
8. Matthews, D. L. et al 1983 IEEE J. Quantum Electron. QE-19 1786.
9. Porter, J. L. et al 1990 Paper 3D1-2, IEEE Int. Conf. Plasma Sci, Oakland, California USA.
10. Spielman, R. B. et al 1989 Proc. 2nd Int. Conf. on Dense Z Pinches, eds. N. R. Pereira, J. Davis, and N. Rostoker (New York, American Institute of Physics) pp 3-16.
11. Stephanakis, S. J. et al 1988 IEEE Trans. Plasma Sci. 16 472.
12. Vinogradov, A. V., Sobelman I. I., and Yukov E. A. 1975 Sov. J. Quantum Electron 5 59.
13. Young, F. C. et al 1987 Appl. Phys. Lett. 50 1053.
14. Young, F. C. et al 1990 submitted to J. Appl. Phys.

NRL EXPERIMENTAL PULSED POWER X-RAY LASER PROGRAM

F. C. Young, B.L. Welch,+ D.D. Hinshelwood,\* and R.J. Comisso

Pulsed Power Physics Branch  
Plasma Physics Division  
Naval Research Laboratory  
Washington, DC 20375-5000

+ University of Maryland, College Park, MD.

\* JAYCOR, Vienna, VA.

## I. Introduction

Research on the development of a pulse-power driven Na/Ne photopumped soft x-ray laser continued in FY90. This lasing scheme uses line-coincidence photopumping of heliumlike Ne ions by x-rays from heliumlike Na ions produced in a nearby Z-pinch implosion. The FY90 program involved three different aspects of this scheme: 1) the development of a higher power Na pump source in a collaborative effort with Physics International (PI) personnel, (2) participation in Na source development and Na/Ne photopumping experiments on the 10-MA Saturn generator at Sandia National Laboratory (SNL), and (3) experiments to characterize the properties of Ne Z-pinch plasmas as used in photopumping experiments and as a medium for lasing. Activities in these three areas are summarized below.

In FY89, experiments on the photopumping of neutral Ne atoms with K-shell radiation from a nearby Ne implosion leading to population inversion and lasing through Auger decay were initiated as described in the FY 1989 Final Report. Despite favorable experimental results and modeling, this work was not continued in FY90 because sufficient funding to support both approaches to a laboratory soft x-ray laser was not available.

## II. Sodium Source development

A Na pump for the Na/Ne photopumped x-ray laser was developed in FY90 using the Double-EAGLE generator at Physics International. The NaF capillary source, originally used on Gamble II at the Naval Research Laboratory, was modified to provide a plasma appropriate for implosions driven by the 3-MA current of the Double-EAGLE generator. Sodium pump powers up to 115 GW,  $\sim 5\times$  that obtained on Gamble II, were produced reliably on Double-EAGLE. Calculations indicate that a gain of  $2\text{ cm}^{-1}$  can be realized on the 230-Å line in a neon plasma located 2 cm from this source. This NRL/PI collaboration has been documented in a manuscript which has been submitted for publication in the Journal of Applied Physics. A copy of this manuscript is included as Appendix A.

In February, 1990 personnel at Sandia National Laboratory carried out Na-wire-array implosions on the 10-MA SATURN generator to produce a high-power sodium pump source. Frank Young assisted in these experiments. His experience with similar experiments on the Double-EAGLE generator was valuable in carrying out Na-wire extrusions to produce a Na-wire array. The maximum Na pump power produced in this experiment was 160 GW, and the results were presented at the IEEE International Conference on Plasma Science in May 1990 by SNL personnel.

### III. Sodium-Neon Photopumping

In September 1990, experiments were carried out on the SATURN generator to measure the photopumping of Ne using the x-ray emission from a Na-wire-array implosion. The Ne was confined in a gas bag located 2 cm from the Na implosion. The intense x-ray emission from an implosion on SATURN was sufficient to both heat the Ne to the heliumlike stage and to provide about 150 GW of Na pump power. Frank Young participated in these experiments. He assisted in evaluating Na wire arrays, in fielding x-ray diagnostics, and in giving guidance to shot-to-shot measurements. The evidence for photopumping of Ne by Na is impressive in these experiments, and the results were presented by SNL personnel at the 13th International Conference on Lasers and Applications (LASERS'90) in San Diego on December 9-14, 1990.

### IV. Neon Plasmas from Z-Pinch Implosions

The preparation of Ne plasmas as potential lasants for the Na/Ne photopumping scheme has been investigated. The goal of this work is to optimize the Ne IX ground-state population for photopumping experiments. Neon Z-pinch implosions with modest driving currents (100-200 kA) were used to produce soft implosions in order to create plasmas with temperatures of 50-100 eV and ion densities of about  $10^{18}$  cm<sup>-3</sup>, conditions appropriate for lasing. Spectroscopic measurements of Ne VIII emissions were used to evaluate the conditions of the imploded plasma under different experimental configurations. Measurements with temporal, spatial, and spectral resolution were required to determine the temperature, density, and Ne IX population fraction. Absolute spectral-intensity measurements were made to determine excited-state populations of Ne VIII. The Ne IX ground-state population was inferred from these measurements using an atomic-physics equilibrium model. A preliminary report of some of these results is included as Appendix B.

The Ne implosion experiments were carried out on a test stand where the implosions were studied under conditions similar to the Ne return-current geometry used in previous Na/Ne fluorescence experiments Gamble II. The results of these experiments can be used to compare the photopumping observed in experiments on Gamble II with the the predictions of atomic-physics modeling. The Na pump power, measured in the experiments on Gamble II, and the Ne plasma conditions, inferred from the test-stand experiments, are now available so that a quantitative measure of the absorption of the Na pump line by the Ne plasma can be made. Support to carry out and document this analysis in FY91 has been requested.

The experience that has been developed at NRL in producing plasmas with significant Ne IX ground-state populations has been made available to researchers at PI and SNL. The higher power generators at these laboratories may be used to produce sufficient power to achieve lasing with the Na/Ne photopumping scheme.

APPENDIX A

Implosions of NaF plasmas with a 3-MA driver  
for photopumping a Na-Ne x-ray laser

F.C. Young, D.D. Hinshelwood\* and J.P. Apruzese

Plasma Physics Division  
Naval Research Laboratory  
Washington, DC 20375-5000

C. Deeney, T. Nash and R.R. Prasad

Physics International Co.  
San Leandro, CA 94577

Abstract - Intense heliumlike sodium 11-Å line radiation is required to resonantly photopump a neon plasma in the Na-Ne soft x-ray laser scheme. The implosion of a NaF capillary-discharge plasma with a 3-MA peak current is used to produce a power exceeding 100 GW in this He- $\alpha$  line. The power is optimized by varying both the initial radius of the 3-cm long NaF plasma column and the time delay between the capillary current and the generator current. Maximum power of 115 GW is obtained for implosions which occur just after peak current. Burn-through of the heliumlike sodium stage is evident in spectroscopic measurements where sodium Ly- $\alpha$  line emission is 2 to 4 times stronger than He- $\alpha$  emission. Mass loadings of 200 to 400  $\mu\text{g}/\text{cm}$  are inferred from measured implosion times and initial plasma diameters. CRE model calculations are used to relate the He- $\alpha$  line power and the Ly- $\alpha$ /He- $\alpha$  line ratio to the plasma electron temperature and ion density. Measurements indicate that temperatures of 350 to 560 eV and ion densities approaching  $10^{20} \text{ cm}^{-3}$  are produced in these implosions. The mass load inferred from implosion dynamics is consistent with the ion density deduced from spectral measurements.

## I. INTRODUCTION

Intense line radiation from a sodium plasma is required to resonantly photopump a neon plasma in the Na-Ne soft x-ray laser scheme. The pump radiation is the Na X  $1s^2(^1S_0) - 1s2p(^1P_1)$  transition at 11 Å (He- $\alpha$ ) which is used to resonantly photoexcite the  $1s4p(^1P_1)$  level of Ne IX.<sup>1</sup> This excitation, according to calculations,<sup>2</sup> can produce population inversions for the 3-4, 2-4, and 2-3 lines in a neon plasma with an electron temperature of about 50 eV and an ion density of  $10^{18}$  to  $10^{19}$  cm<sup>-3</sup>. Powers of 25 to 30 GW have been produced in this pump line by imploding the NaF plasma produced by a capillary-discharge source<sup>3</sup> with a 1-MA pulsed power driver.<sup>4</sup> Resonant photopumping of Ne IX has been demonstrated with this pump power for a Na-Ne separation of 5 cm.<sup>2,5</sup> Modeling of the Na-Ne lasing system indicates that to produce a gain of 1 cm<sup>-1</sup> on the Ne IX  $3d(^1D_2) - 4f(^1F_3)$  line, pump powers of 100 to 250 GW are required for Na-Ne separations of 3 to 5 cm.<sup>6</sup> Smaller separations will reduce the power required to achieve this gain. Alternatively, for a given pump power, smaller separations will lead to larger gain.

In this paper we report measurements of He- $\alpha$  powers exceeding 100 GW in experiments where the radiated power is increased by increasing the current driving the implosion. The Double-EAGLE generator<sup>7</sup> at Physics International was used to produce currents of 3 MA to drive NaF implosions. The NaF discharge source<sup>3</sup> was modified to increase the mass per unit length of the plasma for these implosions. Modifications to this source and the experimental arrangement on Double-EAGLE are described in Sec. II. Experimental results are presented in Sec. III. Section IV contains an analysis of the implosions and an evaluation of the average temperature and density of the imploded plasma deduced from the measurements. Implications for the Na-Ne lasing scheme are discussed in Sec. V.

## II. EXPERIMENTAL CONDITIONS

The NaF discharge source has been described in detail elsewhere.<sup>3</sup> Briefly, a 40 to 50-kA current pulse with a 3.4- $\mu$ s period is driven through a NaF capillary. Plasma ejected from one end of the capillary is collimated to form a 1 to 2-cm diam, several-cm-long cylindrical plasma with a mass per unit length of 15 to 30  $\mu$ g/cm. Implosions with this source on the 1-MA Gamble II generator at the Naval Research Laboratory indicated that this mass could be increased by increasing the current through the capillary. For the Double-EAGLE experiment, the capillary current was increased to about 200 kA by doubling the capacitance (1.8 to 3.6  $\mu$ F) and by doubling the charging voltage (25 to 50 kV) on the capacitor. With these changes, the period of the current increased to 4.5  $\mu$ s, and the mass per unit length increased an order of magnitude as indicated by the implosion experiments to be described.

Plasma from the NaF discharge was injected across a 3-cm anode-cathode gap on the Double-EAGLE generator as shown in Fig. 1. The plasma was emitted from a carbon nozzle (anode) and directed toward a coarse high-voltage copper or aluminum wire mesh (cathode). The initial 3-cm long plasma column was confined radially by nozzles of either 0.5, 0.75, or 1.0-cm exit radius. The carbon nozzle was connected to 12 return-current rods through an array of aluminum strips. The nozzle and aluminum strips were replaced on each shot. The return-current rods were equally spaced on a diameter of 10 cm. Radiation from the on-axis implosion was viewed through gaps in the return-current path. Diagnostics were located at 65° to the axis of the generator so that 0.5 cm of the 3-cm long anode-cathode gap was obscured from view by the capillary nozzle. To implode the plasma, the generator was fired several microseconds after the start of the capillary current. To optimize the sodium He- $\alpha$  line power, both the exit diameter of the nozzle and the delay between the firing the capillary and pulsing the generator were varied.

X-rays from the imploded NaF were measured with an array of diagnostics to provide temporal, spectral, and spatial resolution. Two vacuum x-ray diodes (XRDs) with copper cathodes and appropriate filters were used to record total sodium K-shell and sodium He- $\alpha$  x-ray powers. The sensitivities of these detectors are shown in Fig. 2. The energy dependence of the copper-cathode XRD sensitivity was taken from Ref. 8, and the absolute sensitivity was determined experimentally by comparison with an aluminum-cathode XRD as described in Ref. 9. The cathode and filter materials were selected to optimize the sensitivities for the x-rays of interest. These sensitivities decrease for x-rays with energies below the copper L-edge (0.95 keV) and above the aluminum K-edge (1.56 keV) or the germanium L-edge (1.22 keV). For the germanium-filtered XRD, discrimination against the F VIII and F IX,  $n = 2-1$  lines at 0.72 and 0.83 keV is at least an order of magnitude relative to the sodium He- $\alpha$  line. Sodium K-shell emissions were spatially and spectrally resolved with a 4-cm curved Mica crystal spectrograph and were time resolved with a 4-cm curved Mica crystal spectrometer with gated microchannelplates (10-ns resolution).<sup>10</sup> A time-resolved x-ray pinhole camera with two pinholes was used to image both sodium K-shell and sub-keV x-ray emissions with 0.2-mm spatial resolution onto gated microchannelplates (5-ns resolution).<sup>11</sup> The pinholes were filtered with 2- $\mu$ m aluminized Kimfol<sup>12</sup> for subkeV x-rays, and with 8- $\mu$ m Kimfol<sup>12</sup> plus 1.8- $\mu$ m aluminum to transmit only keV x-rays.

### III. EXPERIMENTAL RESULTS

The current driving an implosion and XRD measurements of the imploded plasma are presented in Fig. 3. The implosion occurs with the emission of a burst of sodium K-shell x-rays after the current peaks at 3.2 MA. This shot was taken with a 0.75-cm radius nozzle and a capillary-to-generator delay of 5.5  $\mu$ s. The 130-GW peak sodium He- $\alpha$  XRD power is one of the largest measured and

corresponds to a time-integrated yield in this line of 3.4 kJ. The total K-shell XRD power is 540 GW and the yield is 14 kJ. The time interval from the start of the current (determined by extrapolating the slope of the current rise to the base line) to peak x-ray emission is used to measure the implosion time. For this shot the implosion time is 119 ns.

Time-integrated x-ray spectra were recorded to measure sodium K-shell x-ray line emissions. A typical spectrum obtained for a shot with a 0.5-cm radius nozzle and 5.0- $\mu$ s capillary delay is shown in Fig. 4. The Na X  $1s^2-1s2p$  (He- $\alpha$ ),  $1s^2-1s3p$  (He- $\beta$ ), and  $1s^2-1s4p$  (He- $\gamma$ ) lines are identified along with the Na XI  $1s-2p$  (Ly- $\alpha$ ) line. The spectra are dominated by the Ly- $\alpha$  and He- $\alpha$  lines. The spectra were recorded on Kodak DEF film, scanned with a narrow-slit densitometer, and converted to intensity using published film calibrations.<sup>13</sup> Corrections were made for x-ray attenuation by a 2- $\mu$ m Kimfol<sup>12</sup> plus 1.8- $\mu$ m aluminum filter on the spectrograph, but no corrections were made for crystal efficiency. Since the mica crystal reflectivity<sup>14</sup> is nearly constant with x-ray energy for the lines of interest in Fig. 4, the relative intensity of each line was determined by integrating over the line profile and subtracting the spectral background. From shot-to-shot, the Ly- $\alpha$ /He- $\alpha$  ratio ranges from 2.2 to 3.9, and this ratio is not correlated with either the capillary nozzle radius or the capillary delay. For the shot in Fig. 4, this ratio is 3.8 and the integrated He- $\alpha$  XRD yield is 5.0 kJ. If this XRD yield is from the sodium He- $\alpha$  line, then the total yield in the Ly- $\alpha$  and He- $\alpha$  lines is 24 kJ, which is consistent with the yield of 30 kJ measured by the K-shell XRD on this shot. A somewhat higher energy should be measured by the K-shell XRD because it includes Na X and Na XI higher-series line emissions and continuum, as well as the He- $\alpha$  and Ly- $\alpha$  lines (see Fig. 2).

The sodium He- $\alpha$  XRD power is presented as a function of the capillary-to-generator delay in Fig. 5a and as a function of implosion time in Fig. 5b. The

results in Fig. 5a indicate that a power of 130 GW can be produced for a 0.5 or 0.75-cm radius nozzle and a delay of 5.0 to 5.5  $\mu$ s. For the 0.5-cm radius nozzle, the power may be even larger for delays less than 5  $\mu$ s. As the delay is increased, the implosion tends to occur later in time for a given nozzle, as indicated in Fig. 5b. This behavior is consistent with allowing time for more plasma from the capillary to fill the diode gap. Maximum power is measured for an implosion time of about 120 ns. The power may be even larger for implosion times of 105 to 115 ns, but no measurements were made in this range. However, experience with Z-pinch implosions indicates that maximum coupling of energy to the load and consequent x-ray emission occurs for an implosion time slightly after peak current,<sup>15</sup> as observed in Fig. 3. The capillary-to-generator delay on Double-EAGLE could be preset to a precision of  $\pm 0.1$   $\mu$ s so that the implosion time for maximum He- $\alpha$  x-ray power could be reliably reproduced.

The germanium-filtered XRD records the heliumlike  $1s^2-1s2p$   $^1P$  resonance line as well as the heliumlike  $^3P$  intercombination line on the low energy side of the resonance line. These lines are resolved in the crystal spectrograph measurements, (see Fig. 4), and their relative intensity was used to unfold the resonance line power. The intercombination-to-resonance line ratio ranges from 0.10 to 0.16 for all the shots in this experiment. For the high He- $\alpha$  power shots, this ratio is 0.14 and corresponds to a resonance line power that is 89% of the power in both lines. This fraction is larger than observed in similar measurements on Gamble II where He- $\alpha$  satellite transitions as well as the intercombination line were observed.<sup>16</sup> In the present experiment, satellite lines were either not observed or were much less intense than the intercombination line, and their contribution to this unfold was neglected. With this correction, the  $1s^2-1s2p$   $^1P$  resonance line power is 115 GW for the high He- $\alpha$  power shots.

Dynamics of the imploding plasma were observed in time-resolved pinhole camera images of the x-ray emission. Typical images of the emitting plasma are presented in Fig. 6 for shots with a 0.75-cm radius nozzle. Figure 6a shows subkeV images for a shot with 4.2- $\mu$ s capillary delay, while Fig. 6b shows keV images for a shot with 6.5- $\mu$ s capillary delay. The timing of the frames relative to the sodium K-shell power is indicated for each shot. The plasma was injected from the bottom in these images. The length of these images represents 2.5 cm of the 3-cm long pinch due to the viewing angle of the diagnostic. SubkeV x-ray emission is observed before keV x-ray emission. Early in time, the subkeV images fill the width of the microchannelplate strips. Current-return connections block the view of the plasma at the bottom corners of these images. Shadows at the top of the subkeV images arise from the wire mesh cathode. In frame 8 of Fig. 6b, the keV x-ray emission is observed from a tight pinch, about 3 mm in diameter, along the entire length of plasma; in later frames the plasma begins to disrupt. Similar diameter images of keV x-rays were observed for both the 0.5-cm and 0.75-cm radius nozzles. For the 1.0-cm radius nozzle, the pinch was about 4 mm in diameter at bulk maximum compression. The radial contraction of the collapsing plasma indicated in these images was used to estimate radial velocities of 20 to 40 cm/ $\mu$ s for these implosions.

The structure of the  $m = 0$  sausage instability is well defined in the keV pinhole camera images at late time. By following the evolution of individual  $m = 0$  instabilities at different axial locations, growth rates were estimated and compared with calculations. The  $m = 0$  structure in Fig. 6b corresponds to  $kr = 3.5$  where  $k$  is the wave number of the structure and  $r$  is the pinch radius. Growth rates of  $0.2$  to  $1.7 \times 10^8 \text{ s}^{-1}$  were estimated from the evolution of the neck and flare structures in frames 8, 9 and 10 of Fig. 6b. For example, initially (frames 8 and 9) the measured growth rates are  $1.7 \times 10^8 \text{ s}^{-1}$  for the

neck and  $0.2 \times 10^8 \text{ s}^{-1}$  for the flare. However, 5-ns later (frames 9 and 10) the growth rates are  $0.8 \times 10^8 \text{ s}^{-1}$  for the neck and  $0.3 \times 10^8 \text{ s}^{-1}$  for the flare. Pereira<sup>17</sup> has calculated the growth rates of  $m = 0$  instabilities for thin surface currents and for sheath currents of finite width. For  $m = 0$  instabilities with  $kr = 3.5$ , the calculated growth rates are  $0.3$  to  $0.5 \times 10^8 \text{ s}^{-1}$  for a 560-eV plasma provided the current flows in a sheath of width 50% less than the pinch radius. This temperature is based on an analysis of spectral measurements given in Sec. IV. Smaller growth rates are calculated for lower temperatures. If the radial current distribution is uniform, the growth rate is an order of magnitude smaller. The measured and calculated growth rates are consistent only if the current is assumed to flow in a sheath rather than in a uniform radial distribution.

Time-resolved measurements of the sodium He- $\alpha$  and Ly- $\alpha$  lines are presented in Fig. 7. Early in time (frame 2,3), both lines are observed with comparable intensities. Later in time, the He- $\alpha$  line decreases while the Ly- $\alpha$  line increases. By the last frame (8,9), the Ly- $\alpha$  line is decreasing, but the He- $\alpha$  line does not reappear. The large continuum in frame 6,7 is due to background exposure of the microchannelplate at peak x-ray emission. These measurements indicate that during the radiation pulse the imploded sodium is heated and ionized beyond the He-like stage. This burn-through of the He- $\alpha$  line was observed in all these NaF implosions on Double-EAGLE. Comparing the implosion dynamics, including the pinch and unstable phases, with the time resolved K-shell spectra indicates that some plasma heating occurs during the unstable phase of the pinch.

#### IV. INTERPRETATION

The mass per unit length ( $\mu$ ) of the imploded plasma can be determined from measurements of the current waveform and the implosion time ( $\tau$ ) if the initial radius ( $r_0$ ) is known. For an imploding cylindrical shell with an approximately linear current rise, the scaling

$$\tau = Kr_0 \mu^{1/2} / I_m \quad (1)$$

can be used, where  $I_m$  is the peak current and  $K$  is a constant dependent on the current waveform.<sup>18</sup> For nickel-wire arrays,  $K = 38$  has been determined from z-pinch implosions on Double-EAGLE.<sup>19</sup> For a uniformly filled cylinder, a similar scaling is assumed but with a different value of  $K$ . Numerical calculations for specific current waveforms are used to determine  $K$ . For the Double-EAGLE waveform,  $K = 23$  for  $\tau$  in ns,  $r_0$  in cm,  $I_m$  in MA, and  $\mu$  in  $\mu\text{g}/\text{cm}$ .<sup>20</sup> An analysis of a uniformly filled cylindrical sodium implosion based on the Gamble II current waveform gives  $K = 26$ . (Ref. 21) The similarity of these  $K$ -values for 1.2-MA and 3.4-MA drivers supports the scaling in Eq. 1.

In the present experiment, the exit diameter of the capillary nozzle places a lower limit on the initial plasma radius. However, plasma is observed to diverge from the exit of the nozzle in visible-light framing images of the capillary-discharge plasma similar to those described in Ref. 3. Estimated plasma diameters based on these images are given in Table I. Each plasma diameter is larger than the corresponding nozzle diameter due to this divergence, particularly for the smaller nozzles. The diameters in Table I were measured for the plasma located 1 cm from the exit of the nozzle at 5 to 6  $\mu\text{s}$  after the start of the capillary current; conditions corresponding to the initial plasma for the implosions on Double-EAGLE which produced maximum sodium He- $\alpha$  power. These diameters were used to evaluate  $\mu$  according to Eq. 1.

Values of  $\mu$  for each nozzle with implosion times of approximately 120 ns are given in Table I. The uncertainty in each  $\mu$ -value is  $\pm 25\%$  with the primary contribution of  $\pm 10\%$  from the radius measurement. A larger mass per unit length and higher He- $\alpha$  power are produced for the two smaller-radius nozzles. For shots with larger capillary delay and longer implosion time, the values of  $\mu$  increase to more than 400  $\mu\text{g}/\text{cm}$ , at least for the 0.5- and 0.75-cm radius nozzles. No increase is observed for the 1.0-cm radius nozzle. Maximum sodium He- $\alpha$  power is produced for an initial plasma diameter of 1.7 to 1.8 cm and an inferred mass per unit length of about 300  $\mu\text{g}/\text{cm}$ .

The mass per unit length of NaF capillary-discharge plasmas was determined in previous implosion experiments on the Gamble II generator. A value of about 30  $\mu\text{g}/\text{cm}$  was deduced from implosion dynamics,<sup>4</sup> and values of 14 to 33  $\mu\text{g}/\text{cm}$  were inferred from analyses of x-ray measurements of several imploded plasma.<sup>22</sup> For these measurements, a 50-kA peak current pulse was driven through the capillary. By increasing this current to about 200 kA in the Double-EAGLE experiment, the mass per unit length increased an order of magnitude.

The principal objective of this experiment is to maximize the sodium He- $\alpha$  line power. We focus on this quantity as both a figure of merit and as a diagnostic of the average properties of the NaF plasma. To calculate the He- $\alpha$  power as a function of temperature, density, and pinch diameter, the plasma is assumed to be cylindrical and homogeneous. A collisional-radiative-equilibrium (CRE) atomic model for sodium is employed as described in Ref. 22. The diameter of the plasma is determined from the time resolved x-ray pinhole camera images. For a given diameter, the He- $\alpha$  power per unit length and the Ly- $\alpha$ /He- $\alpha$  ratio are displayed most instructively as contours versus ion density and temperature. Such contours are displayed in Fig. 8 for a 3-mm diameter plasma corresponding to the imploded plasma size observed in this experiment.

It is apparent from Fig. 8a that the He- $\alpha$  power is primarily a function of density. This is a result of burn-through of the heliumlike stage which counteracts any tendency of the He- $\alpha$  power to increase with temperature due to increasing collisional excitation. Therefore, increasing the mass loading of the plasma at moderate temperature (250-500 eV) is the most promising approach to maximize the He- $\alpha$  power.

In contrast to Fig. 8a, Fig. 8b indicates that the Ly- $\alpha$ /He- $\alpha$  ratio depends primarily on temperature. This is expected because the ratio of the hydrogenlike-to-heliumlike ion populations increases monotonically with temperature. The nearly pure density dependence of the He- $\alpha$  power and the nearly pure temperature dependence of the Ly- $\alpha$ /He- $\alpha$  ratio allow the state of the plasma (approximated as a homogeneous cylinder) to be determined by measuring both of these quantities on the same shot.

Measurements of the He- $\alpha$  power and the Ly- $\alpha$ /He- $\alpha$  ratio are used to determine average ion density and electron temperature using the CRE model. Measured values of the maximum He- $\alpha$  power per unit length and the Ly- $\alpha$ /He- $\alpha$  ratio are plotted in Fig. 8 for the 0.5-cm and 0.75-cm radius nozzles. By fitting both measurements, the density and temperature of the plasma are determined for each shot. Uncertainties in these measured quantities of  $\pm 10\%$  are indicated in this figure. The uncertainty indicated for the He- $\alpha$  power is for constant Ly- $\alpha$ /He- $\alpha$  ratio, and the uncertainty indicated for the Ly- $\alpha$ /He- $\alpha$  ratio is for constant He- $\alpha$  power. The electron temperature is  $560 \pm 60$  eV for the 0.5-cm radius nozzle and  $350 \pm 30$  eV for the 0.75-cm radius nozzle. For both nozzles, the ion density is  $(0.8 \pm 0.2) \times 10^{20} \text{ cm}^{-3}$ . This ion density corresponds to the initial mass per unit length of 300  $\mu\text{g}/\text{cm}$ , determined from implosion dynamics, compressed to a diameter of 3.7 mm, consistent with diameters observed in the time-resolved pinhole camera images.

Shot-to-shot comparisons of the sodium K-shell line spectra were made to look for systematic changes in the spectra with variations of the capillary delay and the nozzle radius. The spectra are very similar; for example, only modest variations of the Ly- $\alpha$ /He- $\alpha$  line ratio and of the He- $\alpha$  intercombination-to-resonance line ratio have already been noted, and these variations are not systematic. The only systematic variation observed is for satellite lines on the low energy side of the sodium Ly- $\alpha$  line. The satellite lines are more intense for smaller radius nozzles and for longer capillary delay. Satellite lines are compared in Fig. 9 for two shots with different radius nozzles but the same capillary delay. The satellites are much more intense for the 0.5-cm radius nozzle. Variation of the satellite intensity with capillary delay is illustrated by comparing the spectrum in Fig. 9a with the spectrum in Fig. 4 (5.5- $\mu$ s delay). The satellites are more intense for the larger delay, and this intensity difference is even more apparent for larger differences in delay. The ratio of heliumlike-satellite to hydrogenic-resonance-line emission is strongly dependent on electron temperature as pointed out by Lunney.<sup>23</sup> The satellites arise from doubly excited heliumlike ions which require electrons with energies well above the heliumlike ionization limit (2.5 keV) for this excitation. The absence of any correlation between the Ly- $\alpha$ /He- $\alpha$  line ratio, which is temperature sensitive, and the satellite intensity suggests that the systematic variation in the magnitude of the satellite lines is not due to temperature effects. A possible explanation is that a beam of high energy electrons is produced across the diode in the imploding plasma under the conditions of longer capillary delay and/or smaller radius nozzle. The production of electron beams may be coupled to the pinch dynamics or to the evolution of the  $m = 0$  instabilities. Further understanding of how these satellites are produced will require more study.

## V. CONCLUSIONS

NaF plasmas from a capillary discharge were successfully imploded with a 3-MA driving current. Maximum sodium K-shell emission was achieved for a mass load of about 300  $\mu\text{g}/\text{cm}$  and an initial plasma radius of about 0.9 cm. This mass load was produced by driving the capillary with a 200-kA current pulse and waiting several microseconds for plasma to be ejected from the source. Increasing the capillary current from 50 to 200 kA increased the mass load by an order of magnitude. Systematic control of the mass load from 200 to 400  $\mu\text{g}/\text{cm}$  was achieved by adjusting the delay between the capillary current and the 3-MA driving current.

Maximum power of 115 GW in the 11- $\text{\AA}$  heliumlike-sodium line emission was obtained by adjusting the mass per unit length and the initial radius of the plasma. The plasma was compressed to a diameter of 3 to 4 mm and to a total ion density approaching  $10^{20} \text{ cm}^{-3}$ . The compressed plasma was heated to a temperature of 350 to 560 eV (time-averaged), and the sodium was stripped beyond the heliumlike stage. Atomic CRE calculations indicate that the most promising approaches to achieving larger power are to compress the plasma to higher density or increase the total plasma mass at moderate temperature (250-500 eV).

The power in the 11- $\text{\AA}$  sodium line may be increased in two ways. Implosions driven by a 10-MA current source<sup>24</sup> may compress more plasma to even higher density and produce more pump-line power. In addition, the power may be doubled by replacing the NaF plasma with a pure sodium plasma. An array of extruded sodium wires has been developed,<sup>25</sup> and the implosion of such arrays on Double-EAGLE has produced 150 GW in the pump line.<sup>26</sup> Alternatively, the NaF capillary could be replaced by a sodium confined-discharge source.<sup>27</sup>

The sodium pump power produced in this experiment is sufficient to produce unity gain at 230 Å in an appropriate neon plasma located 3 cm from the pump.<sup>6</sup> Because the sodium plasma is the pump source in the Na-Ne laser scheme, instabilities and non-uniformities in the sodium implosion are not critical to lasing. The desired properties of the neon lasant plasma have been given elsewhere,<sup>2</sup> and the goal is to locate the neon as close as possible to the sodium in order to optimize pumping efficiency, yet maintain the appropriate neon lasant conditions. In the present experiment, maximum pump power is produced for an initial NaF plasma radius less than 1 cm, so that the neon could be located as close as 2 cm to the sodium. If the diameter of the return-current posts is reduced to 3 cm, then the neon plasma could be located at 2 cm just outside the return-current path. For a 2-cm separation and 100-GW sodium pump power, a gain of  $2 \text{ cm}^{-1}$  in the 230-Å line is expected. Research is in progress to provide the required neon lasant for such a pump source.<sup>28</sup>

#### Acknowledgements

The support of M. Krishnan in providing initial guidance to this experimental effort is appreciated. Excellent technical assistance was provided by B. Kribs, N. Knobel, and the Double-EAGLE operations staff at PI. The assistance of V. Scherrer (Sachs Freeman) and D. Rose (Jaycor) at NRL and L. Warren at PI in reducing x-ray film records to intensity is appreciated. This work was supported by SDIO/T/IS and directed by NRL. Additional support was provided by the Defense Nuclear Agency.

Table I

Properties of Capillary Discharge Plasmas for Different Radius nozzles

Nozzle Radius (cm)	Initial Plasma Diam (cm)	Mass/length $\mu$ ( $\mu\text{g}/\text{cm}$ )
1.0	2.3	150
0.75	1.8	350
0.5	1.7	300

## References

- \* JAYCOR, Vienna, VA 22180.
- 1. J.P. Apruzese, J. Davis, and K.G. Whitney, *J. Appl. Phys.* 53, 4020 (1982);  
and J.P. Apruzese, and J. Davis, *Phys. Rev. A* 31, 2976 (1985).
- 2. S.J. Stephanakis, J.P. Apruzese, P.G. Burkhalter, G. Cooperstein, J. Davis,  
D.D. Hinshelwood, G. Mehlman, D. Mosher, P.F. Ottinger, V.E. Scherrer, J.W.  
Thornhill, B.L. Welch, and F.C. Young, *IEEE Trans. Plasma Sci.* 16, 472  
(1988).
- 3. B.L. Welch, F.C. Young, R.J. Comisso, D.D. Hinshelwood, D. Mosher, and  
B.V. Weber, *J. Appl. Phys.* 65, 2664 (1989).
- 4. F.C. Young, S.J. Stephanakis, V.E. Scherrer, B.L. Welch, G. Mehlman, P.G.  
Burkhalter, and J.P. Apruzese, *Appl. Phys. Lett.* 50, 1053 (1987).
- 5. F.C. Young, V.E. Scherrer, S.J. Stephanakis, D.D. Hinshelwood, P.J.  
Goodrich, G. Mehlman, D.A. Newman, and B.L. Welch, *Proc. Inter. Conf. on  
LASERS'88*, R.C. Sze and F.J. Duarte, Eds. (STS Press, McLean, VA) 1989, p.  
98.
- 6. J.P. Apruzese and J. Davis, *Proc. Inter. Conf. on LASERS'89*, D.G. Harris  
and T.M. Shay, Eds. (STS Press, McLean, VA) 1990, p. 7.
- 7. P. Sincerny, D. Strachan, G. Frazier, C. Gilman, H. Halava, S. Wong, J.  
Bannister, T. DaSalva, S.K. Lam, P.D. LePell, J. Levine, R. Rodenberg, and  
T. Sheridan, *Proc. Fifth IEEE Conference on Pulsed Power*. 151 (1985).
- 8. R.H. Day, P. Lee, E.B. Saloman, and D.J. Nagel, *J. Appl. Phys.* 52, 6965  
(1981).
- 9. F.C. Young, S.J. Stephanakis, and V.E. Scherrer, *Rev. Sci. Instrum.* 57,  
2174 (1986).
- 10. T. Nash, C. Deeney, P.D. LePell, and R. Prasad, *Rev. Sci. Instrum.* 61, 2804  
(1990).

11. T. Nash, C. Deeney, P.D. LePell, and R. Prasad, Rev. Sci. Instrum. 61, 2807 (1990).
12. Tradename of Kimberly-Clark Corporation, Schweiter Division, Lee, MA 01238.
13. B.L. Henke, J.Y. Uejio, G.F. Stone, C.H. Dittmore and F.G. Fujiwara, J. Opt. Soc. Am. B 3, 1540 (1986).
14. B.L. Henke and P.A. Jaanimagi, Rev. Sci. Instrum. 56, 1537 (1985).
15. D. Mosher, Coupling of Imploding Plasma Loads to High-Power Generators, NRL Memorandum Rept. No. 3687, Naval Research Laboratory, January, 1978 (unpublished).
16. P.G. Burkhalter, G. Mehlman, J.P. Apruzese, D.A. Newman, V.E. Scherrer, F.C. Young, S.J. Stephanakis and D.D. Hinshelwood, J. Quant. Spectrosc. Radiat. Transfer (to be published).
17. N.R. Pereira, N. Rostoker and J.S. Pearlman, J. Appl. Phys. 55, 704 (1984).
18. N.R. Pereira and J. Davis, J. Appl. Phys. 64 R1 (1988).
19. C. Deeney, T. Nash, P.D. LePell, K. Childers, M. Krishnan, K.G. Whitney and W. Thornhill, J. Quant. Spectrosc. Radiat. Transfer (to be published).
20. J. Apruzese and C. Agritellis (private communication).
21. J. Davis, J.E. Rogerson, and J.P. Apruzese, NRL Memorandum Rept. No. 5776, Naval Research Laboratory, May 8, 1986 (unpublished).
22. J.P. Apruzese, G. Mehlman, J. Davis, J.E. Rogerson, V.E. Scherrer, S.J. Stephanakis, P.F. Ottinger, and F.C. Young, Phys. Rev. A 35, 4896 (1987).
23. J.G. Lunney, Phys. Rev. A 40, 467 (1989).
24. R.B. Spielman, R.J. Dukart, D.L. Hanson, B.A. Hammel, W.W. Hsing, M.K. Matzen, and J.L. Porter, in Proceedings of the 2nd International Conference on Dense Z-Pinches, Laguna Beach, CA, 1989, edited by N.R. Pereira, J. Davis, and N. Rostoker (AIP, New York, 1989) p. 3.
25. C. Deeney, R.R. Prasad, T. Nash, and N. Knobel, Rev. Sci. Instrum. 61, 1551 (1990).

26. C. Deeney, T. Nash, R.R. Prasad, M. Krishnan, F.C. Young, D.D. Hinshelwood and J.P. Apruzese, in Record, 17th IEEE Inter. Conf. Plasma Sci., Oakland, CA, 1990, p. 148; and C. Deeney, R.R. Prasad, T. Nash, L. Warren and J.P. Apruzese (submitted to Appl. Phys. Lett.).
27. D.D. Hinshelwood, P.G. Burkhalter, J.M. Buzzi, H.J. Doucet, G. Mehlman, V.E. Scherrer, S.J. Stephanakis, B.L. Welch, and F.C. Young, Bull. Am. Phys. Soc. 33, 2043 (1988).
28. B.L. Welch, H.R. Griem, and F.C. Young, Bull. Am. Phys. Soc. 34, 1914 (1989).

### Figure Captions

- FIG. 1. Arrangement of the NaF capillary-discharge source in the diode region of the Double-EAGLE generator.
- FIG. 2. XRD sensitivities to measure the total sodium K-shell and the He- $\alpha$  x-ray emissions.
- FIG. 3. Current and XRD traces for shot 2072 on Double-EAGLE.
- FIG. 4. Time-integrated x-ray spectrum measured for shot 2111 on Double-EAGLE. Spectral lines from Na X and Na XI ions are identified.
- FIG. 5. Sodium He- $\alpha$  x-ray powers for 0.5, 0.75 and 1.0-cm radius nozzles (a) as a function of capillary-to-generator delay and (b) as a function of implosion time.
- FIG. 6. Time-resolved (a) subkeV and (b) keV x-ray images of NaF implosions for shots with a 0.75-cm radius nozzle. The timing of the sequential 5-ns duration frames is indicated on traces of the sodium K-shell power.
- FIG. 7. Time-resolved spectra of the sodium Ly- $\alpha$  and He- $\alpha$  lines for shot 2077. The time-frame numbers refer to the frame numbers in Fig. 6a. Two numbers are shown for each spectrum because the spectrometer time frames are sequential 10-ns intervals.
- FIG. 8. (a) Contours of constant He- $\alpha$  line power in GW/cm and (b) contours of constant Ly- $\alpha$ /He- $\alpha$  ratio as functions of electron temperature (T) and total ion density (Na + F) for a 3-mm diam NaF plasma. Experimental values corresponding to maximum sodium He- $\alpha$  power for a 0.5-cm radius nozzle (open circle) and a 0.75-cm radius nozzle (solid circle) are indicated.
- FIG. 9. Time-integrated x-ray spectra for NaF implosions (a) with a 0.5-cm radius nozzle and 7.0- $\mu$ s capillary delay (shot 2079) and (b) with a 1.0-cm radius nozzle and 7.5- $\mu$ s capillary delay (shot 2078). Spectral lines from Na X (He- $\alpha$ ) and Na XI (Ly- $\alpha$ ) are identified.

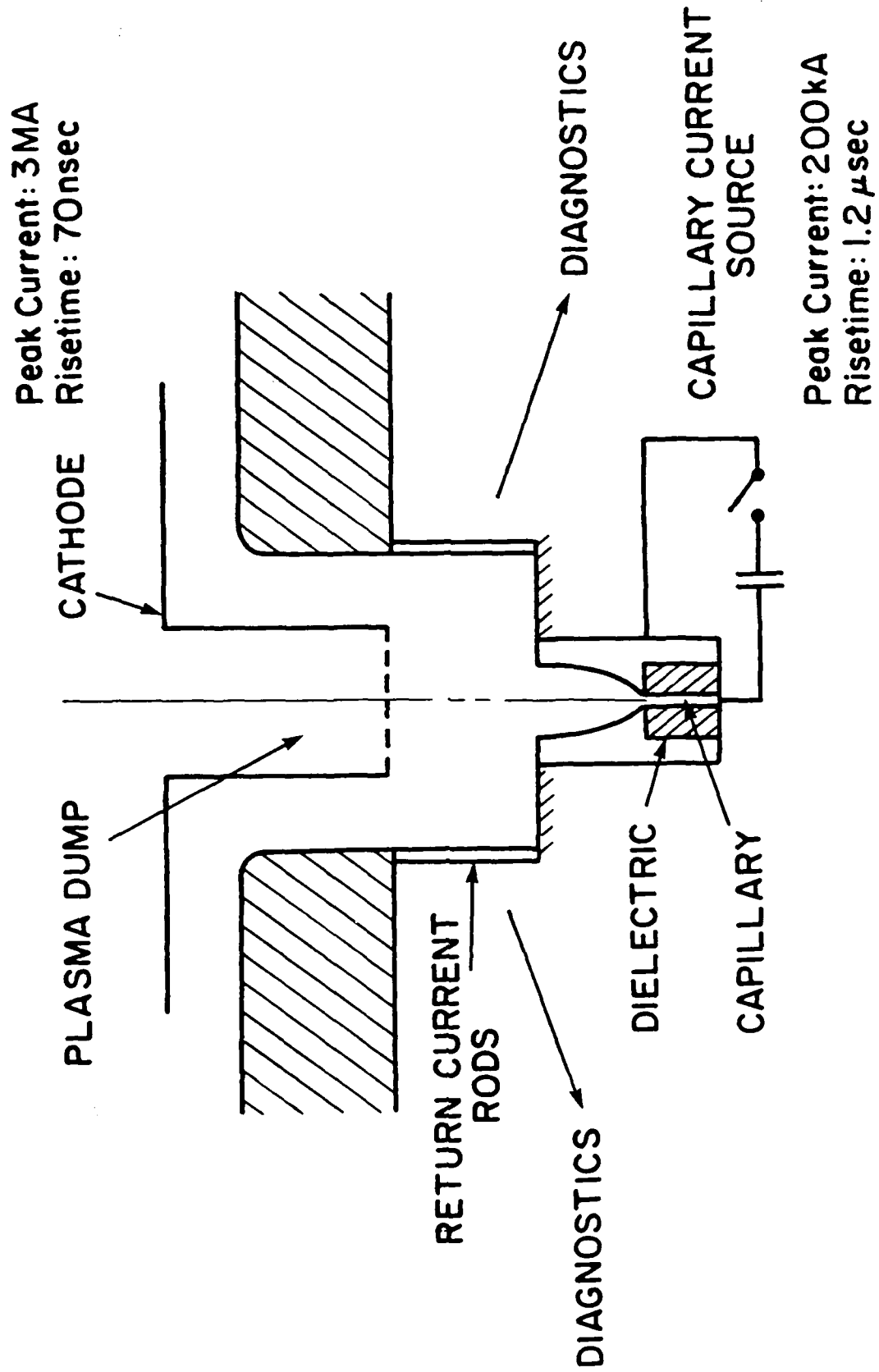


Figure 1

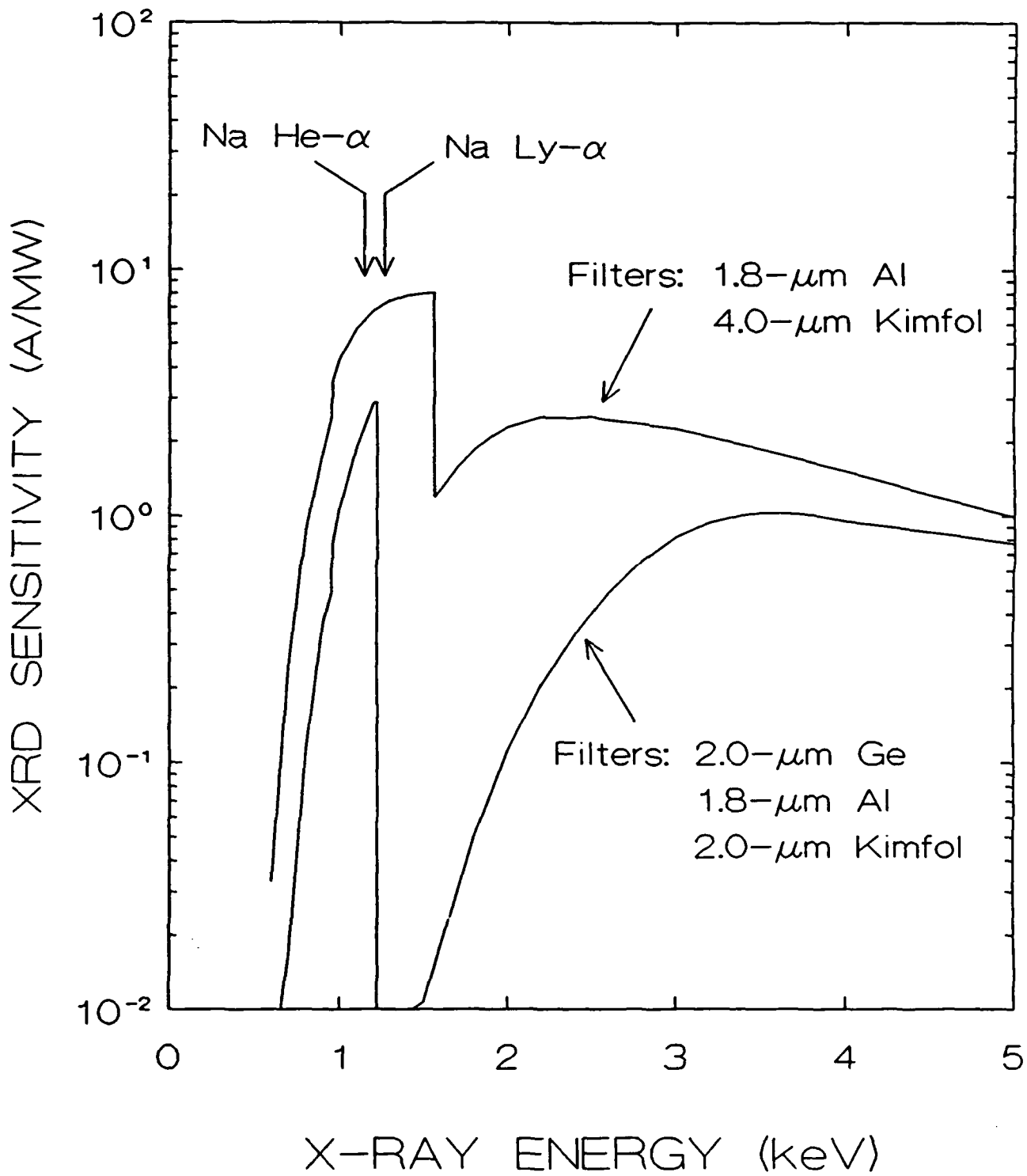


Figure 2

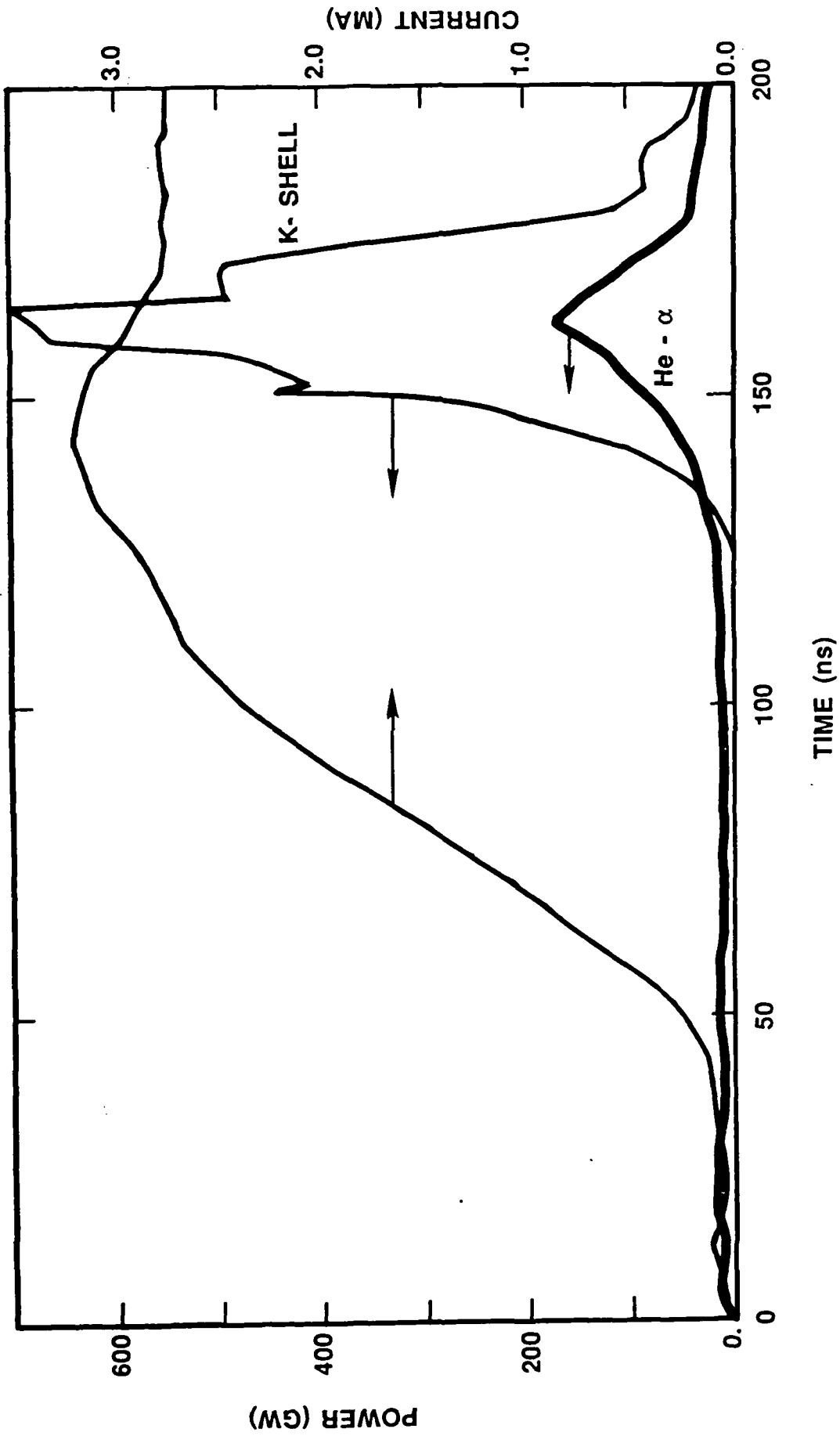


Figure 3

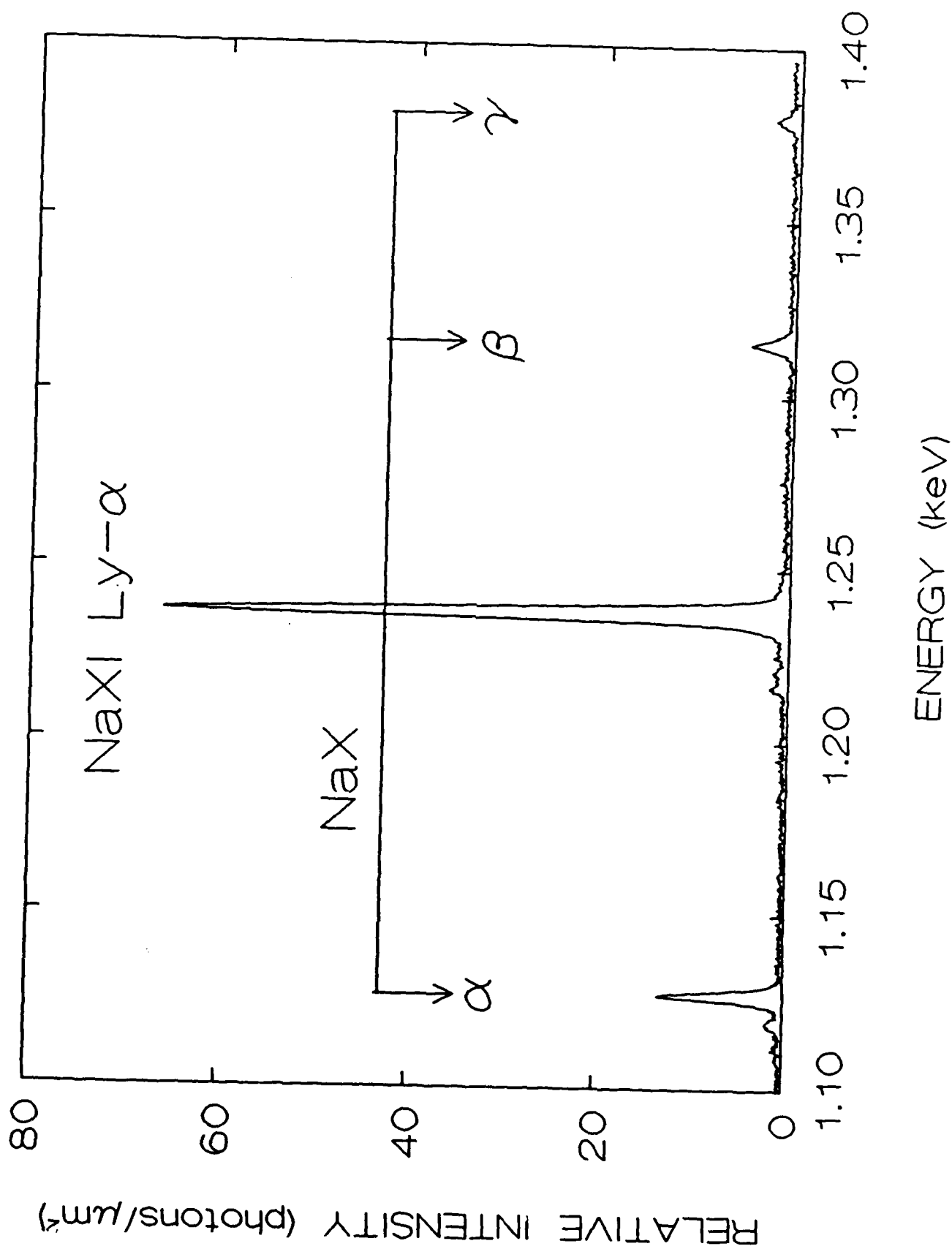


Figure 4

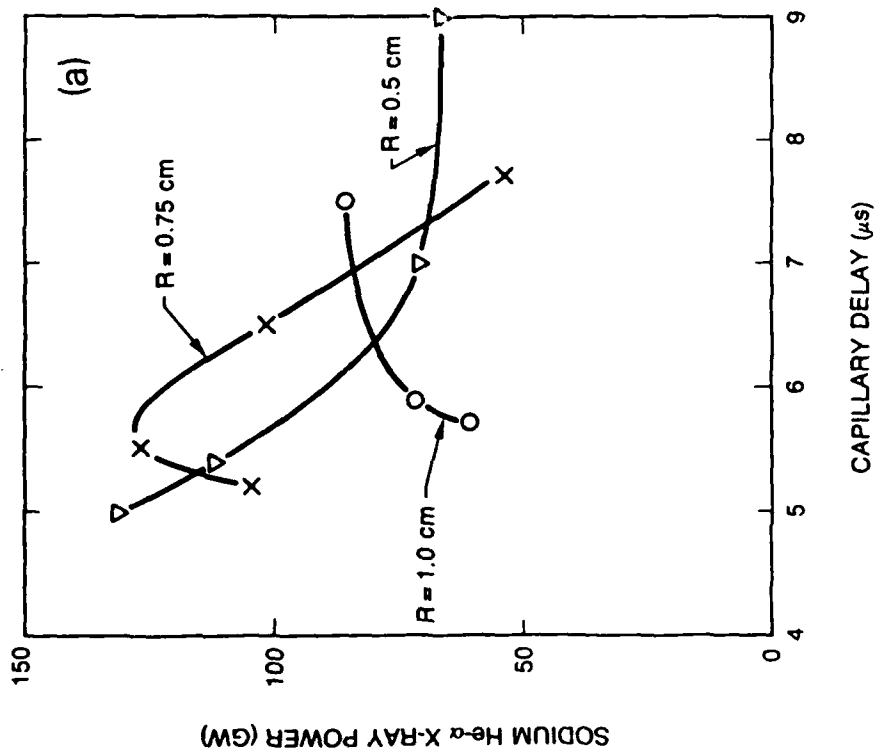
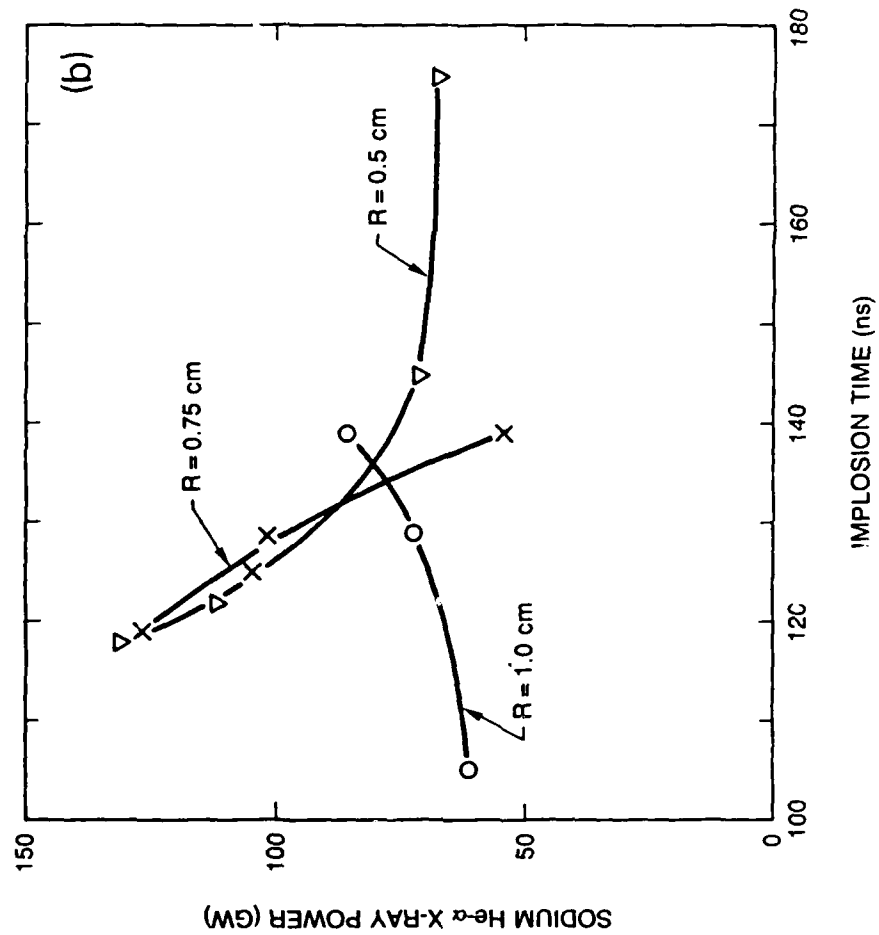


Figure 5

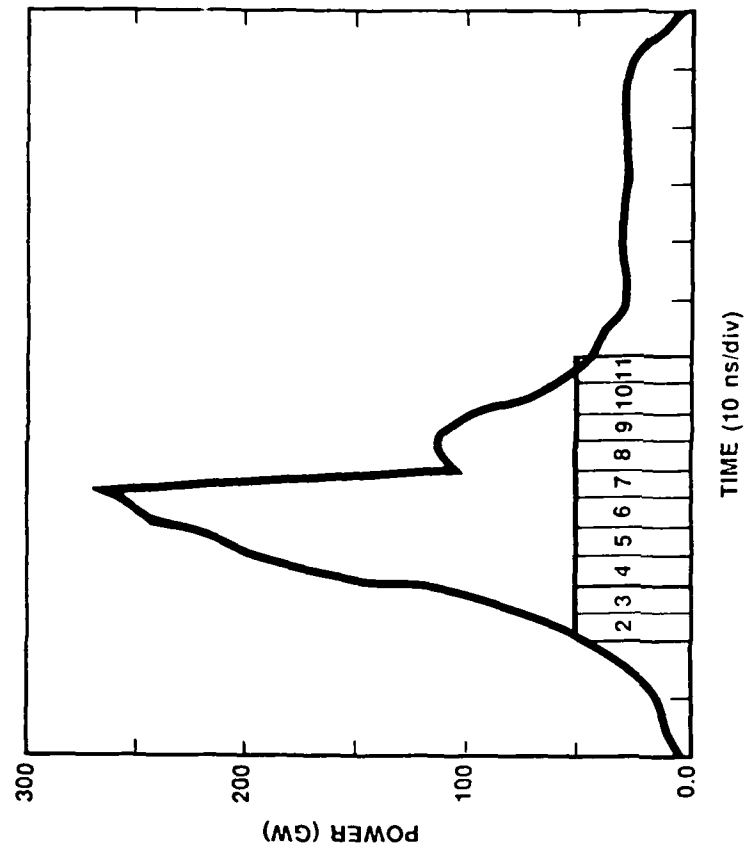


Figure 6a

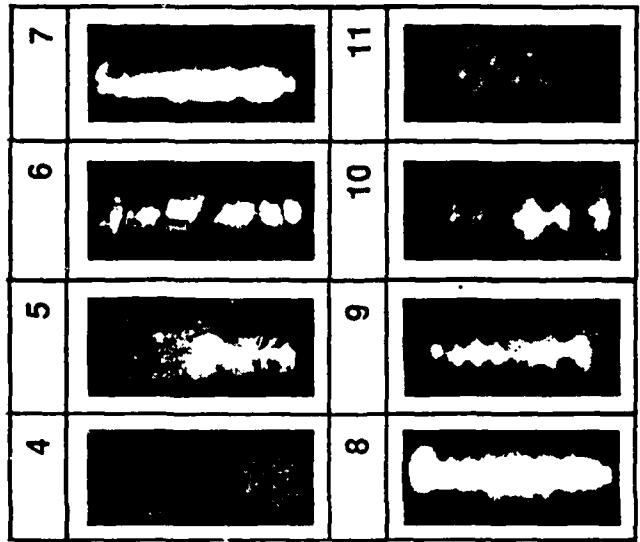
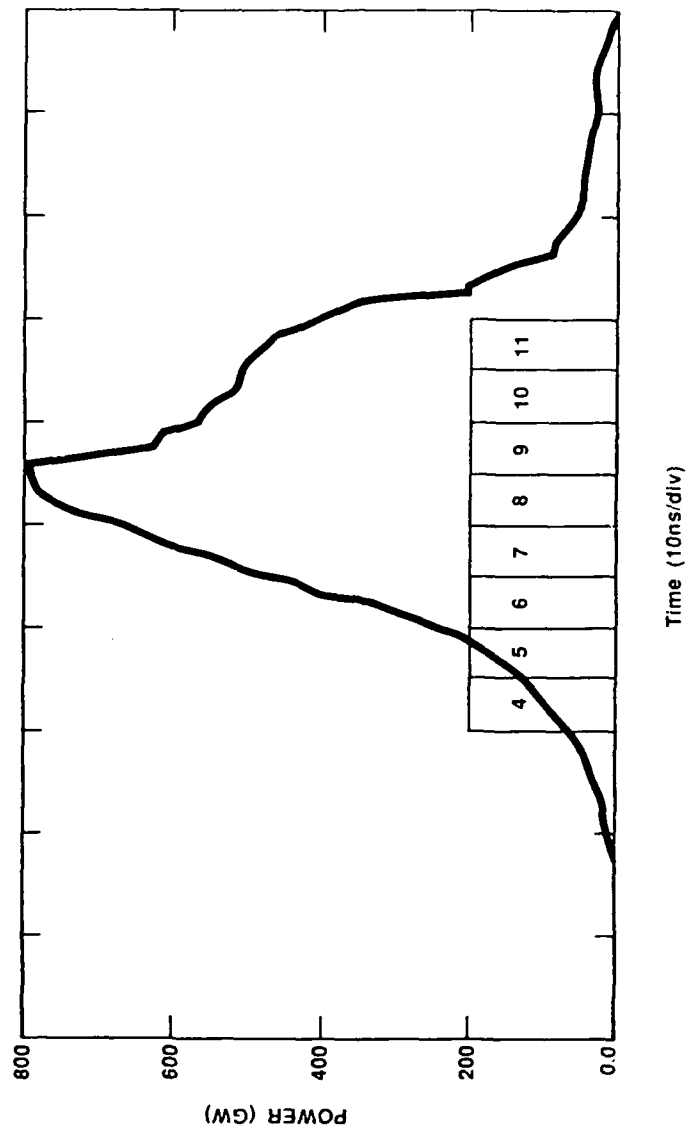
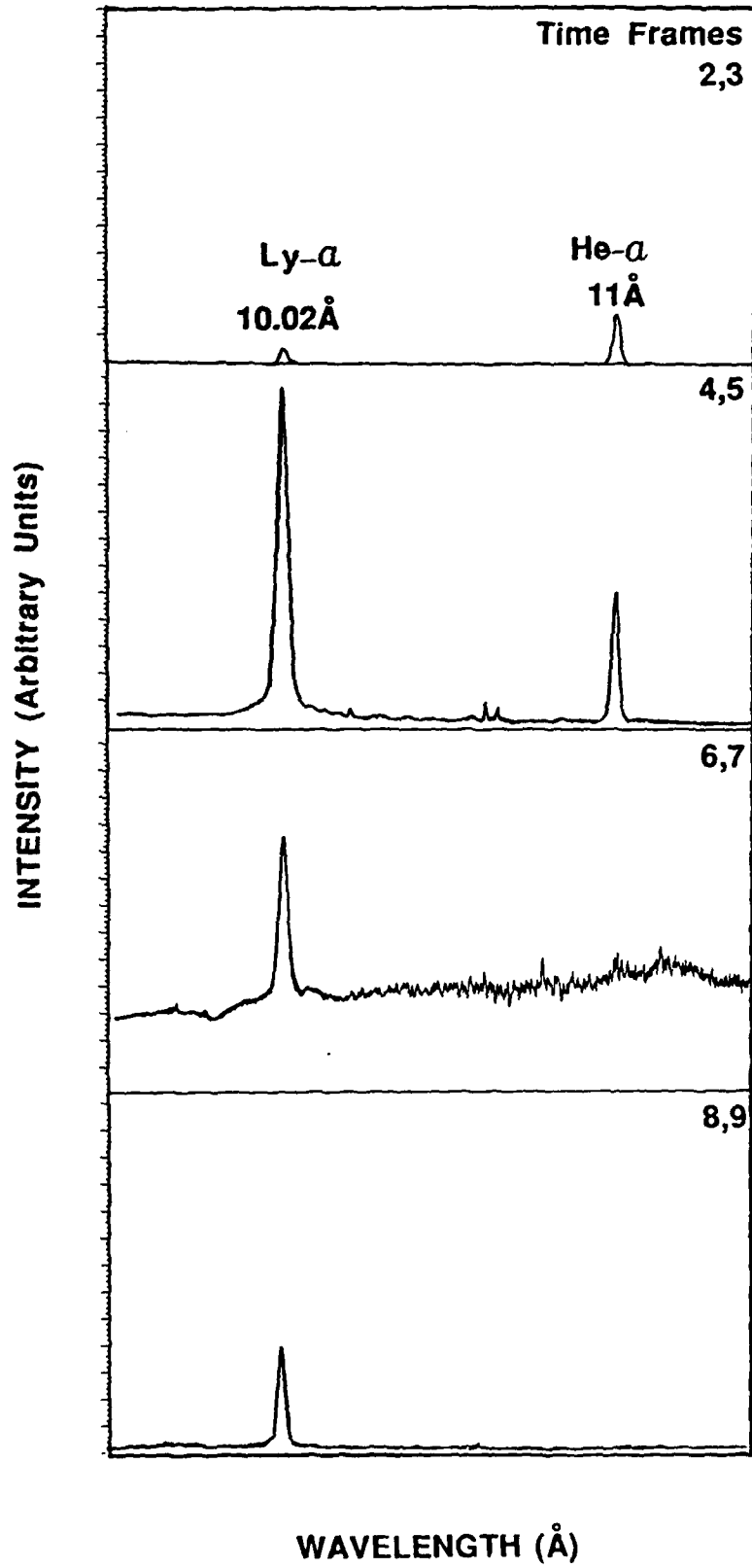


Figure 6b



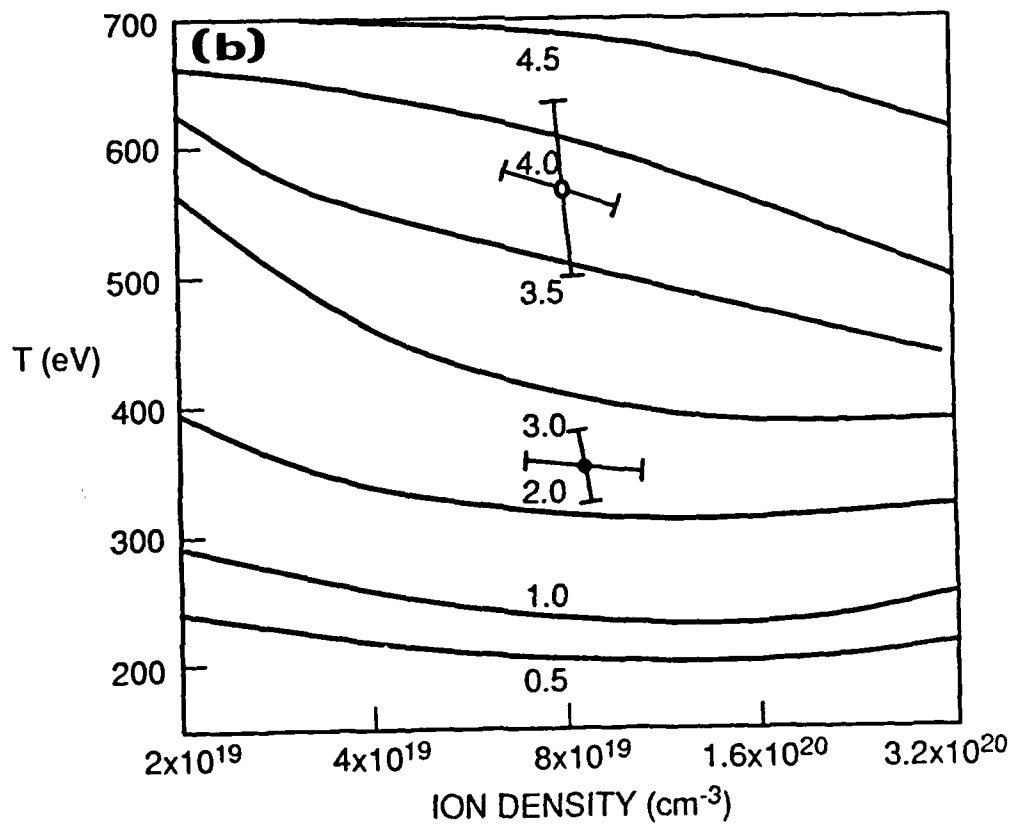
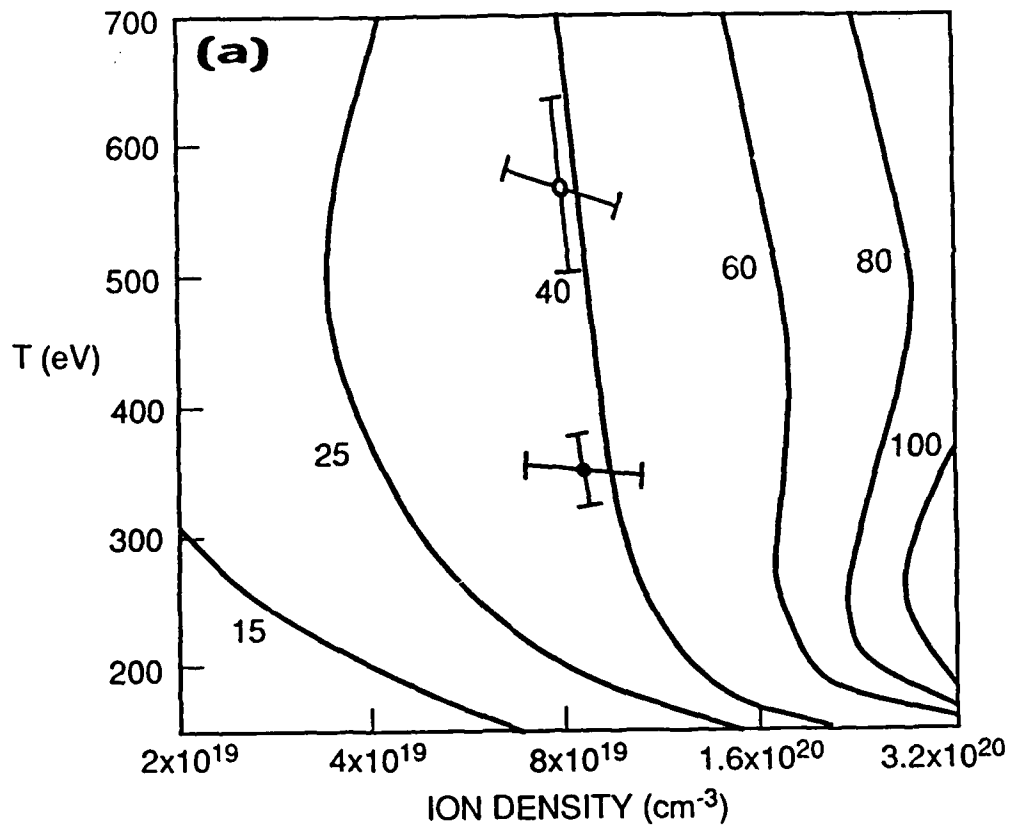


Figure 8

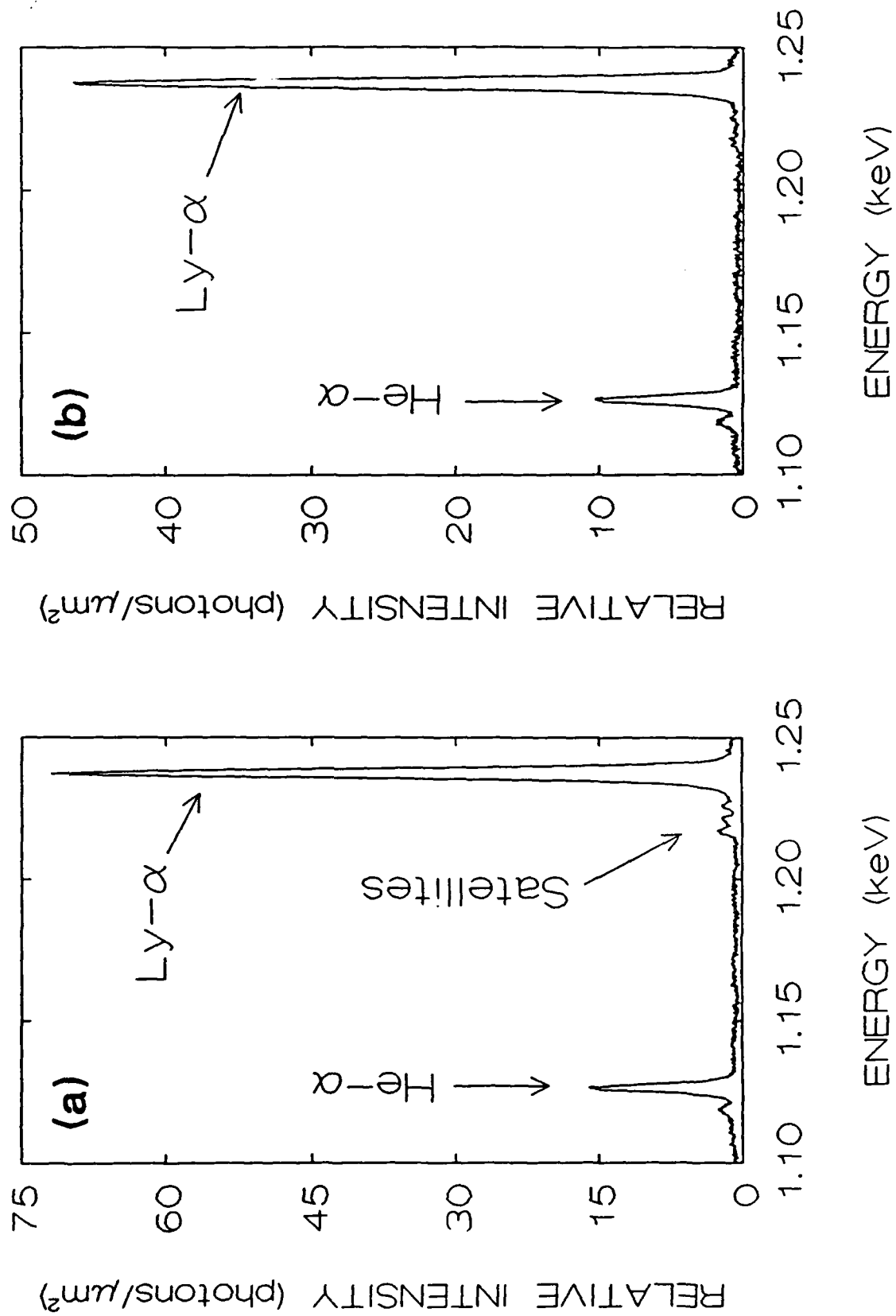


Figure 9

## APPENDIX B<sup>#</sup>

### Neon Plasma Conditions for Na/Ne Photopumping<sup>+</sup>

B.L. Welch,<sup>\*</sup> R.J. Commisso, H.R. Griem,<sup>\*</sup> and F.C. Young

**ABSTRACT:** Time-resolved UV and XUV emissions from a neon gas-puff Z-pinch were studied to determine conditions appropriate for Na/Ne photopumping. The UV spectrometer was calibrated in intensity with a deuterium lamp. Simultaneous measurements of Ne VIII 3s-3p (2821 Å) and 2s-3p (88.1 Å) lines were used to provide absolute XUV intensities by the branching-ratio technique. The neon plasma was produced on a teststand<sup>1</sup> under conditions similar to previous Na/Ne photopumping experiments.<sup>2</sup> Variations in UV and XUV emissions with gas-puff pressure, driving current, and current rise time will be presented.

# Presented at the 1990 APS Plasma Physics Division Meeting in Cincinnati, Ohio, November 14, 1990.

+ Work supported by IST/SDIO and directed by NRL.

\* Univ. of Maryland, College Park, MD 20742.

1. B.L. Welch et al., Bull. Am. Phys. Soc. 34, 1914 (1989).

2. F.C. Young, et al., Proc. Inter. Conf. on LASERS '88, R.C. Sze and F.J. Duarte, Eds. (STS Press, McLean, VA, 1989) p. 98.

Figure 1: Energy level diagram of Ne VIII and Ne IX showing the energy of the pumped level (Ne IX 1-4), the lasing levels (Ne IX 2-4, 2-3, 3-4), and levels of interest in this poster (Ne VIII 2-3). For Ne plasmas at temperatures of 50-100 eV, populations of the lithiumlike levels are closer to equilibrium than the heliumlike upper levels. Therefore, we focus on emissions from the excited levels of Ne VIII to determine the population of the Ne IX ground state.

Figure 2: Energy diagram of the  $n=2$  and  $n=3$  levels of Ne VIII. Measurements of the  $2s-3p$  transitions at 88 Å, and the  $3s-3p$  transitions at 2819-Å and 2858 Å are reported in this presentation.

Figure 3: Photograph of the experimental arrangement of the neon gas-puff Z-pinch with an opening switch. The gas puff is centered below the vertical extension on top of the 30-cm diameter horizontal vacuum chamber. Current is driven through the gas puff from a capacitor supply and plasma-opening-switch (POS) assembly on the left. Radiation from the imploded plasma is recorded through horizontal ports located in front and behind the vacuum chamber. A grazing incidence monochromator is in front and two absolutely calibrated UV monochromators are behind. Also, a calibrated optical multichannel analyzer (OMA) is used to record spectra at the exit of one UV spectrometer.

Figure 4: A time-integrated spectrum of Ne VIII lines from the neon gas-puff Z-pinch. The strong 2-3 lines correspond to the three transitions identified in Fig. 2. Higher series Ne VIII lines are also identified. Most of the lines not labeled are from Ne VII.

Figures 5 and 6: Time histories of the 88-Å (Ne VIII  $2s-3p$ ) line and the 2810 Å (neon continuum) radiation are compared for a discharge without a POS (Fig. 5) and with a POS (Fig. 6). Without the POS, the current risetime is about 1  $\mu$ s, and emission

from two implosions is observed, first at 0.5  $\mu$ s and then at 1.2  $\mu$ s. With the POS, the implosion is driven by a faster risetime current pulse, and emission is observed only from one implosion at about 0.8  $\mu$ s. Both the upstream and downstream currents are shown in Fig. 6. The spike on the 88-Å emission at switch opening is attributed to photomultiplier pickup due to high voltages induced by the large downstream  $dI/dt$  at opening. Note that the relative intensities of the UV and 88-Å emissions have different temporal variations. Spectral measurements (to be described) were made with the OMA at the timings indicated by the circled numbers.

Figures 7 and 8: To compare the Ne VIII 2s-3p and 3s-3p line emissions, continuum must be subtracted from the 3s-3p (UV) measurement. In Fig. 7, time histories on (2820 Å) and off (2810 Å) the 3s-3p line are compared. The difference between these signals corresponds to the Ne VIII 3s-3p line. At the first implosion, the emission is nearly all continuum, while at the second implosion, significant 2820-Å emission is observed. The difference between these signals is compared with the 2s-3p line (88-Å) emission in Fig. 8. Emission at both 2820 Å and 88 Å is observed at the second implosion. The reproducible correlation from shot-to-shot of these two emissions at the second implosion indicates significant population of Ne VIII excited states and probably the Ne IX ground state at this time.

Figures 9, 10, 11 and 12: Spectra of the UV emission near 2820 Å were measured with the OMA at different times during the implosions. The OMA was gated on for 100 ns. Spatially resolved spectra corresponding to the times indicated in Figs. 5 and 6 are shown in Figs. 9, 10 and 11. At time 1 (Fig. 9), the spectra have strong lines identified as transitions in Ne III, and the diameter of the plasma is 3.5 mm. At time 2 (Fig. 10), no spectral lines are observed; the emission consists of an intense continuum, and the plasma diameter is 1 mm. At time 3 (Fig. 11), two weak spectral lines from Ne VIII are observed, and the plasma

diameter is 4 mm. The size of this plasma and the absolute intensity of this emission are used to estimate the Ne VIII population fraction. A spectrum at time 3, spacially integrated to improve the signal-to-background ratio, is shown in Fig. 12. The two spectral lines observed here correspond to 3s-3p transitions of Ne VIII (see Fig. 3). The ratio of these two lines is 2:1 as expected for an optically thin plasma. The line width of 4 Å is used to determine the electron density in the plasma.

Figures 13, 14, 15 and 16: Emissions from Ne VII, Ne VIII and Ne IX are compared to estimate plasma temperatures and to determine the experimental conditions for optimum Ne IX ground-state population. The plenum pressure in the gas puff is varied to control the initial Ne mass in these implosions. Time histories of Ne VII and Ne VIII emissions, measured on the same shots, are compared in Figs. 13 and 14. For Ne VII, the 2s2p-2s3d (106 Å) transition is used, and this emission is observed from both implosions. For Ne VIII, the 3s-3p (2820 Å) radiation with continuum subtraction is used. Here the Ne VIII measurements at the first implosion are unreliable due to the large continuum. At the second implosion, the Ne VIII emission is reliable and is more intense for lower plenum pressure. Time histories of Ne VIII and Ne IX emissions, measured on the same shots, are compared in Figs. 15 and 16. For Ne VIII, the 2s-3p (88 Å) transition is used. This emission is observed for both implosions, but is more intense for the second implosion at lower plenum pressure. For Ne IX, a Ni-cathode vacuum x-ray diode and filter (0.5- $\mu$ m Al + 1.8- $\mu$ m Kimfol) are used. This detector sensitivity is optimum for 1-keV neon K-shell radiation. Ne IX emission is also observed for both implosions.

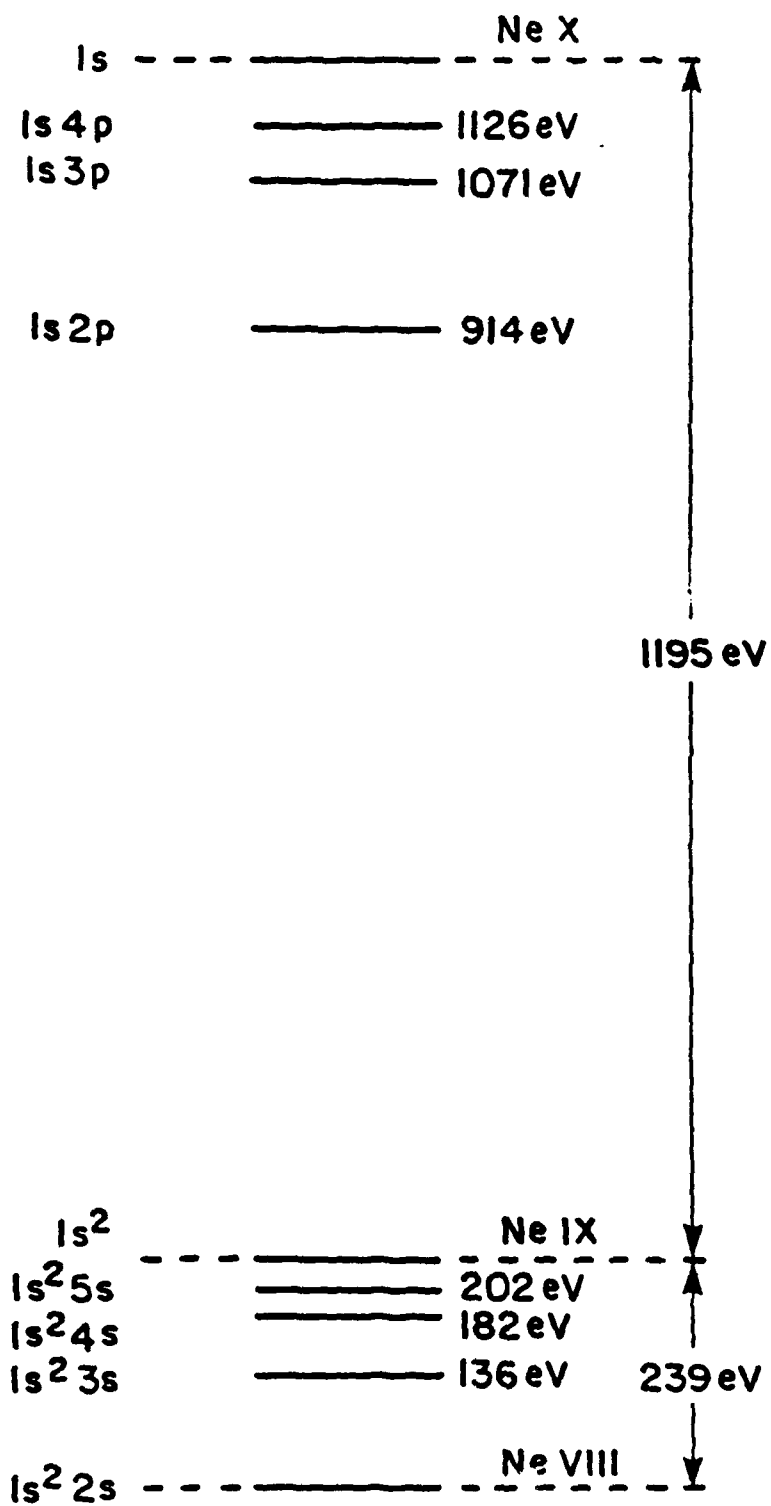
Figures 17 and 18: A comparison is made of the Ne VIII emission without (Fig. 17) and with (Fig. 18) the POS. Time histories of the Ne VIII 2s-3p line emission and current traces are given for plenum pressures of 50 and 150 psi. The implosions occur later

in time for higher plenum pressure (i.e., larger mass) in Fig. 18 and for the second implosion in Fig. 17.

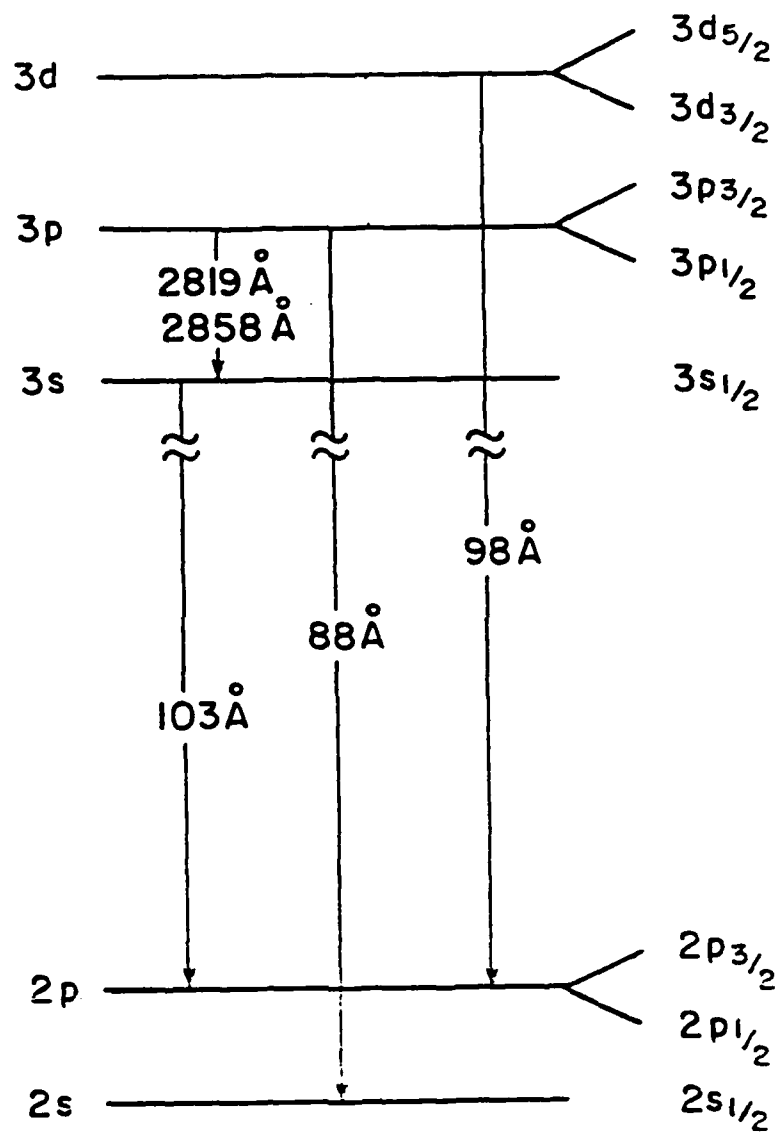
Figures 19 and 20: A comparison is made of the Ne VIII emission for different risetime currents. Time histories of the Ne VIII 2s-3p line emission and current traces are given for 100-ns risetime (Fig. 19) and 50-ns risetime (Fig. 20) currents. The current risetime is controlled by adjustments in the POS. The implosions occur earlier in time for larger current are expected, and the Ne VIII emission is larger for the slower risetime current.

Figures 21 and 22: Properties of the imploded Ne plasma deduced from the quantitative measurements are given in Fig. 21. At the second implosion (without the POS), the electron temperature is 75 eV; the electron density is  $6 \times 10^{18} \text{ cm}^{-3}$ ; and the Ne IX ground-state fraction is about 37% based on a Saha equilibrium atomic physics model. Several scalings of the Ne VIII emission determined from the relative measurements are given in Fig. 22. To increase the Ne VIII emission, smaller mass (50-psi plenum pressure), larger current (190 kA), and slower risetime current (100 ns) are indicated.

# Level Diagram for Ne VIII and Ne IX



# BRANCHING-RATIO MEASUREMENT



Ne VIII

Figure 2

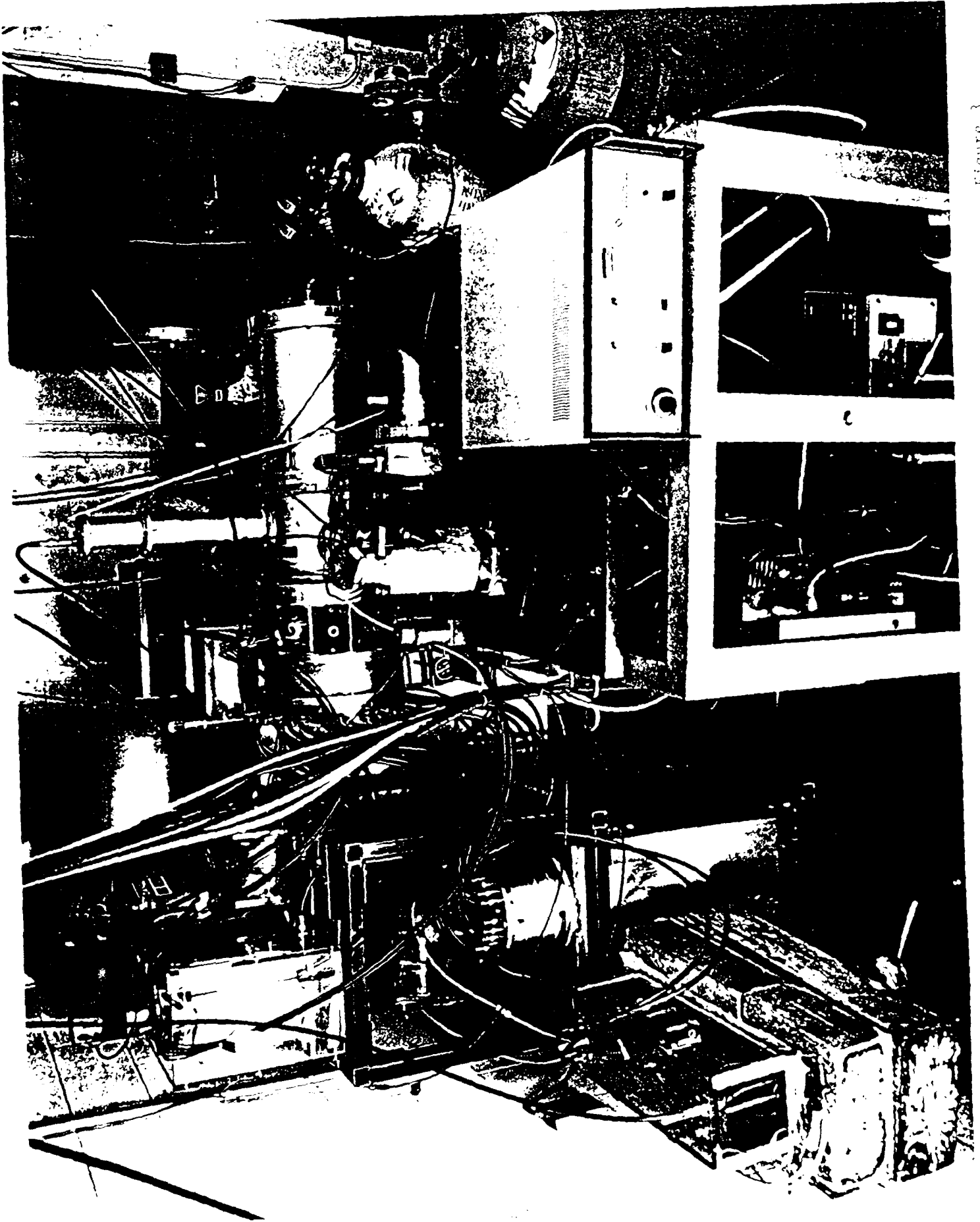


Figure 3

# GRAZING INCIDENCE SPECTRA OF IMPLoded NEON

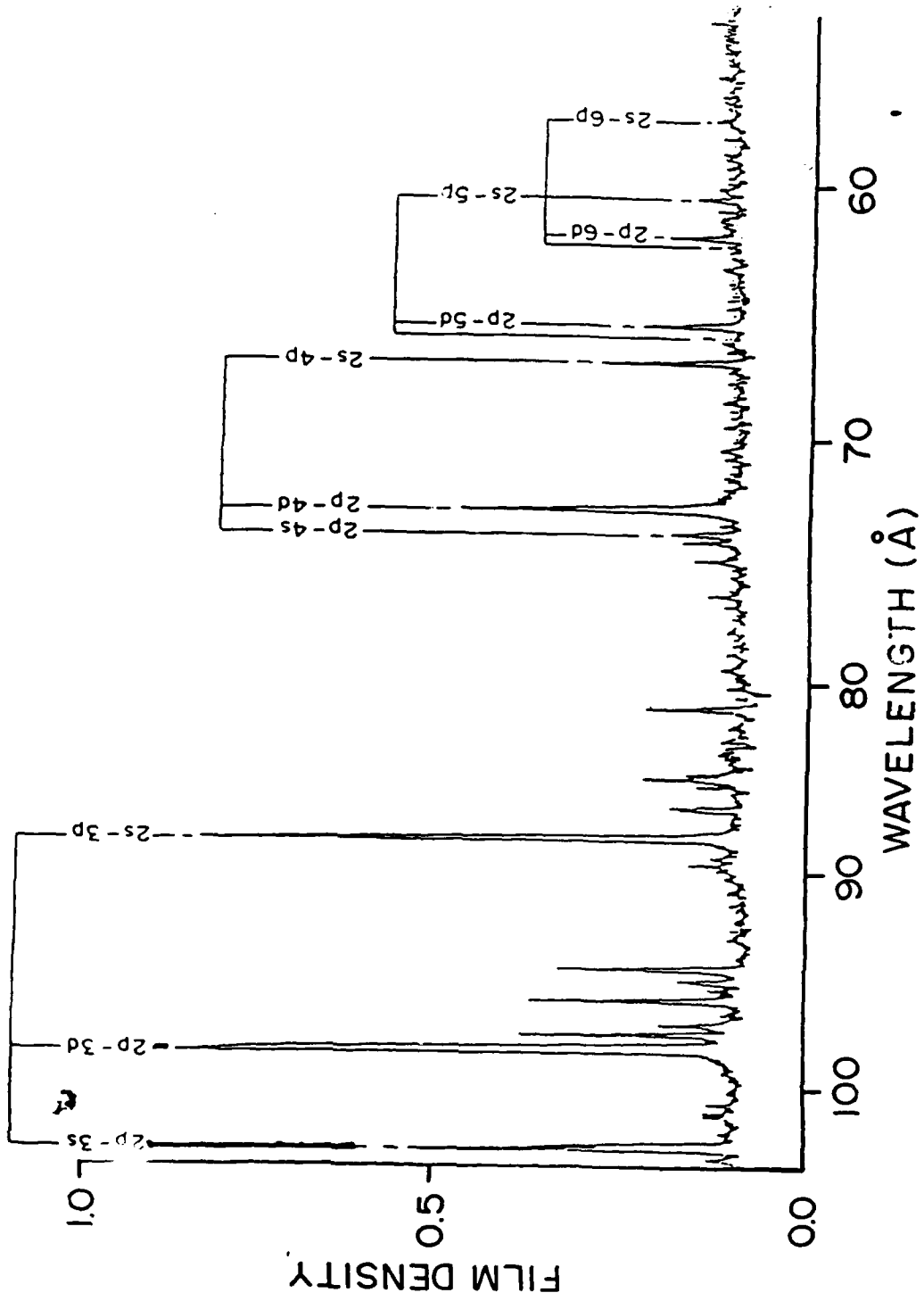
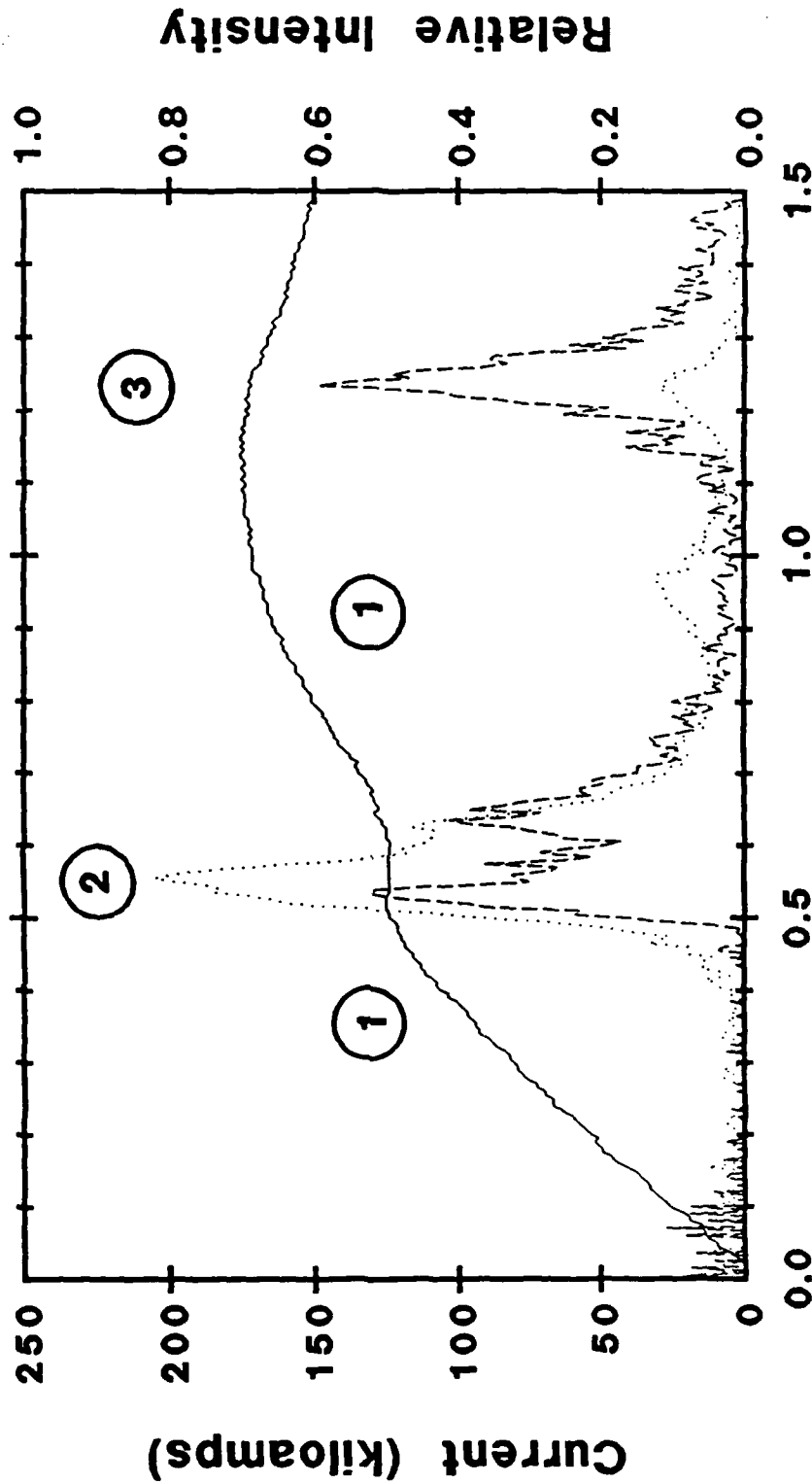


Figure 4

# NEON EMISSION

( O indicates OMA timing)



# NEON EMISSION WITH PLASMA OPENING SWITCH

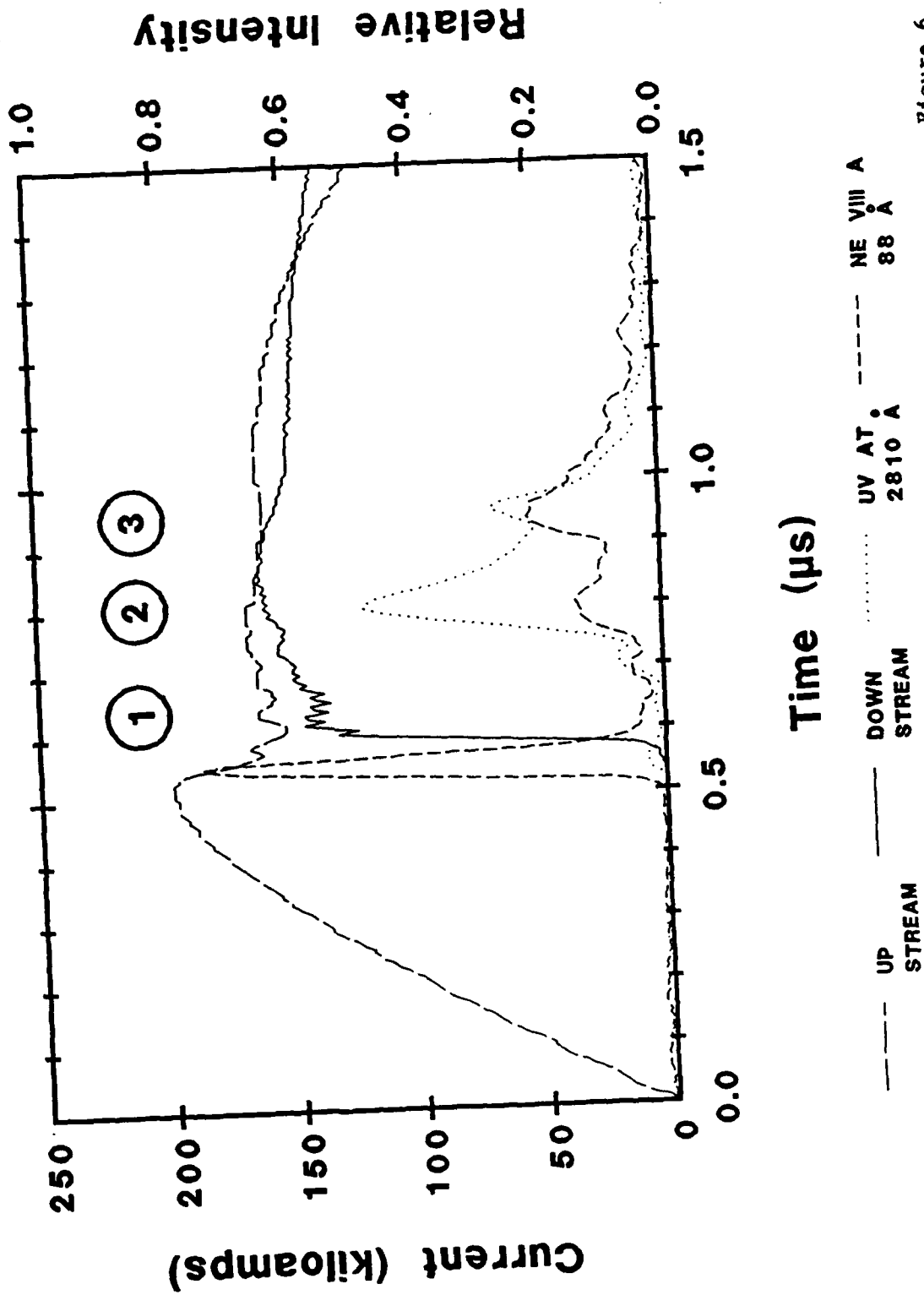
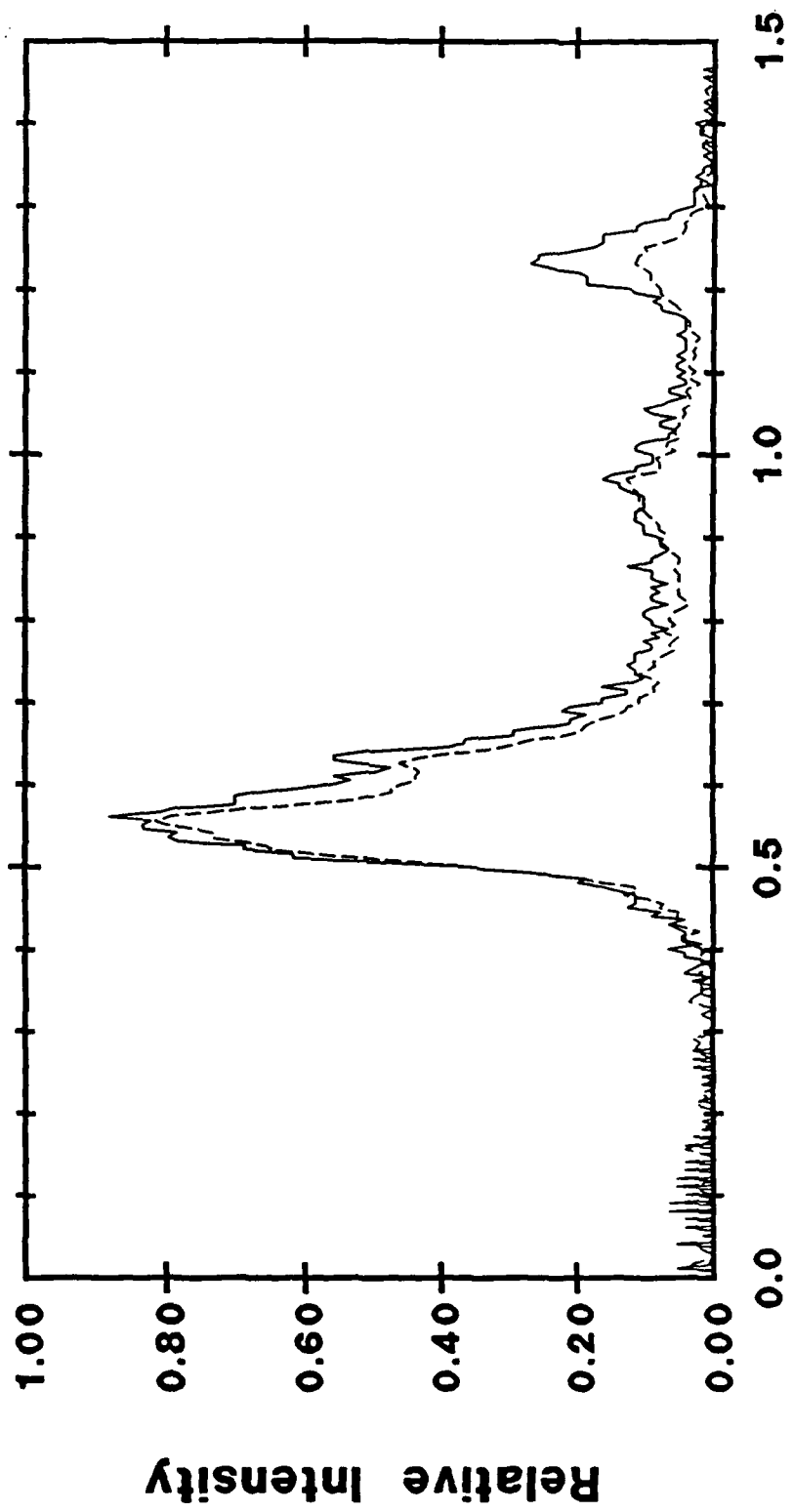


Figure 6

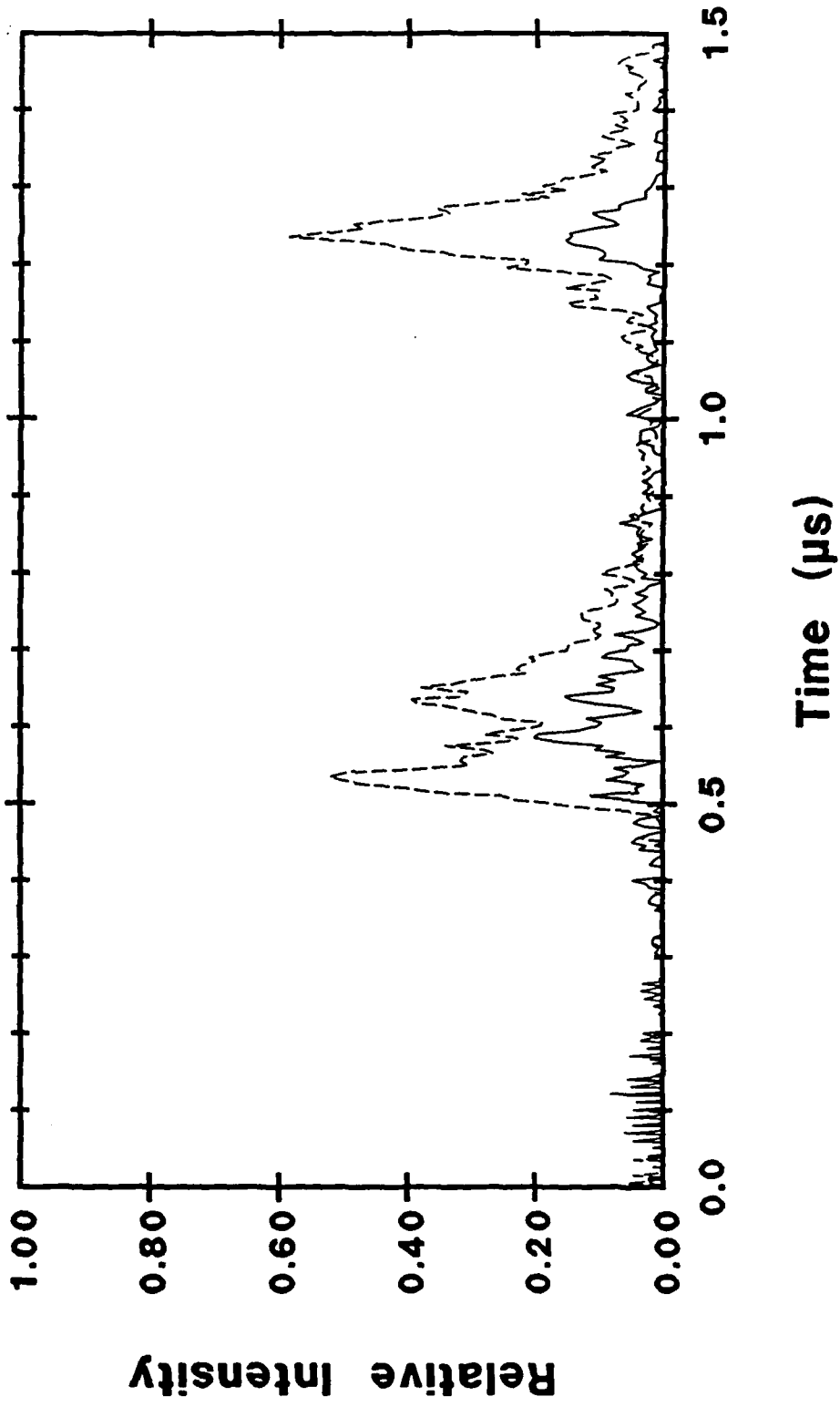
# NEON VIII EMISSION 3S-3P TRANSITION



— UV AT 2820 Å  
- - - UV at 2810 Å

Figure 7

# NEON VIII EMISSION nS-3P TRANSITIONS



— DIFFERENCE  
2820-2810 Å

----- XUV AT  
88 Å

Figure 8

# NE III EMISSION SPATIALLY RESOLVED

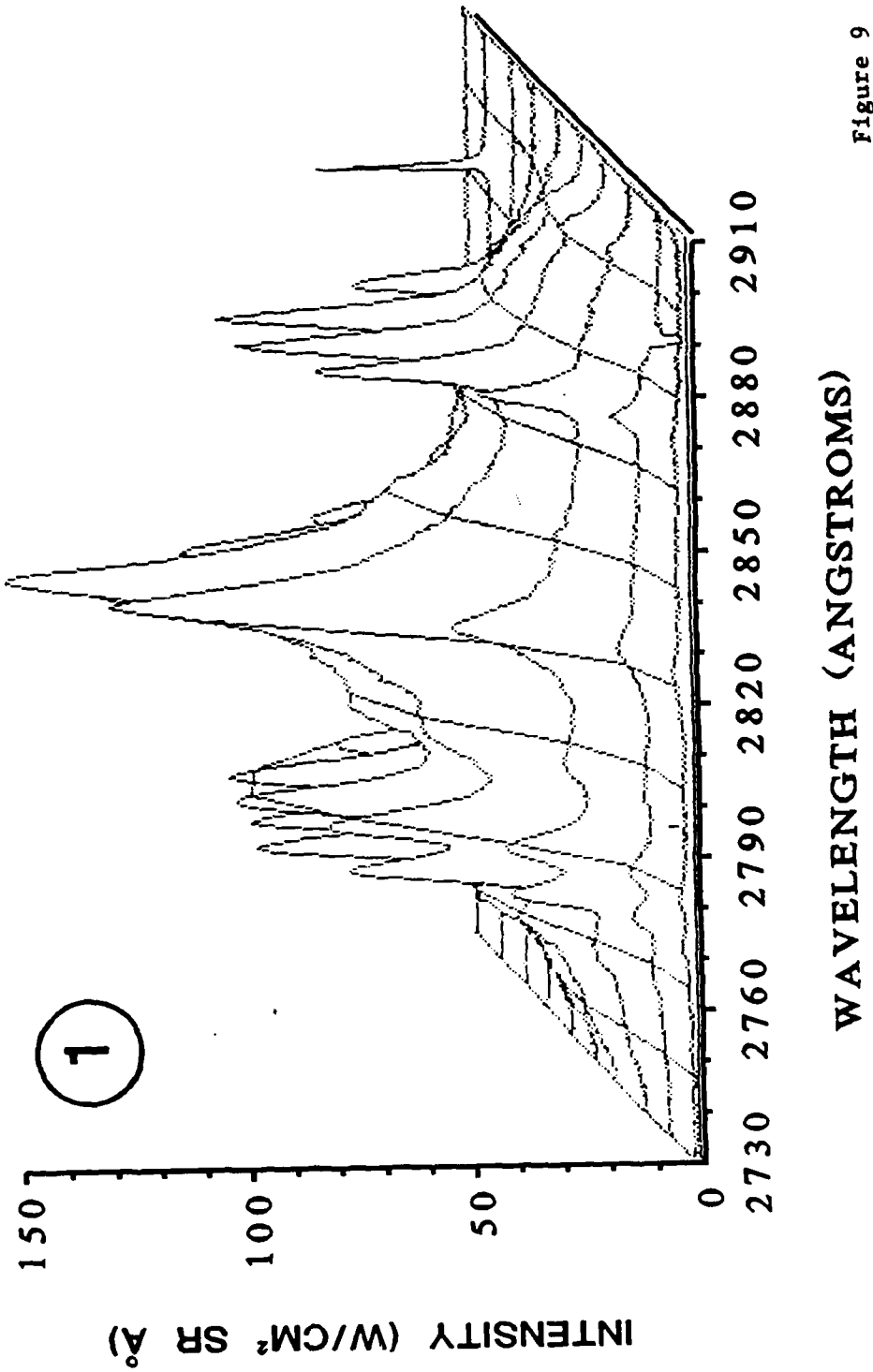


Figure 9

# NEON EMISSION SPATIALLY RESOLVED

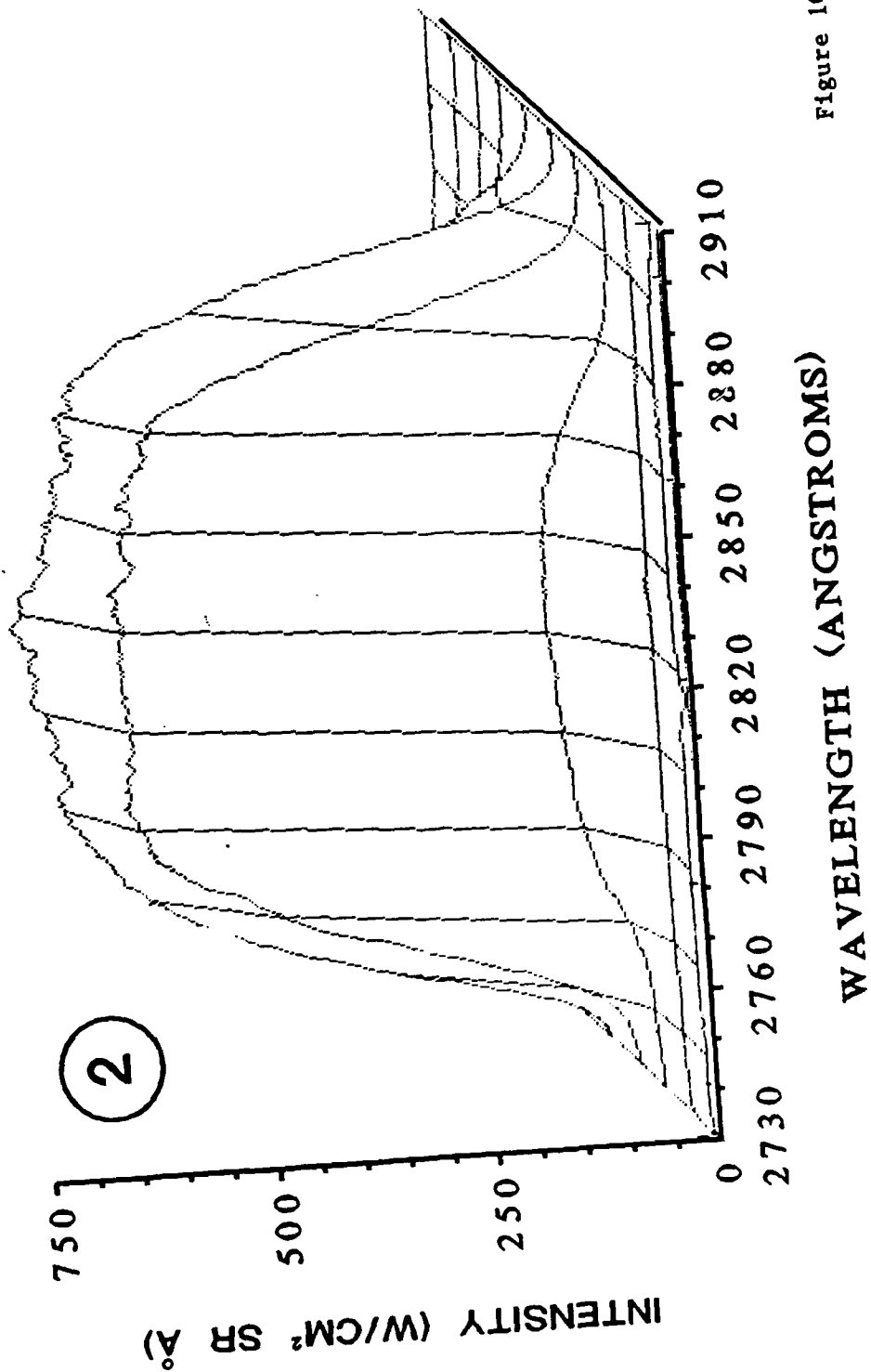
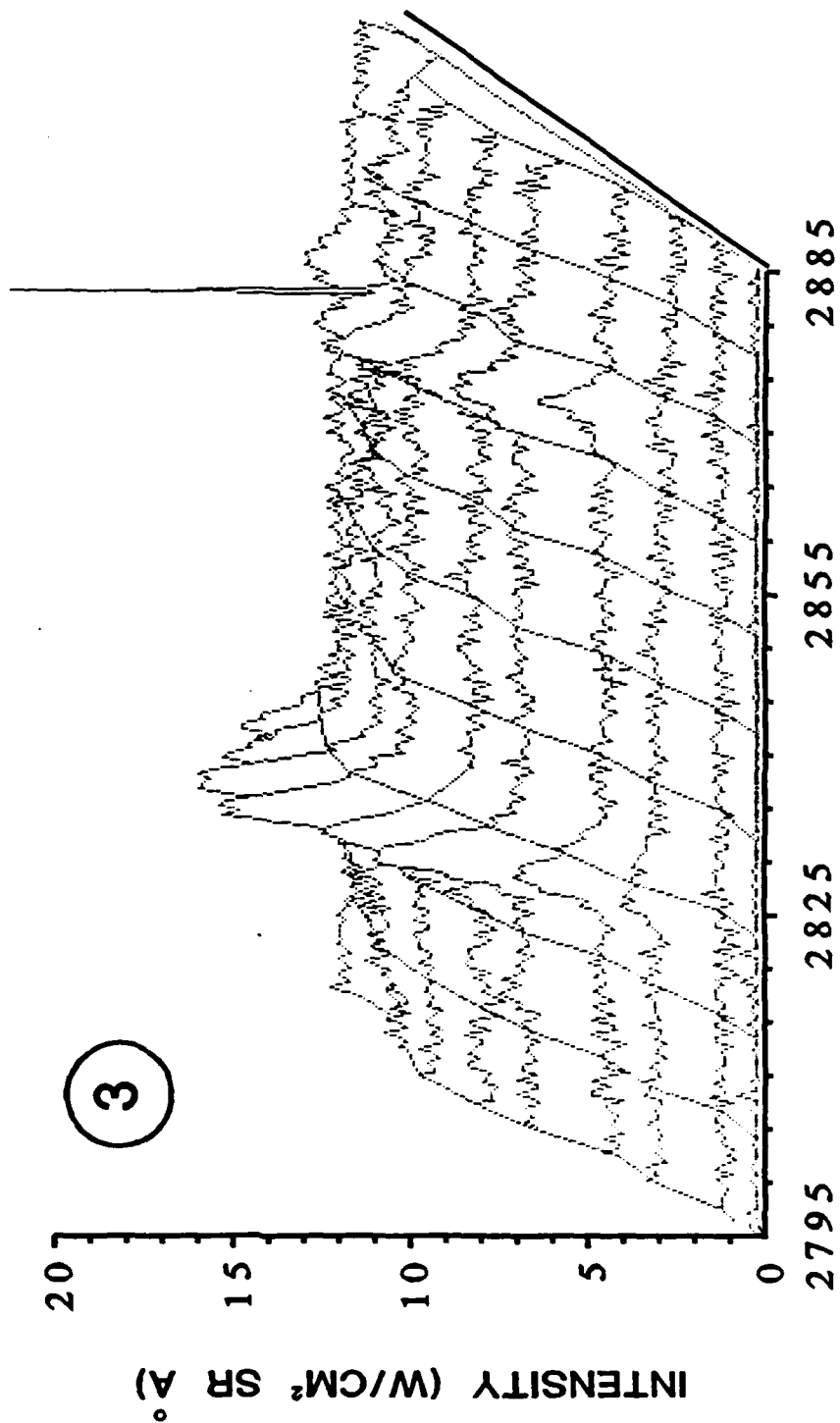


Figure 10

# NE VIII EMISSION SPATIALLY RESOLVED



WAVELENGTH (ANGSTROMS)

Figure 11

# NE VIII EMISSION SPATIALLY INTEGRATED

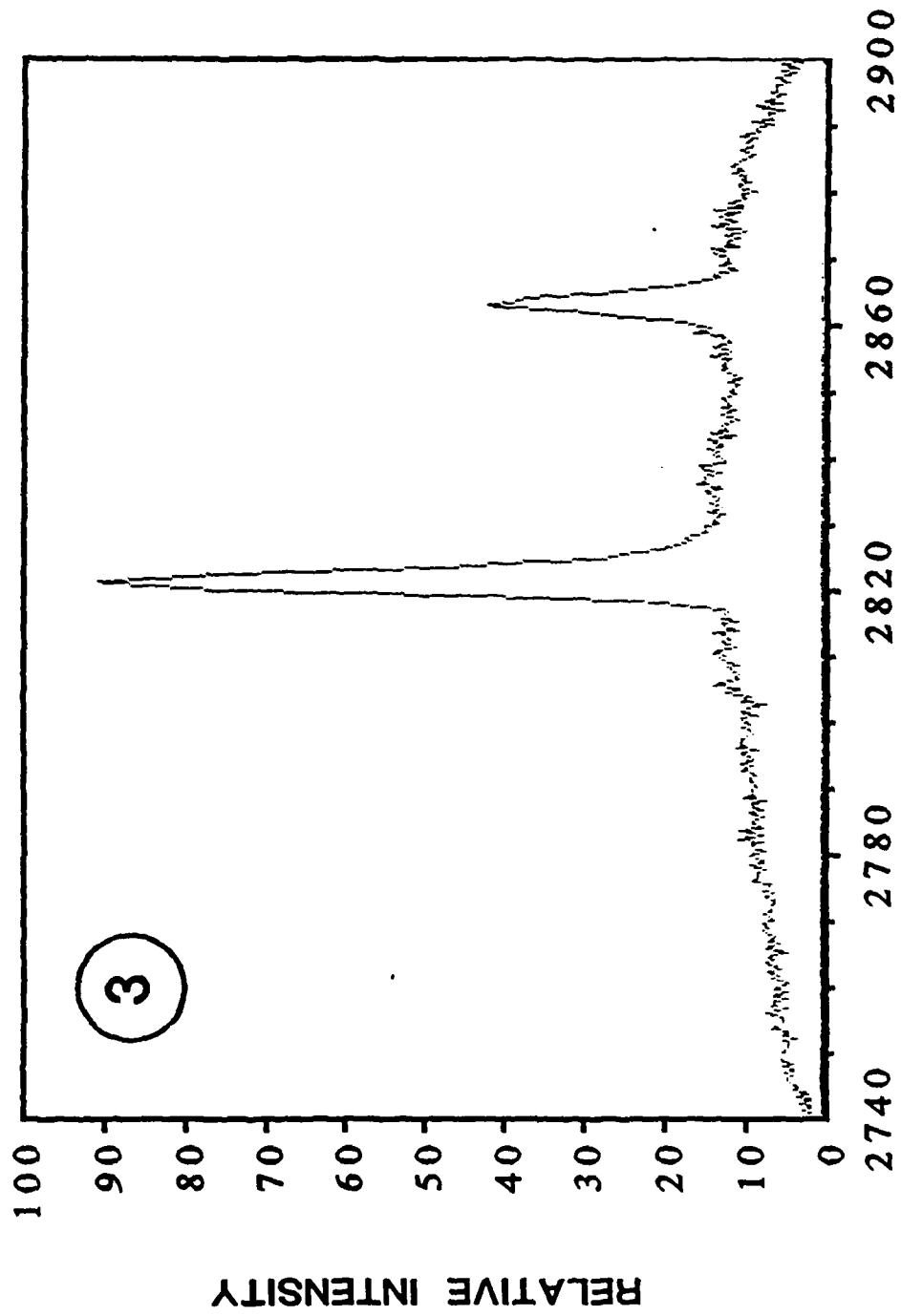


Figure 12

# NEON VII EMISSION 2S2P-2S3D TRANSITION

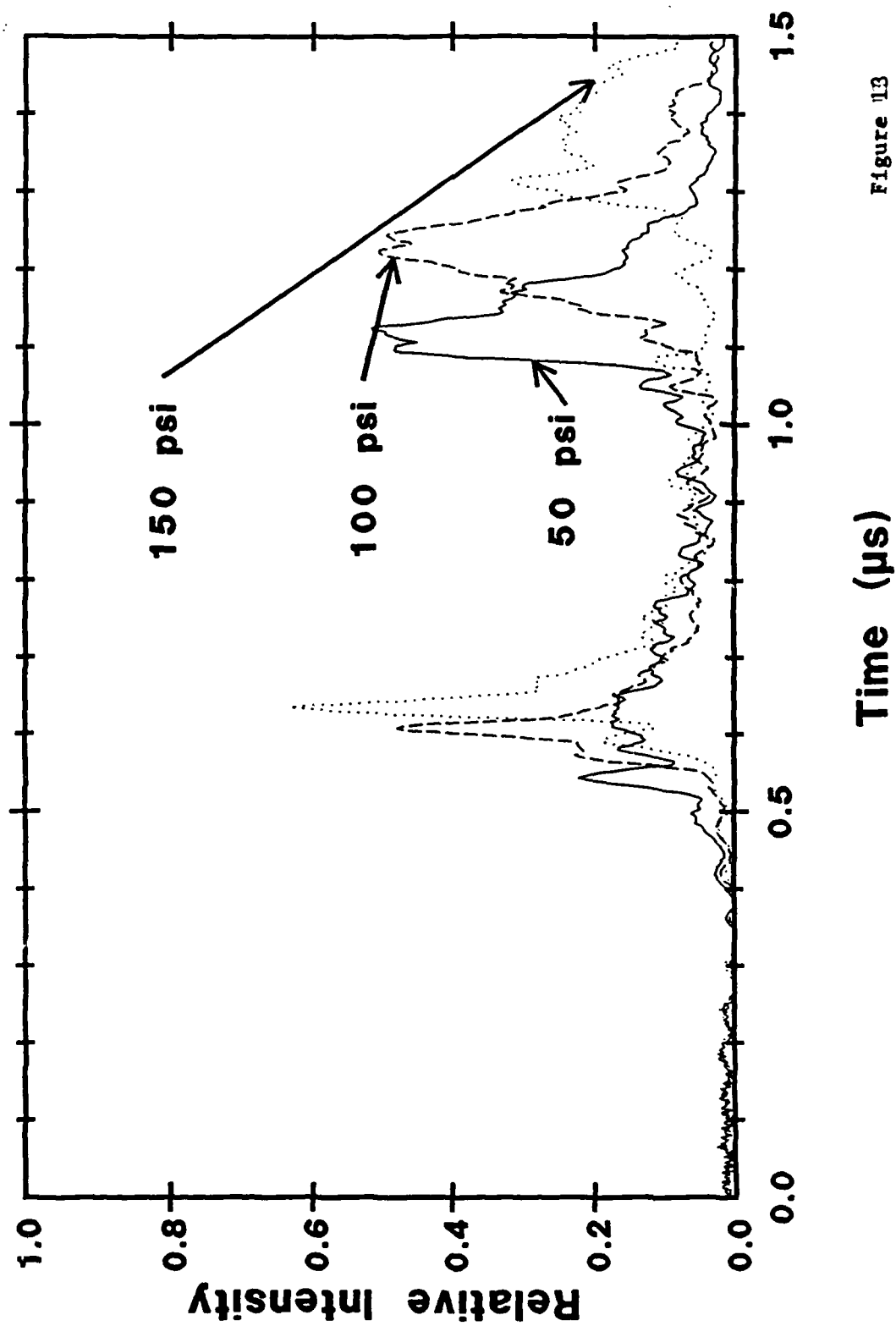


Figure 13

# NEON VIII EMISSION 3S-3P TRANSITION

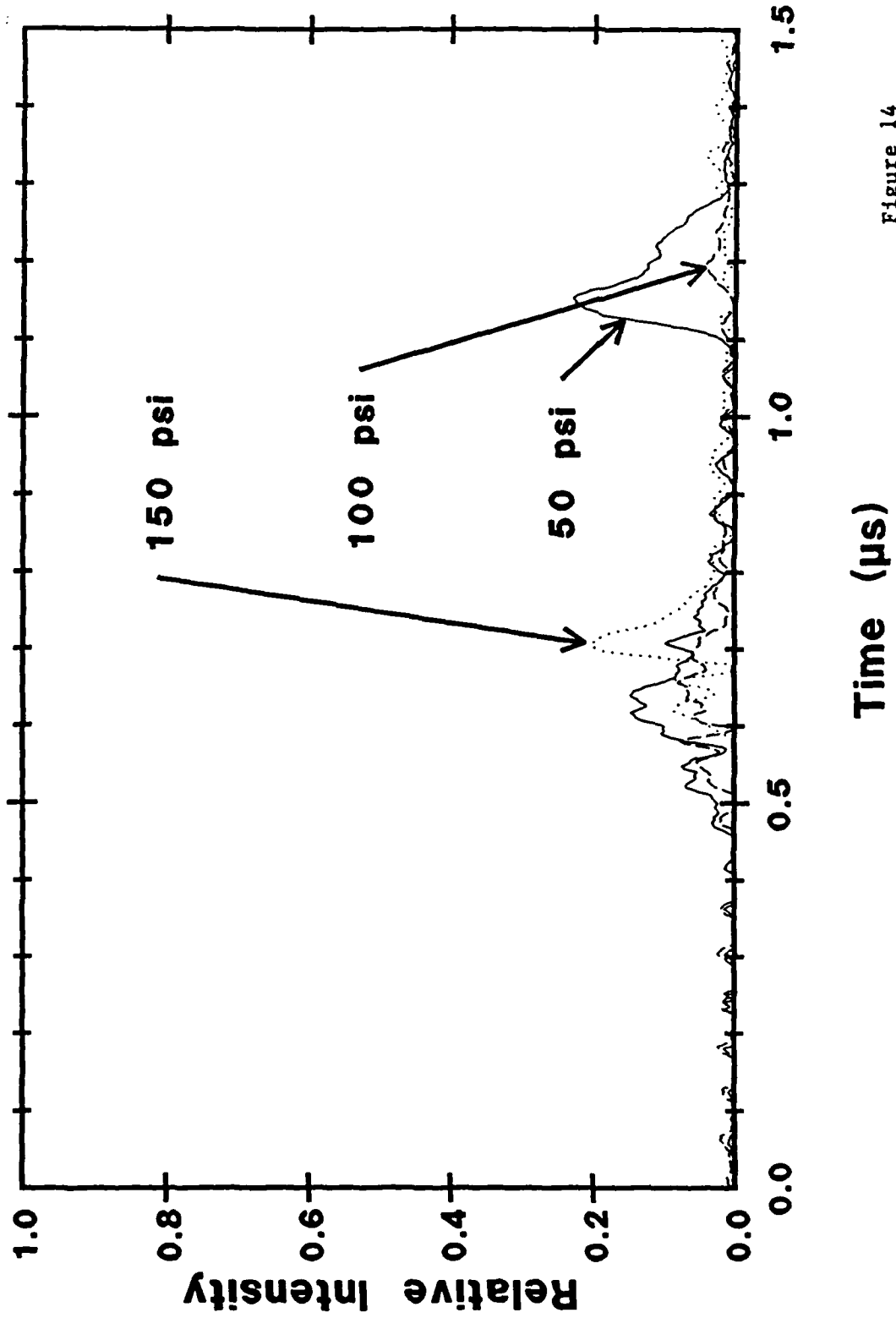


Figure 14

# NEON VIII EMISSION 2S-3P TRANSITION

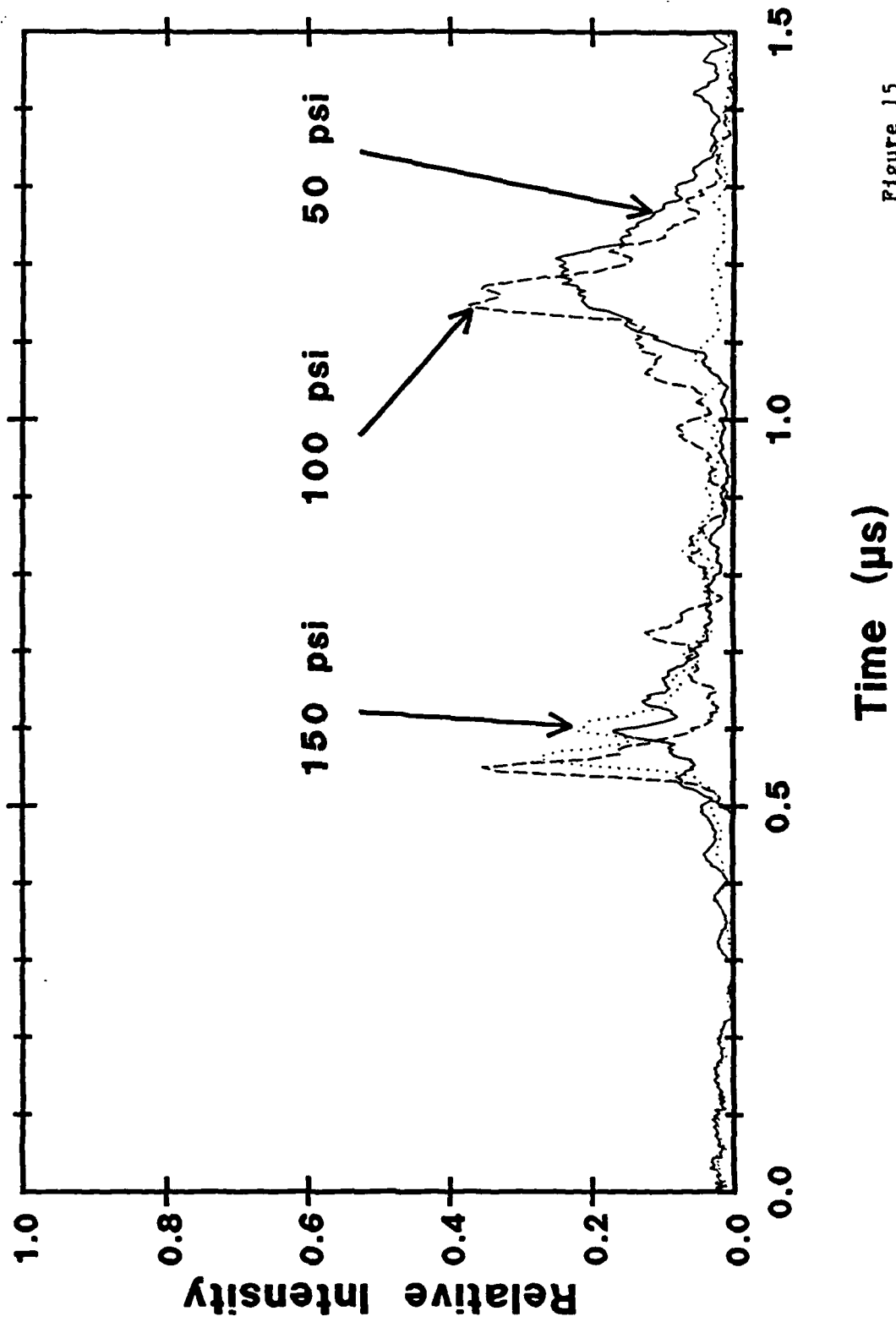


Figure 15

# NEON K-SHELL EMISSION FILTERED VACUUM DIODE

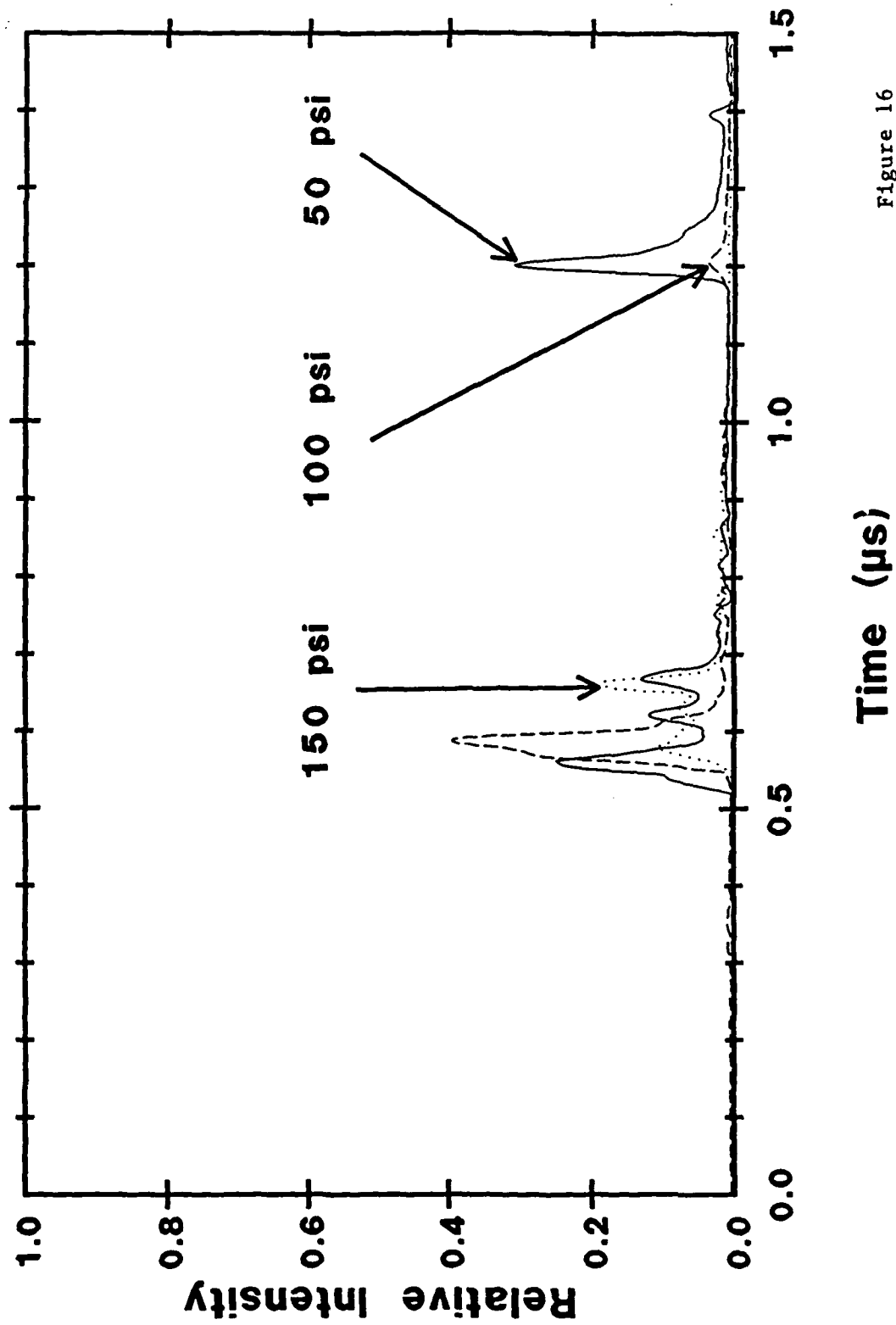
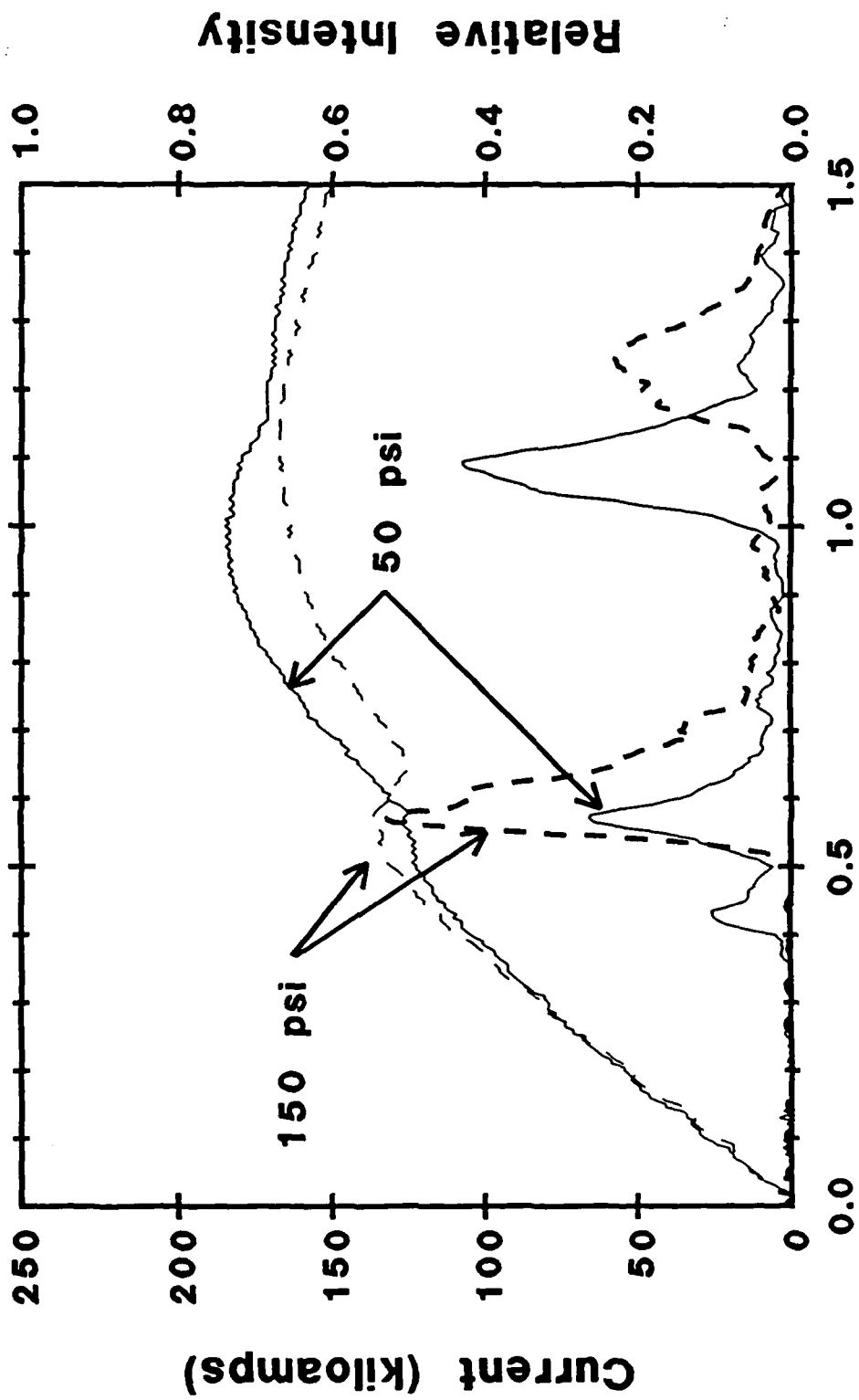


Figure 16

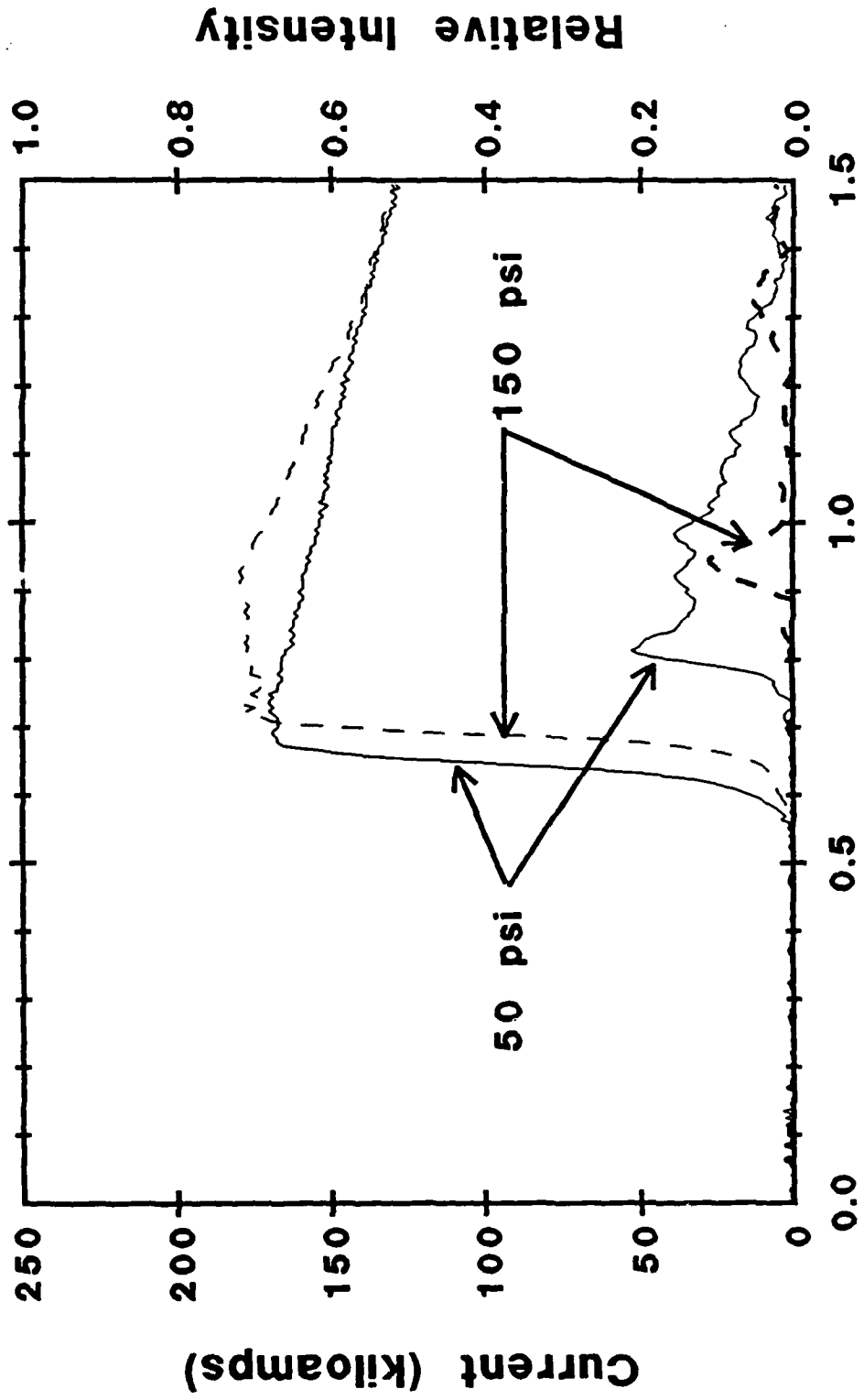
# NEON EMISSION FOR 2S-3P TRANSITION



Time ( $\mu\text{s}$ )

Figure 17

# NEON EMISSION FOR 2S-3P TRANSITION



Time ( $\mu$ s)

Figure 18

# NEON VIII EMISSION FOR 100 PSI

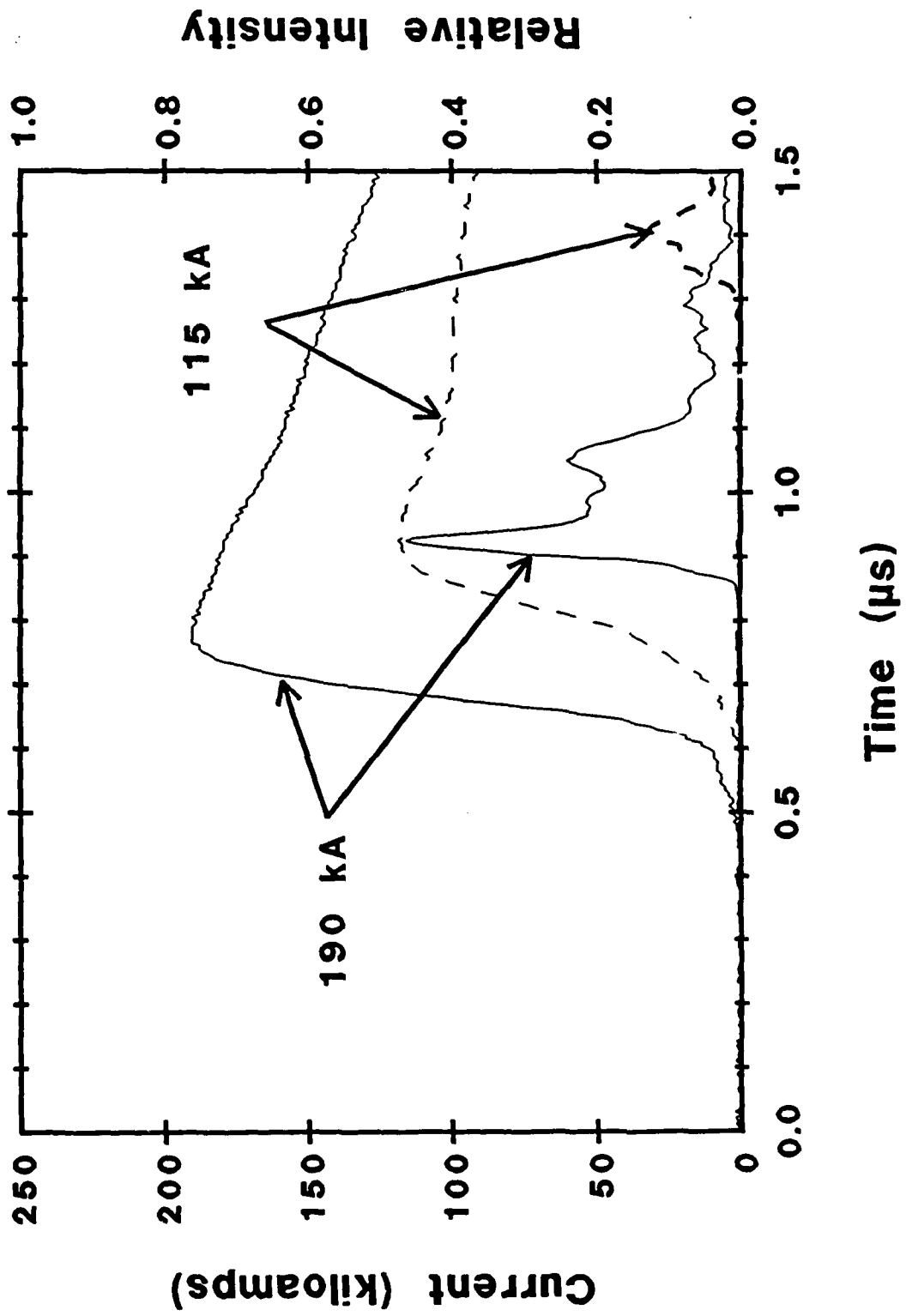


Figure 19

# NEON VIII EMISSION FOR 100 PSI

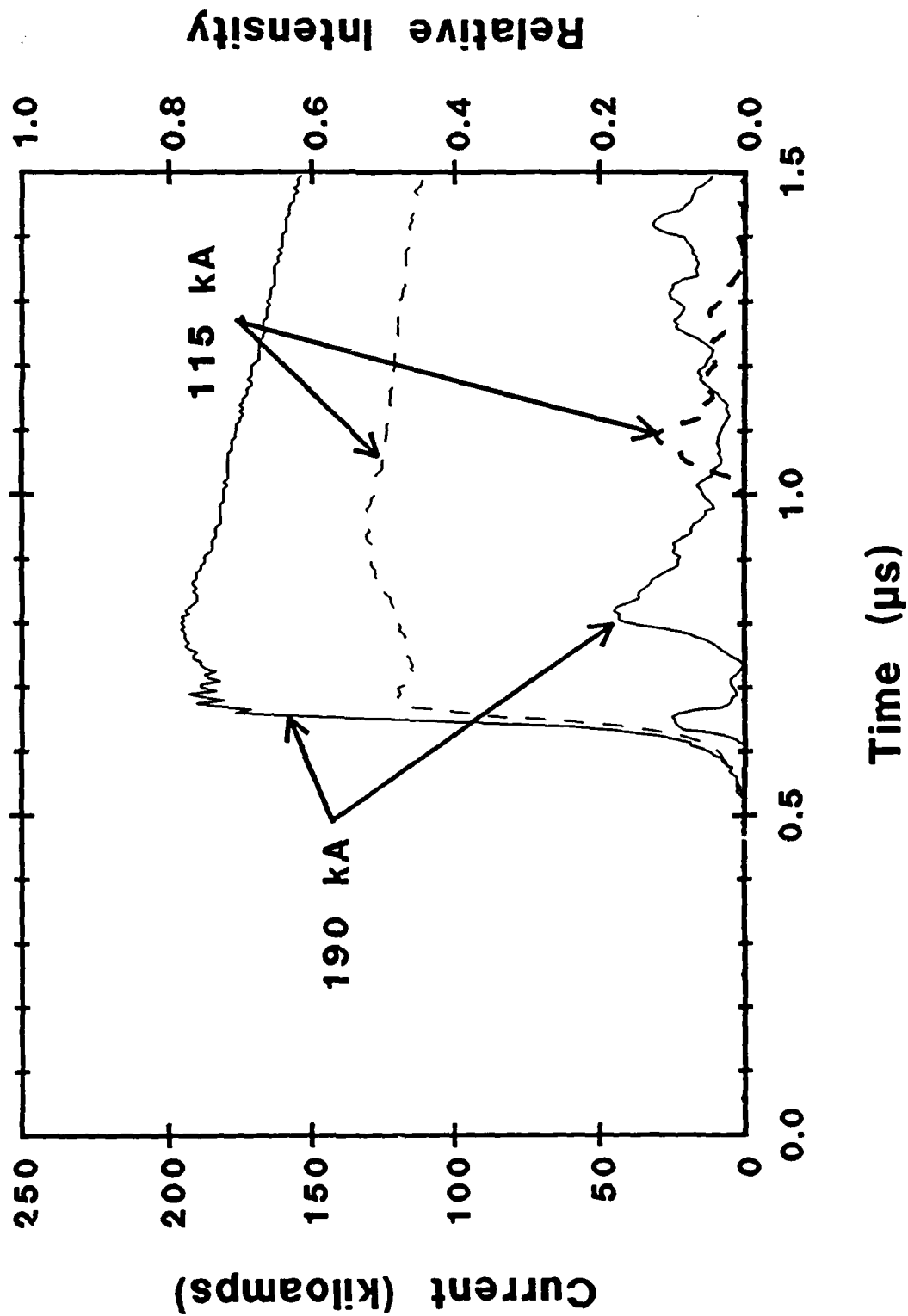


Figure 20

## CONCLUSIONS

1. Plasma Conditions at Second Implosion
  - \* Electron temperature of 75 eV inferred from ionization stages observed.
  - \* Electron density of  $6 \times 10^{18} \text{ cm}^{-3}$  deduced from Ne VIII 3s-3p line width.
  - \* Heliumlike Ne ground-state fraction of 37% inferred from 3s-3p line absolute intensity.

## **2. Slow-Risetime Current Implosions**

- \* Two implosions observed**
- \* As mass is increased, intensity of NeVIII emission - increases for first implosion. - decreases for second implosion.**
- \* As current is increased, NeVIII emission increases for both peaks.**

## **3. Fast-Risetime Current Implosions**

- \* Voltage spike observed at switch opening.**
- \* Intensity of NeVIII emission increases for - smaller mass - larger current - slower risetime current.**

Improving Plasma Uniformity in Z-Pinch Driven  
Neonlike Krypton X-Ray Lasers

J. W. Thornhill, J. Davis, J. P. Apruzese, and R. Clark

Naval Research Laboratory  
Radiation Hydrodynamics Branch  
Washington, D.C. 20375-5000  
Phone (202) 767-9299

Abstract - Maintaining plasma uniformity is an essential requirement for successful x-ray laser designs. In this work, we focus on a z-pinch driven neonlike krypton x-ray laser design for which we: 1) investigate the role initial mass loading plays in affecting plasma uniformity and gain, and 2) show there are advantages in terms of plasma uniformity to diluting a krypton plasma with a low z material such as helium. These results are obtained using a 1D radiation hydrodynamic model. The results of this study show that low mass 100 percent Kr plasmas are optimal for achieving significant gain while maintaining plasma integrity. Diluting a Kr plasma with He has the advantage of improving plasma uniformity but it has the disadvantages of enhanced collisionality and line broadening associated with the additional free electrons.

## I. INTRODUCTION

There have been several experiments that utilized pulsed power driven z-pinch implosions to heat and compress plasmas to attempt to achieve conditions conducive to gain for an x-ray laser. At Physics International Corporation an experiment was recently performed in which a krypton gas puff was imploded onto another krypton gas puff located on axis.<sup>1,2</sup> Sandia National Laboratories has succeeded in obtaining an apparent inversion in heliumlike neon using a novel design in which the radiation from a z-pinch imploded sodium plasma is used to both heat and photopump an isolated neon plasma.<sup>3</sup> The success of both experiments depends on being able to control the heating and compression of the gain medium in such a way that an adequate degree of plasma uniformity is maintained. Sandia achieved this goal by insulating the lasing plasma from being perturbed by MHD effects of the imploded sodium plasma. Physics International based their x-ray laser design on imploding onto a low density krypton gas in order to provide uniformity and localize the gain region. This is similar to a Sandia design involving implosion onto extremely low-density foam cylinders as a means of enhancing stagnation uniformity.<sup>4</sup> Additional progress made in producing uniform z-pinch implosions includes adding axial magnetic field,<sup>5</sup> increasing the number of wires in array implosions,<sup>6</sup> and improved nozzle design for gas-puff experiments.<sup>7</sup>

In our work, we focus on a z-pinch driven neonlike krypton x-ray laser design, for which we: 1) investigate the role initial mass loading plays in affecting plasma uniformity and gain, and 2) show there are advantages with respect to temporal and spatial uniformity to diluting a pure krypton plasma with a low atomic number material such as helium. The purpose of the helium is to reduce the specific (per unit mass) radiative cooling rate of the

plasma. If a localized region cools faster than energy is supplied to the region, its density increases in order to maintain pressure equilibrium with the surrounding plasma. Because of the non-linear nature of radiative cooling, which varies as the square of the number density for optically thin bremsstrahlung and recombination radiation, the increase in density causes the local plasma to cool faster. As the local plasma progressively radiates and compresses, the process feeds upon itself until either opacity or temperature effects limit the radiative cooling. As a result, the global plasma can have steep gradients in temperature and density, and it can become increasingly unstable.<sup>8</sup> In addition, a strongly radiating plasma can lose its thermal energy rapidly, thus, limiting the time over which gain can be achieved. By adding a poor radiator such as helium, which reduces the radiative cooling rate, the deleterious effects of the above processes can be limited.

## II. MODEL DESCRIPTION

The calculation proceeds in two stages. First, we follow the evolution of the helium and krypton mixture as it implodes on axis. This is accomplished using a 1D radiation hydrodynamic model which solves continuity, momentum, and energy equations in a 40 zone Lagrangian reference frame with cylindrical geometry. The fluid equations describing the plasma dynamics are:

Mass continuity,

$$\frac{dV}{dt} = \frac{V}{r} \frac{\delta}{\delta r} (ru) \quad (1)$$

Momentum,

$$\frac{du}{dt} = -v \frac{\delta P}{\delta r} - \frac{V}{r} \frac{\delta}{\delta r}(rQ) \quad (2)$$

and two equations describing the change in

electron internal energy,

$$\frac{dE_e}{dt} = -P_e \frac{dV}{dt} + \frac{V}{r} \frac{\delta}{\delta r}(rK_e \frac{\delta T_e}{\delta r}) + R + 2\omega_c(T_i - T_e) \quad (3)$$

and ion internal energy,

$$\frac{dE_i}{dt} = -P_i \frac{dV}{dt} + \frac{V}{r} \frac{\delta}{\delta r}(rK_i \frac{\delta T_i}{\delta r}) - VQ \frac{\delta u}{\delta r} - 2\omega_c(T_i - T_e) \quad (4)$$

In Eqs. (1) - (4),  $V$  is the specific volume,  $u$  is the radial fluid velocity,  $P$  is the total particle pressure,  $P_e$  and  $P_i$  are electron and ion pressures,  $E_e$  and  $E_i$  are electron and ion internal energies,  $K_e$  and  $K_i$  are electron and ion thermal conductivities,  $T_e$  and  $T_i$  are the electron and ion temperatures,  $Q$  is the von Neumann artificial viscosity,<sup>9</sup>  $R$  is the specific radiative loss or gain, and  $\omega_c$  is the electron-ion collision rate. The transport coefficients  $K_e$ ,  $K_i$ , and  $\omega_c$  are given by Braginskii.<sup>10</sup>

These equations are put in closed form by using the ideal gas equation of state for the electrons and ions:

$$P_e = \frac{2}{3} (E_e - E_z)/V \quad (5)$$

$$P_i = \frac{2}{3} E_i/V \quad (6)$$

where  $E_z$  is the potential energy due to ionization and excitation of the atoms.

Several quantities in the above equations are obtained by solving ionization and radiation dynamics equations for the krypton component of the plasma. These are krypton's contribution to  $R$ , the radiative loss rate,  $E_z$

the ionization and excitation energy density, and  $Z$  the effective charge of the plasma. The ionization and radiation dynamics is treated self-consistently using the collisional-radiative-equilibrium (CRE) radiation and atomic physics models developed at NRL.<sup>11-17</sup> The helium component of the plasma is assumed completely ionized, and therefore radiates only bremsstrahlung. This is an excellent approximation because the plasma temperatures of interest exceed 50 eV, virtually assuring that the helium will be completely ionized.

Radiation is coupled to the plasma through emission and absorption processes. Photoionization and photoexcitation directly affect the populations while inner-shell absorption and radiative cooling produce indirect changes by altering the temperature. In order to self-consistently include these processes, the radiation field must be transported. This is accomplished by a probabalistic transport scheme in which angle and frequency averaged escape probabilities are calculated for each line and continuum emission process.<sup>18,19</sup> Coupling of photons from cell to cell is described by differencing the escape probabilities across the cell boundaries. The probabalistic transport scheme is only applied to the krypton component. The helium contributes free electrons, ionization energy, thermal energy, and optically thin bremsstrahlung radiation. There is no coupling of the radiation between the helium and krypton ions other than indirect thermal effects brought on by the sum of the radiative cooling emanating from both helium and krypton. A more complete description of the ionization dynamics and radiation transport models employed in this study are given in Refs. 20 and 21.

Once the hydrodynamic profiles and the time evolution of the ground states of neonlike and fluorinelike krypton are obtained from this first stage of the calculation the gain is calculated using a detailed multilevel

model similar to the one described in Ref. 22. There are two significant alterations made to this model: 1) it is adapted to neonlike krypton, and 2) the original Sobolev escape probability<sup>23</sup> is replaced with the more accurate angle-averaged Sobolev escape probability for axially symmetric plasmas.<sup>24</sup> This escape probability is essential for gain calculations because it allows for photon escape in frequency space due to large velocity gradients and curvature effects present in the plasma. The reduced opacity can decrease trapping of the lower level  $2p^5 3s - 2p^6$  transitions significantly compared to the case of no bulk Doppler effects in the radiation transport. The gain model assumes a Voigt line profile.

We are currently investigating Stark broadening effects, but we did not include them in the gain model. Stark broadening may become important for neonlike krypton transitions, especially for the He/Kr mixture plasmas containing many additional free electrons surrounding each krypton ion.

### III. RESULTS

#### A. Initial Conditions

The plasma is assumed to have initially evolved in a z-pinch implosion to a state of spatially constant density within a cylinder of radius 0.5 cm, uniform temperature of 100 eV, and inward radial velocity of  $4 \times 10^7$  cm/sec. The succeeding evolution of the plasma is calculated without taking into account the presence of an azimuthal magnetic field driver, which is normally present in gas-puff experiments. Neglecting the magnetic field driver will substantially change the dynamics of an implosion, especially the late time behavior because of the  $r^{-1}$  variation of the magnetic field at the outer radial boundary of the pinch. A simulation of a magnetically

driven implosion will produce a nearly uniform radial velocity, as assumed in our study. However, unlike our uniform density and temperature assumption, density and temperature gradients will be generated by the presence of the magnetic field. This is especially true for regions close to the outer edge of the plasma, where significant Ohmic heating is present. We intend to include some of the magnetic field effects in future work. For now, we assume that the qualitative results of this idealized study will be a valid guide to the more complete theoretical treatment.

We investigate a variety of gas puffs with different mass loadings as well as different concentrations of helium and krypton. The mass loading is given in terms of micrograms per unit axial length ( $\mu\text{g}/\text{cm}$ ) of the pinch. Since the radial velocity is, unless otherwise stated,  $4 \times 10^7$  cm/sec, all of the different mass loads will have the same kinetic-energy-per-unit-mass. The total mass as well as its He/Kr ratio will affect the way in which the plasma radiates and ultimately thermalizes its kinetic energy during the on-axis stagnation.

#### B. Comparison of Density and Temperature Profiles

First, we examine temperature and density profiles for simulations involving different mass loads composed entirely of krypton. The krypton ion density profiles shown in Fig. 1a and the electron temperature profiles shown in Fig. 1b for the  $30 \mu\text{g}/\text{cm}$  mass loading of krypton are reasonably flat and temporally uniform near the axis of the pinch. For times greater than 3.88 ns, the krypton ion density varies by less than an order of magnitude over a radial expanse of 0.06 cm and the electron temperature varies by less than a factor of 2. By comparing the  $30 \mu\text{g}/\text{cm}$  profiles to those obtained from increasing the mass load to  $100 \mu\text{g}/\text{cm}$  as shown in Fig. 2a and Fig. 2b,

we begin to expose the effects of the non-linear behavior of radiation. In general, the plasma becomes a more efficient radiator as its mass is increased. This results in density profiles that are sharply peaked on axis and near axis temperature profiles that decrease rapidly in time as the dense plasma loses thermal energy to radiation. These changes in density and temperature profiles are dramatically illustrated in Figs. 3a and 3b in which results for a 200  $\mu\text{g}/\text{cm}$  load are displayed.

By changing the ion composition of the 200  $\mu\text{g}/\text{cm}$  plasma to a mixture of 98 percent helium by number (140  $\mu\text{g}/\text{cm}$ ) and 2 percent krypton (60  $\mu\text{g}/\text{cm}$ ), Figures 4a and 4b, we again obtain reasonably flat temperature and krypton ion density profiles. The flatter profiles are obtained because helium is an inherently less effective radiator than krypton. As mentioned in the introduction, large temperature and density gradients are strongly correlated with radiative cooling of the plasma. This is clearly demonstrated in Fig. 5 where the accumulated radiative emission per unit mass is plotted as a function of time for the various plasmas. Although the profiles of the 30  $\mu\text{g}/\text{cm}$  plasma, 60  $\mu\text{g}/\text{cm}$  plasma (no density and temperature profiles are displayed for this case), and the 200  $\mu\text{g}/\text{cm}$  plasma consisting of 98 percent helium are considerably more uniform than those of the other plasmas, which is an important objective, achievement of gain while maintaining plasma uniformity remains to be demonstrated theoretically as well as experimentally.

### C. Gain Production

The gains produced during the implosion of a 30  $\mu\text{g}/\text{cm}$ , 60  $\mu\text{g}/\text{cm}$ , 100  $\mu\text{g}/\text{cm}$ , and 200  $\mu\text{g}/\text{cm}$  plasma consisting of 100 percent krypton as well as a 200  $\mu\text{g}/\text{cm}$  plasma composed of 98 percent helium are now discussed. The

initial conditions are identical to those described earlier, i.e. uniform density distributed within a cylinder of 0.5 cm radius, uniform temperature distribution of 100 eV, and a uniform radial velocity of  $4 \times 10^7$  cm/sec. Results for small signal gain produced in the 3p - 3s (J=0-1) transition at  $172 \text{ \AA}$  and the (J=2-1) transition at  $186 \text{ \AA}$ , see Fig. 6, are described because they generally have the largest magnitude, span the most space, and have the longest duration of the multitude of lasing transitions.

Fig. 7 displays contour plots in which the area inside each curve represents the temporal and spatial region over which gain was achieved above a threshold value of  $3 \text{ cm}^{-1}$  for the 0-1 transition for the low mass 30  $\mu\text{g/cm}$  and 60  $\mu\text{g/cm}$  simulations. We find that the 30  $\mu\text{g/cm}$  load shows gain regions with spatial extent in excess of 0.05 cm that endure for as long as 5 ns. The results for 60  $\mu\text{g/cm}$  also span a temporal and spatial region of nearly the same area as the 30  $\mu\text{g/cm}$  results. However, as the mass is further increased the gain region becomes progressively smaller. This behavior, as illustrated in Fig. 8 for the 100  $\mu\text{g/cm}$  and 200  $\mu\text{g/cm}$  loads, is a consequence of the spatial and temporal non-uniformity of the more massive plasmas. However the magnitude of the gain tends to increase for the larger masses. There were transient regions of the 200  $\mu\text{g/cm}$  plasma that exhibited gains larger than  $10 \text{ cm}^{-1}$ , which is not surprising since the magnitude of gain increases linearly with ion number density until affected by collisions and/or opacity. The 200  $\mu\text{g/cm}$  load that consists of 98 percent helium ions did not attain gain greater than  $2 \text{ cm}^{-1}$  in the 0-1 transition.

Representative results for gain greater than  $2 \text{ cm}^{-1}$  produced in the 2-1 transition for the 30  $\mu\text{g/cm}$ , and 200  $\mu\text{g/cm}$  krypton loads are shown in Fig. 9. The 200  $\mu\text{g/cm}$  mixture load did not exhibit any gain exceeding  $1 \text{ cm}^{-1}$ . For purposes of later discussion and to illustrate the role of opacity,

optically thin gain results are displayed in Fig. 10 for the 30  $\mu\text{g}/\text{cm}$  and 200  $\mu\text{g}/\text{cm}$  simulations.

So far we have demonstrated that given the initial conditions, only the low mass 30  $\mu\text{g}/\text{cm}$  and 60  $\mu\text{g}/\text{cm}$  plasmas fulfill both requirements of maintaining uniform plasma conditions as well as achieving significant gain over broad spatial and temporal regions. For implosion velocities of  $4 \times 10^7$  cm/sec the more massive, pure krypton loads radiatively dissipate the thermalized kinetic energy too rapidly to maintain plasma uniformity. The 200  $\mu\text{g}/\text{cm}$  plasma composed of helium and krypton maintains uniformity but does not achieve the necessary gain. The reason the mixture plasma has difficulty producing gain is because the helium provides an additional 98 free electrons that affect each krypton ion. These free electrons increase the collisionality of the plasma, broaden the lasing lines, and increase the overall number density of particles, thus, allowing the plasma to seek pressure equilibration at lower temperatures.

The effects of enhanced collisionality are illustrated in optically thin gain contours as a function of electron temperature and krypton ion density for different mixtures of plasma. Specifically we have calculated the optically thin gain curves for the 0-1 transition for 100 %, 1 %, 2 %, and 3 % plasma mixtures of krypton with helium. The results for gains in excess of  $2 \text{ cm}^{-1}$  for the 0-1 transition are displayed in Fig. 11. The region that lies to the right of each curve is where the gain is larger than  $2 \text{ cm}^{-1}$ . It is clear that in order to achieve significant gain at a fixed krypton ion density, one needs to go to progressively higher temperatures as the krypton concentration is reduced. Based on these optically thin results it appears that one could use a 2 percent krypton mixture and still be able to achieve significant gain under density and temperature conditions similar to the 100 percent krypton case. In the 1 percent case, the collisionality is

increased to the extent that each krypton ion sees an additional 198 free electrons. The effect of this enhancement is reflected by a loss of gain at lower temperatures. As expected, the 3 percent krypton results are closest to the 100 percent krypton case. Unfortunately, a large mass plasma containing 3 percent krypton implies that almost 40 percent of the mass is krypton. Such a plasma will radiatively cool rapidly and consequently will not have as uniform behavior during stagnation as a plasma with a lower percentage of krypton.

Based upon the density and temperature plots for the 200  $\mu\text{g}/\text{cm}$  mixture plasma, Figures 4a and 4b, and the above contour plots for gain, Fig. 11, it appears that more optimal gain conditions could be achieved if the plasma reached higher temperatures and densities than those obtained in the simulation. One way to accomplish this is to increase the implosion velocity. Figures 12a and 12b show the density and temperature profiles of a 200  $\mu\text{g}/\text{cm}$ , 2 percent krypton, 98 percent helium mixture that is imploded under nearly the same initial conditions as the original simulation, with the one exception that the implosion velocity has been increased to  $5 \times 10^7$  cm/sec. The larger implosion velocity supplies 56 percent more kinetic energy available to be thermalized at stagnation than the  $4 \times 10^7$  cm/sec case. This larger energy is reflected in slightly higher temperature and density profiles. The near axis profiles at the higher implosion velocity are similar to the lower velocity profiles in that they are reasonably flat. Additionally, the density and temperature profiles for a 200  $\mu\text{g}/\text{cm}$  pure krypton plasma having an initial implosion velocity of  $5 \times 10^7$  cm/sec are displayed in Figures 13a and 13b. As was true for the lower velocity implosion, there are steep near axis temporal and spatial gradients.

Contour plots for the gain achieved in excess of  $1 \text{ cm}^{-1}$  in the 0-1 transition for the 200  $\mu\text{g}/\text{cm}$  simulations at  $5 \times 10^7$  cm/sec implosion

velocity as well as the mixture at  $4 \times 10^7$  cm/sec are shown in Fig. 14. The gains in excess of  $2 \text{ cm}^{-1}$  are displayed in Fig. 15. The gain for the mixture plasma at  $5 \times 10^7$  cm/sec is not as large as hoped for in the sense that a pure krypton plasma having the same temperature and krypton ion density profiles as exhibited in Figs. 12a and 12b would achieve significantly more gain, see Figs. 1a, 1b, and 7. Thus, it appears that the enhanced collisionality and line broadening associated with the additional electrons of the He/Kr mixture plasmas significantly reduces achievable gain. Even so, these figures reveal that there is a definite enhancement of gain in the 0-1 transition as the implosion velocity is increased from  $4 \times 10^7$  cm/sec to  $5 \times 10^7$  cm/sec for the  $200 \text{ } \mu\text{g/cm}$  plasma mixture of helium and krypton. Therefore, at least for massive plasma loads  $\sim 200 \text{ } \mu\text{g/cm}$  or greater, the results of this work show that there are some advantages to using a mixture of helium and krypton plasma to obtain significant gain coincident with uniform plasma profiles.

#### IV. DISCUSSION and SUMMARY

It is believed that the successful demonstration of inversion and gain in z-pinch imploded gain media depends in large part on the control of inhomogeneities in temperature and density that occur as the plasma implodes on axis. These inhomogeneities can destroy lasing by shortening the gain length and refracting the beam. It is believed that the large density and temperature gradients are partially due to nonuniform initial conditions, magnetic Raleigh-Taylor instabilities, and hydrodynamic instabilities. As was noted by Hussey,<sup>25</sup> "1D calculations are optimistic, and, even with expected improvements, uncertainty in thermalization time associated with implosion nonuniformities must be accounted for in x-ray laser designs." With the

above statement as an underlying tenet, the focus of this work has been to investigate an x-ray laser design in which the gradients that exist in a purely theoretical 1D implosion calculation, without instabilities, are minimized. It is presumed that an experiment designed with these features in mind would enhance the width and lifetime of the lasing channels to the extent that even an unstable plasma would be better able to overcome the difficulties associated with achieving significant gain.

The results of our theoretical work show that there are tradeoffs between obtaining plasma uniformity and large gain coefficients. For example, there are expansive regions in time and space over which the low mass 30  $\mu\text{g}/\text{cm}$  and 60  $\mu\text{g}/\text{cm}$  pure krypton plasmas exhibit gain coefficients of the order of  $3 \text{ cm}^{-1}$  for the  $3p - 3s$  ( $J=0-1$ ) transition at  $172 \text{ \AA}$ . These plasmas also maintain excellent spatial and temporal plasma uniformity. Conversely, there are regions of the 200  $\mu\text{g}/\text{cm}$ , 100 percent krypton plasma that achieved much larger gain coefficients, some in excess of  $10 \text{ cm}^{-1}$ . However, there is a considerable price to pay for this large gain in terms of loss of plasma uniformity. The underlying reason for this difference in behavior between high mass and low mass loads is the non-linear scaling of radiation with local density. In moderate density plasmas the local radiative loss is a result of binary collisions and is therefore proportional to the square of the local density. As a plasma stagnates on axis it experiences an increase in local near axis density, and if the density enhancement of radiative cooling is large enough to compete with thermal conduction, PdV work, and other local heating mechanisms the plasma cools and the local density increases further to attempt to maintain pressure equilibrium with the rest of the plasma. This collapse process feeds upon itself until either temperature or opacity effects reduce the radiative loss

from the dense region of plasma. This behavior is calculated to be prominent in the high mass krypton plasmas.

The low mass plasmas consisting of pure krypton produced the best results in terms of significant gain coinciding with large spatial and temporal uniformity. Based on a Katzenstein scaling,<sup>26</sup> it would require a pulse power machine capable of producing peak currents in the 1 MA to 2 MA range in order to theoretically accelerate 30  $\mu\text{g}/\text{cm}$  and 60  $\mu\text{g}/\text{cm}$  loads to an implosion velocity of  $4 \times 10^7$  cm/sec, which is a near minimal requirement for insuring ionization to the neonlike krypton state. The mixing of helium with krypton in order to produce a more temporally and spatially uniform stagnation by reducing the specific radiative cooling of the plasma, is a useful idea if one is constrained to implode massive loads. In our example of a 200  $\mu\text{g}/\text{cm}$  plasma in which 2 percent of the ions are krypton, we found good plasma uniformity and respectable gain,  $\sim 2 \text{ cm}^{-1}$ . Experiments operating under these conditions would require a machine capable of producing peak currents of 3 MA in order to impart the necessary implosion velocities of  $5 \times 10^7$  cm/sec needed to strip the krypton to the neonlike state. Note, on the one hand there was no attempt made to optimize gain conditions as a function of mass loading and implosion velocity in this work. On the other hand, the presented results are not restricted to implosion velocities of 4 and  $5 \times 10^7$  cm/sec. In general, the more massive pure krypton plasmas still exhibited non-uniform plasma behavior at much higher implosion velocities.

Experiments have shown that a separation between helium and krypton ions arises during the implosion phase such that helium arrives first on axis.<sup>27</sup> These experiments are supported by theory which qualitatively explains this phenomenon by assuming that in the early stages of the implosion the ions are cold and collisionless and the electrons are hot and collisional.<sup>28</sup> As interior electrons are pushed inward by the external

magnetic piston, a small charge separation is produced. The induced electric field drags along the ions to assure quasineutrality. The different species are dragged along at different speeds, with the heavier ions moving slower. These experiments were for 4 - 5  $\mu\text{g}/\text{cm}$  plasma mixtures of 98.5 percent helium and 1.5 percent krypton by ion number density. It is not clear that the same collisionless ion behavior would be exhibited by the more massive loads  $\sim 200 \mu\text{g}/\text{cm}$  discussed in this work. If it is, it may only affect a small percentage of the mass located near the inner surface of the plasma column. If collisionless behavior does cause a separation of ion species throughout the plasma, then one needs to use an innovative target design to insure proper mixing of helium and krypton.

There is some evidence that gain in the 0-1 transition is theoretically overpredicted. For example, in the Livermore selenium experiments,<sup>29,30</sup> gain in the 0-1 transition was a factor of three lower than the calculated results. In these experiments, the observed gain in the 3p-3s (J=2-1) transitions at 206 and 209  $\text{\AA}$  were considerably larger than the 0-1 gain. If this is the case, and one is constrained to optimize gain in the 2-1 transitions, then our results are still qualitatively the same as mentioned above. The major quantitative difference is that the spatial and temporal extent of the gain region for the 2-1 transition is much smaller than the 0-1 region, as is illustrated by comparing Fig. 7 with Fig. 9. However, there is experimental evidence to suggest that the plasmas are not as opaque as predicted by theory.<sup>31</sup> If this is true, then the optically thin 2-1 gains shown in Fig. 10 are very encouraging.

ACKNOWLEDGMENTS - We would like to thank Dr. P. C. Kepple for providing us with the krypton rate table. This work was supported by the Strategic Defense Initiative Office of Innovative Science and Technology.

## References

1. M. Krishnan, R. Nash, P. Le Pell, and R. Rodenburg, "Krypton on Krypton Z-Pinch X-Ray Laser Experiment," Physics International Rept. PIT-87-02 (1987).
2. J. Davis, R. Clark, J. P. Apruzese, and P. C. Kepple, IEEE Trans. on Plasma Sci. 16, 482 (1988).
3. J. L. Porter et al., Paper 3D1-2, IEEE Int. Conf. Plasma Sci., Oakland, California USA (1990).
4. R. B. Spielman, M. K. Matzen, M. A. Palmer, P. B. Rand, T. W. Hussey, and D. H. McDaniel, Appl. Phys. Lett. 47, 229 (1985).
5. F. S. Felber, F. J. Wessel, N. C. Wild, H. U. Rahman, A. Fisher, C. M. Fowler, M. A. Liberman, and A. L. Velikovich, Lasers and Particle Beams 5, 699 (1987).
6. R. B. Spielman, private communication, Sandia National Laboratories.
7. T. W. Hussey, M. K. Matzen, and N. F. Roderick, J. Appl. Phys. 59, 2677 (1986).
8. R. G. Evans, Plasma Physics and Controlled Fusion 27, 751 (1985).
9. J. VonNeumann and R. D. Richtmyer, J. Appl. Phys. 21, 232 (1950).

10. S. I. Braginskii, in *Reviews of Plasma Physics*, edited by M. A. Leontovich (Consultants Bureau, New York, 1965), Vol. 1.
11. D. Duston and J. Davis, *Phys. Rev. A* 23, 2602 (1981).
12. D. R. Bates, A. E. Kingston, and R. W. P. McWhirter, *Proc. R. Soc. London Ser. A* 267, 297 (1962).
13. See, for example, J. Davis, *J. Quant. Spectrosc. Radiat. Trans.* 14, 549 (1974); A. Burgess, H. P. Summers, D. M. Cochrane, and R. W. P. McWhirter, *Mon. Not. R. Astron. Soc.* 179, 275 (1977).
14. V. L. Jacobs, J. Davis, P. C. Kepple, and M. Blaha, *Astrophys. J.* 211, 605 (1977).
15. W. J. Karzas and B. Latter, *Astrophys. J. Suppl. Ser.* 6, 167 (1961).
16. V. L. Jacobs, J. Davis, *Phys. Rev. A* 18, 697 (1978).
17. J. Davis, P. C. Kepple, and M. Blaha, *J. Quant. Spectrosc. Radiat. Transfer* 16, 1043 (1977).
18. J. P. Apruzese, J. Davis, D. Duston, and R. W. Clark, *Phys. Rev. A* 29, 246 (1984).
19. J. P. Apruzese, J. Davis, D. Duston, and K. G. Whitney, *J. Quant. Spectrosc. Radiat. Transfer* 23, 479 (1980).

20. D. Duston, R. W. Clark, J. Davis, and J. P. Apruzese, Phys. Rev. A 27, 1441 (1983).
21. R. W. Clark, J. Davis, and F. L. Cochran, Phys. Fluids 29, 1971 (1986).
22. J. P. Apruzese, P. C. Kepple, J. Davis, and J. Pender, IEEE Trans. Plasma Sci. 16, 529 (1988).
23. V. V. Sobolev, Sov. Astron. 1, 678 (1957).
24. A. I. Shestakov and D. C. Eder, J. Quant. Spectrosc. Radiat. Transfer 42, 483 (1989).
25. T. W. Hussey, M. K. Matzen, and N. F. Roderick, J. Appl. Phys. 59, 2677 (1986).
26. J. Katzenstein, J. Appl. Phys. 52, 676 (1981).
27. J. Bailey, A. Fisher, and N. Rostoker, J. Appl. Phys. 60, 1939 (1986).
28. G. Barak and N. Rostoker, Appl. Phys. Lett. 41, 918 (1982).
29. M. D. Rosen et al., Phys. Rev. Lett. 54, 106 (1985).
30. D. L. Matthews et al., Phys. Rev. Lett. 54, 110 (1985).
31. D. C. Eder, Phys. Fluids B 12, 2462 (1989).

## Figure Captions

FIG. 1a The krypton ion density as a function of time and radial position during the stagnation phase of the 30  $\mu\text{g}/\text{cm}$ , 100 percent krypton implosion. The initial implosion velocity is  $4 \times 10^7$  cm/sec.

FIG. 1b The electron temperature as a function of time and radial position during the stagnation phase of the 30  $\mu\text{g}/\text{cm}$ , 100 percent krypton implosion. The initial implosion velocity is  $4 \times 10^7$  cm/sec.

FIG. 2a The krypton ion density as a function of time and radial position during the stagnation phase of the 100  $\mu\text{g}/\text{cm}$ , 100 percent krypton implosion. The initial implosion velocity is  $4 \times 10^7$  cm/sec.

FIG. 2b The electron temperature as a function of time and radial position during the stagnation phase of the 100  $\mu\text{g}/\text{cm}$ , 100 percent krypton implosion. The initial implosion velocity is  $4 \times 10^7$  cm/sec.

FIG. 3a The krypton ion density as a function of time and radial position during the stagnation phase of the 200  $\mu\text{g}/\text{cm}$ , 100 percent krypton implosion. The initial implosion velocity is  $4 \times 10^7$  cm/sec.

FIG. 3b The electron temperature as a function of time and radial position during the stagnation phase of the 200  $\mu\text{g}/\text{cm}$ , 100 percent krypton implosion. The initial implosion velocity is  $4 \times 10^7$  cm/sec.

FIG. 4a The krypton ion density as a function of time and radial position during the stagnation phase of the 200  $\mu\text{g}/\text{cm}$ , 98 percent helium, 2 percent

krypton implosion. The initial implosion velocity is  $4 \times 10^7$  cm/sec.

FIG. 4b The electron temperature as a function of time and radial position during the stagnation phase of the 30  $\mu\text{g}/\text{cm}$ , 98 percent helium, 2 percent krypton implosion. The initial implosion velocity is  $4 \times 10^7$  cm/sec.

FIG. 5 The radiated energy per unit mass as a function of time for the different mass loadings and He/Kr mixtures. All of the initial implosion velocities are  $4 \times 10^7$  cm/sec.

FIG. 6 Energy level diagram for neonlike krypton.

FIG. 7 Gain contours for the 30 and 60  $\mu\text{g}/\text{cm}$ , 100 percent Kr simulations. The gain is  $3 \text{ cm}^{-1}$  or larger interior to each curve for the 3p-3s ( $J=0-1$ ) transition at  $172 \text{ \AA}$ . The initial implosion velocities are  $4 \times 10^7$  cm/sec.

FIG. 8 Gain contours for the 100 and 200  $\mu\text{g}/\text{cm}$ , 100 percent Kr simulations. The gain is  $3 \text{ cm}^{-1}$  or larger interior to each curve for the 3p-3s ( $J=0-1$ ) transition at  $172 \text{ \AA}$ . The initial implosion velocities are  $4 \times 10^7$  cm/sec. The darkly shaded region is where gain is in excess of  $10 \text{ cm}^{-1}$ .

FIG. 9 Gain contours for the 30 and 200  $\mu\text{g}/\text{cm}$ , 100 percent Kr simulations. The gain is  $2 \text{ cm}^{-1}$  or larger interior to each curve for the 3p-3s ( $J=2-1$ ) transition at  $186 \text{ \AA}$ . The initial implosion velocities are  $4 \times 10^7$  cm/sec.

FIG. 10 Optically thin gain contours for the 30 and 200  $\mu\text{g}/\text{cm}$ , 100 percent Kr simulations. The 3p-3s ( $J=2-1$ )  $186 \text{ \AA}$  gain is  $2 \text{ cm}^{-1}$  or larger interior to each curve. The initial implosion velocities are  $4 \times 10^7$  cm/sec.

FIG. 11 Optically thin gain contours as a function of Kr ion density and electron temperature for different mixtures of He/Kr. The 3p-3s (J=0-1)  $172 \text{ \AA}$  gain is  $2 \text{ cm}^{-1}$  or larger to the right (interior) of each curve.

FIG. 12a The krypton ion density as a function of time and radial position during the stagnation phase of the  $200 \text{ \mu g/cm}$ , 98 percent He, 2 percent Kr implosion. The initial implosion velocity is  $5 \times 10^7 \text{ cm/sec}$ .

FIG. 12b The electron temperature as a function of time and radial position during the stagnation phase of the  $200 \text{ \mu g/cm}$ , 98 percent He, 2 percent Kr implosion. The initial implosion velocity is  $5 \times 10^7 \text{ cm/sec}$ .

FIG. 13a The krypton ion density as a function of time and radial position during the stagnation phase of the  $200 \text{ \mu g/cm}$ , 100 percent Kr implosion. The initial implosion velocity is  $5 \times 10^7 \text{ cm/sec}$ .

FIG. 13b The electron temperature as a function of time and radial position during the stagnation phase of the  $200 \text{ \mu g/cm}$ , 100 percent Kr implosion. The initial implosion velocity is  $5 \times 10^7 \text{ cm/sec}$ .

FIG. 14 Gain contours for different He/Kr  $200 \text{ \mu g/cm}$  simulations. The gain is  $1 \text{ cm}^{-1}$  or larger interior to each curve for the 3p-3s (J=0-1) transition at  $172 \text{ \AA}$ .

FIG. 15 Gain contours for different He/Kr  $200 \text{ \mu g/cm}$  simulations. The gain is  $2 \text{ cm}^{-1}$  or larger interior to each curve for the 3p-3s (J=0-1) transition at  $172 \text{ \AA}$ . The initial implosion velocities are  $5 \times 10^7 \text{ cm/sec}$ .

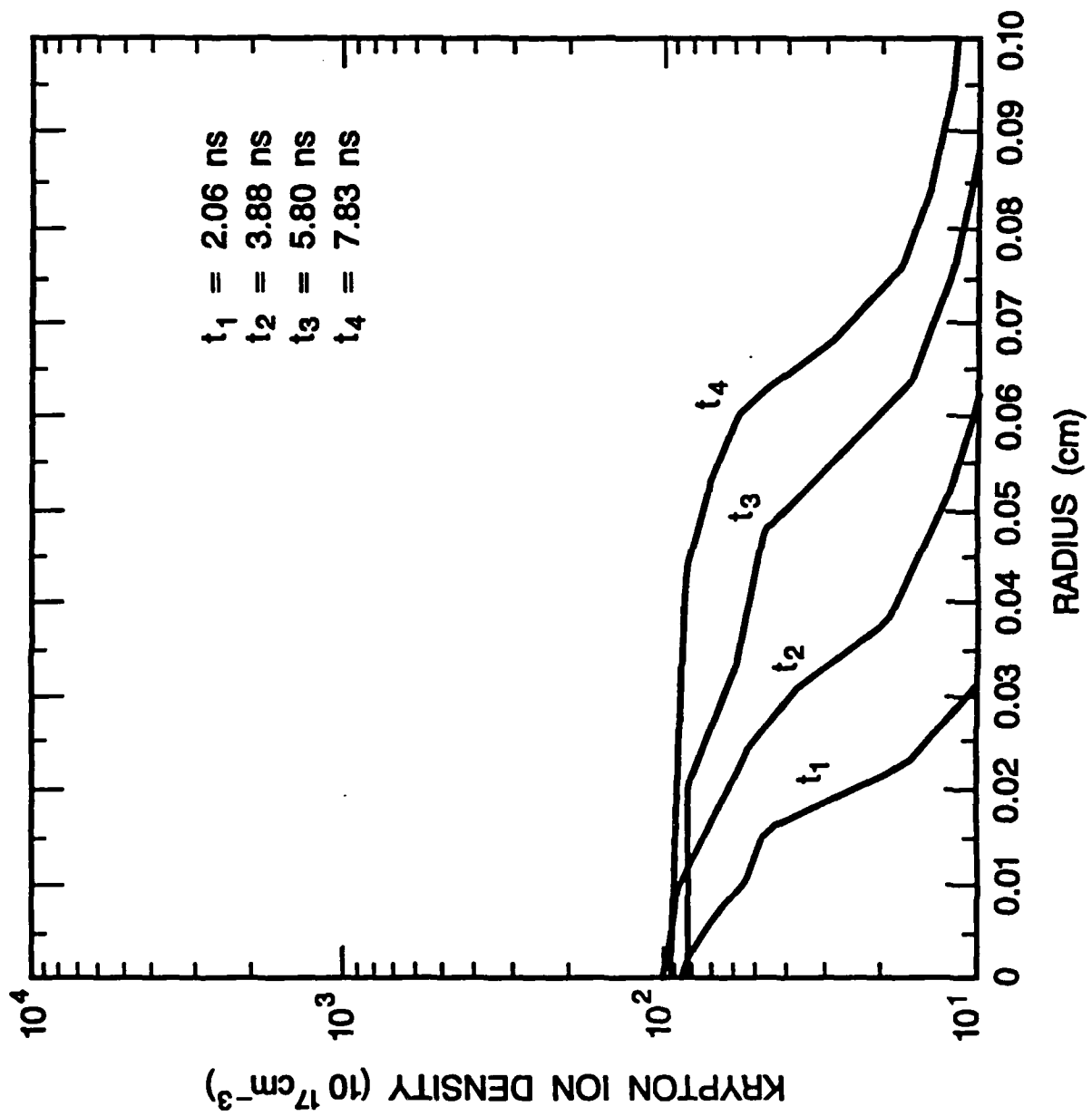


Fig. 1a

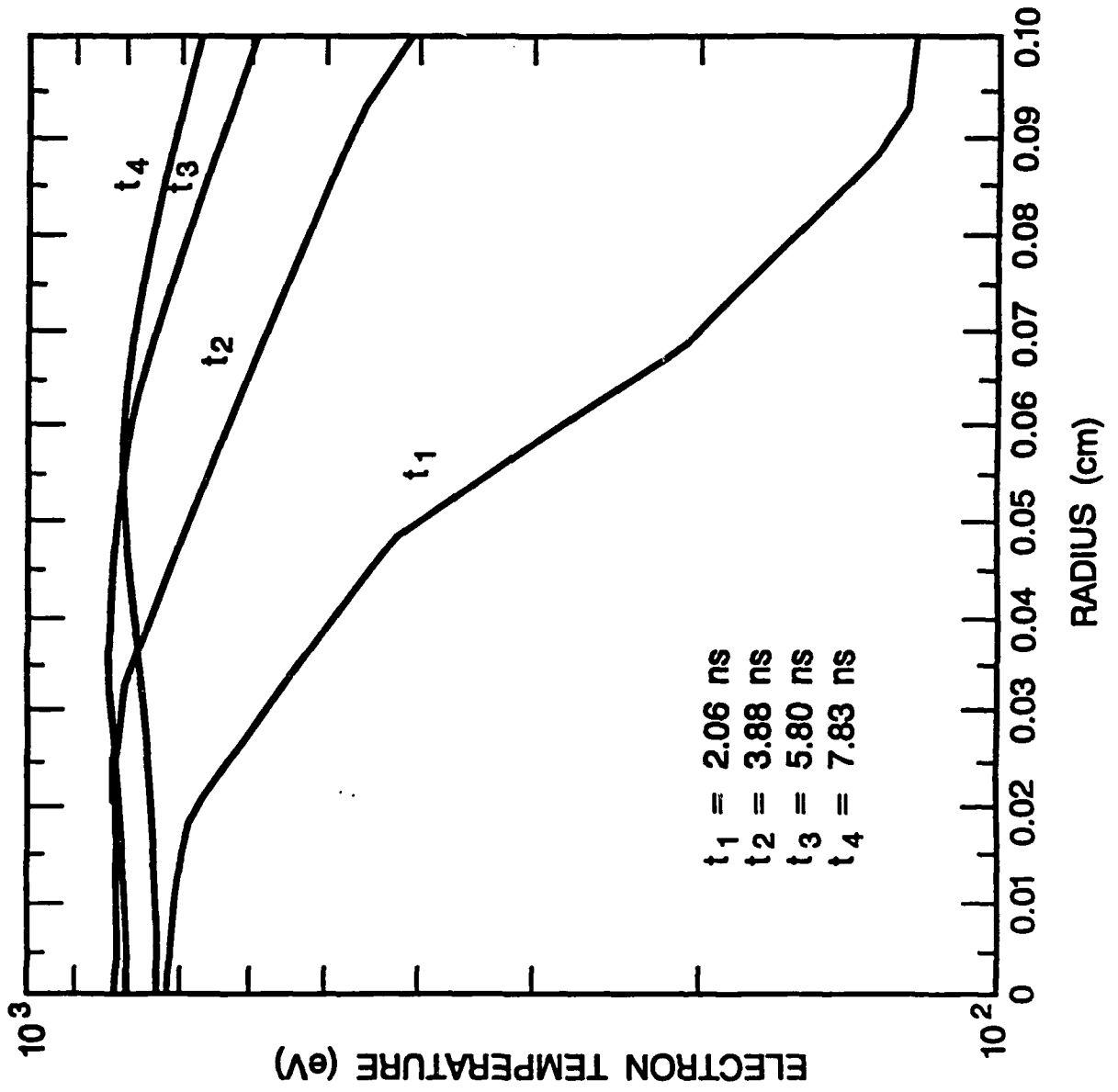


Fig. 1b

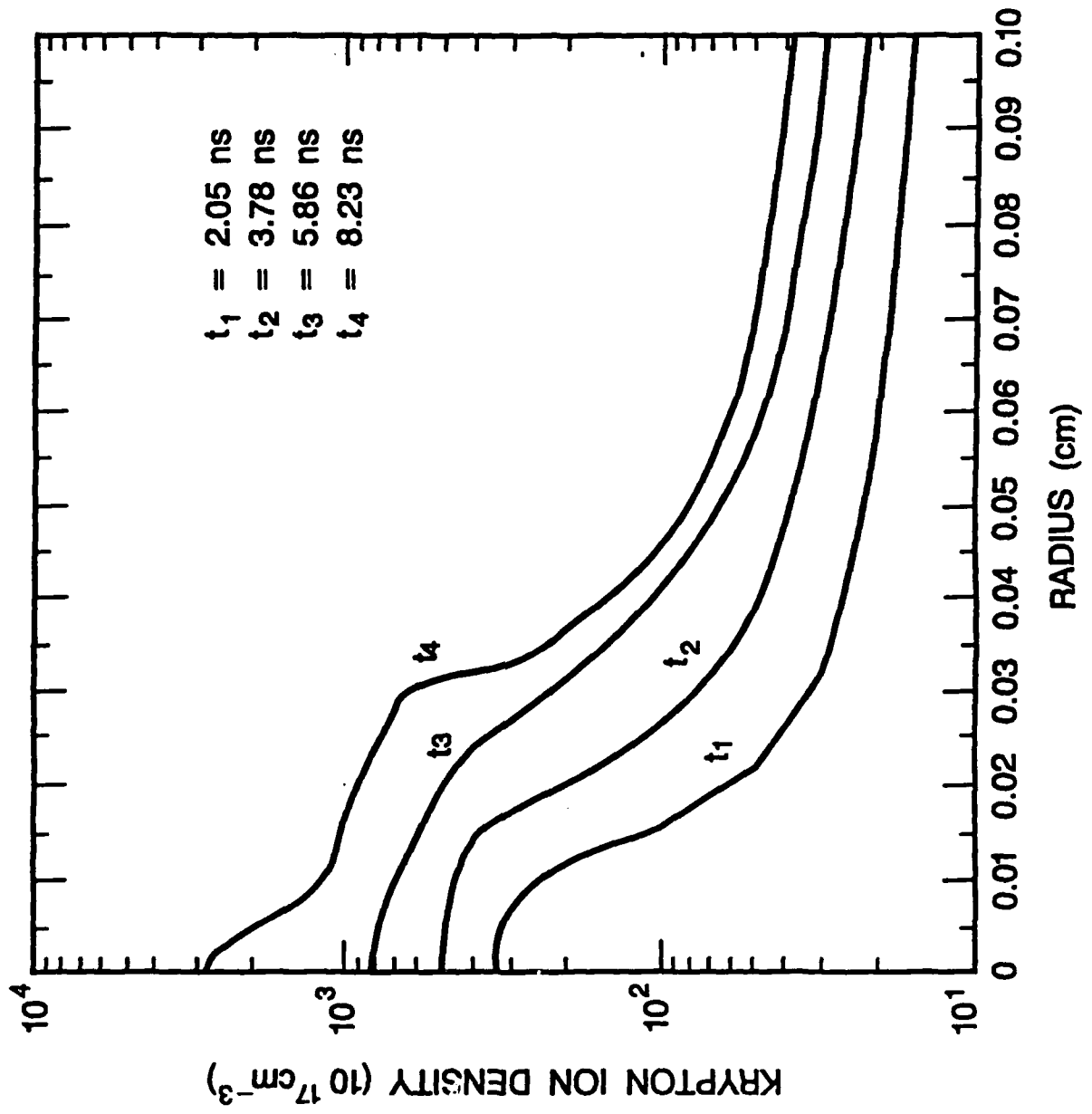


Fig. 2a

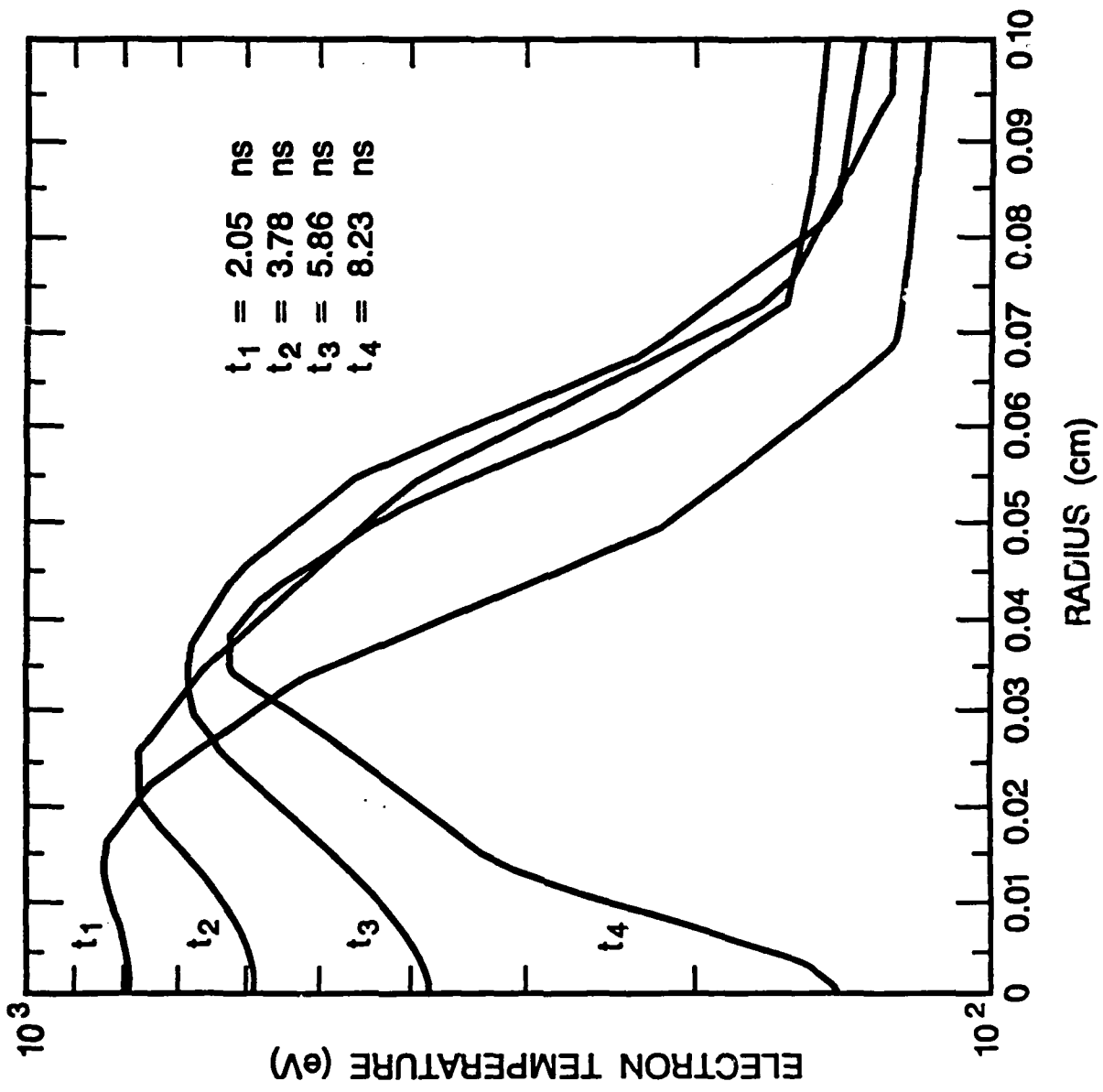


Fig. 2b

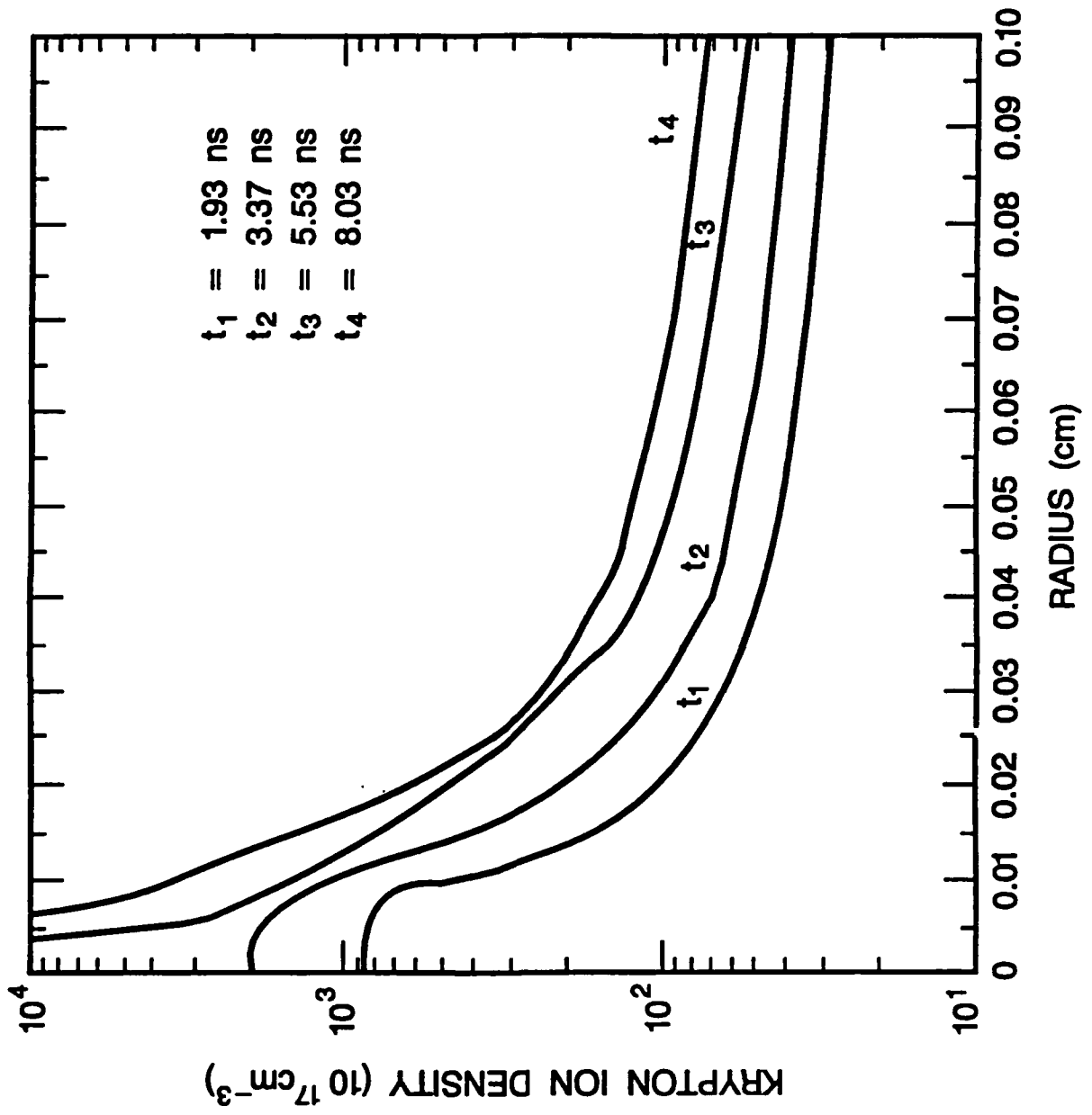


Fig. 3a

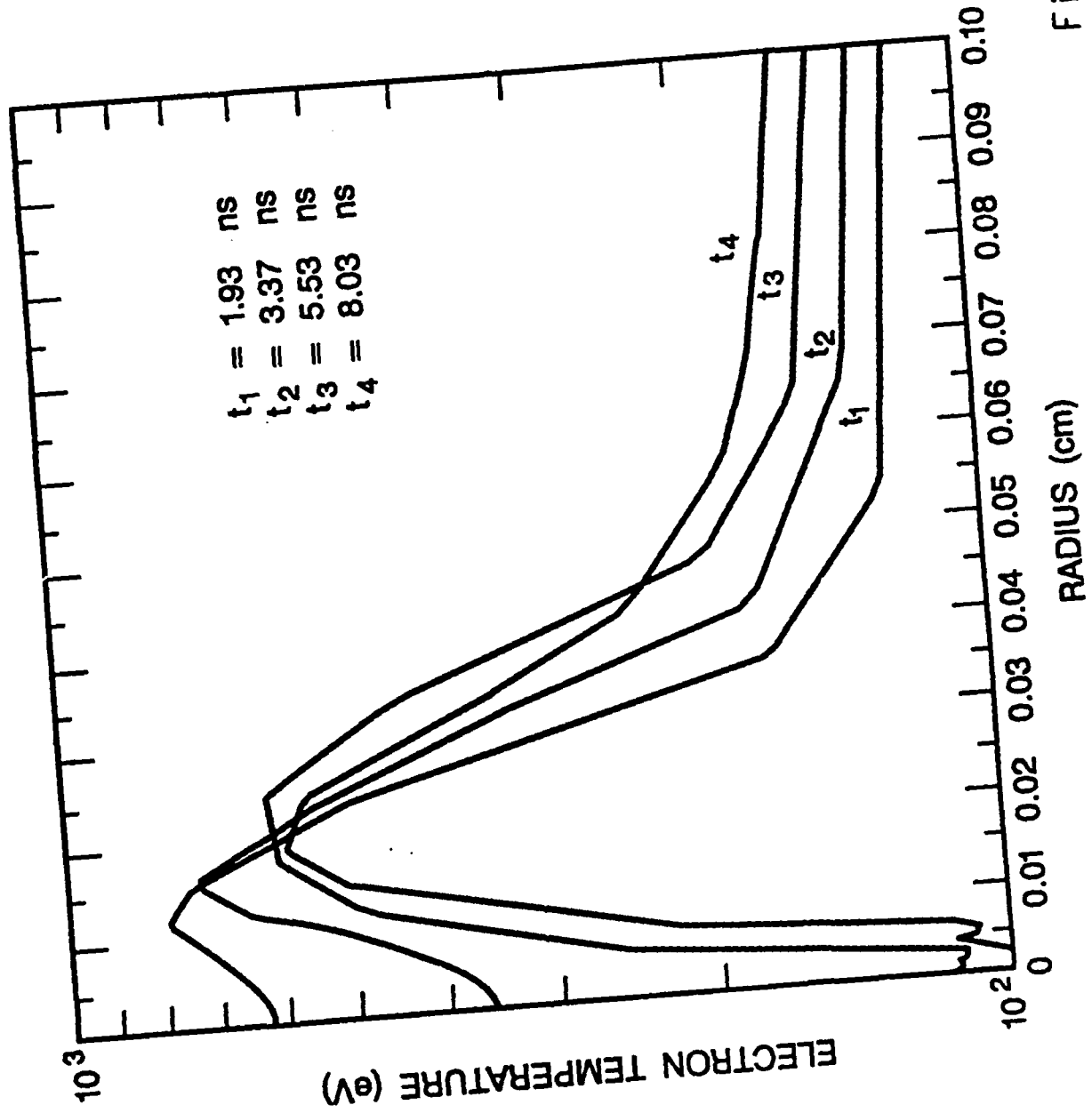


Fig. 3b

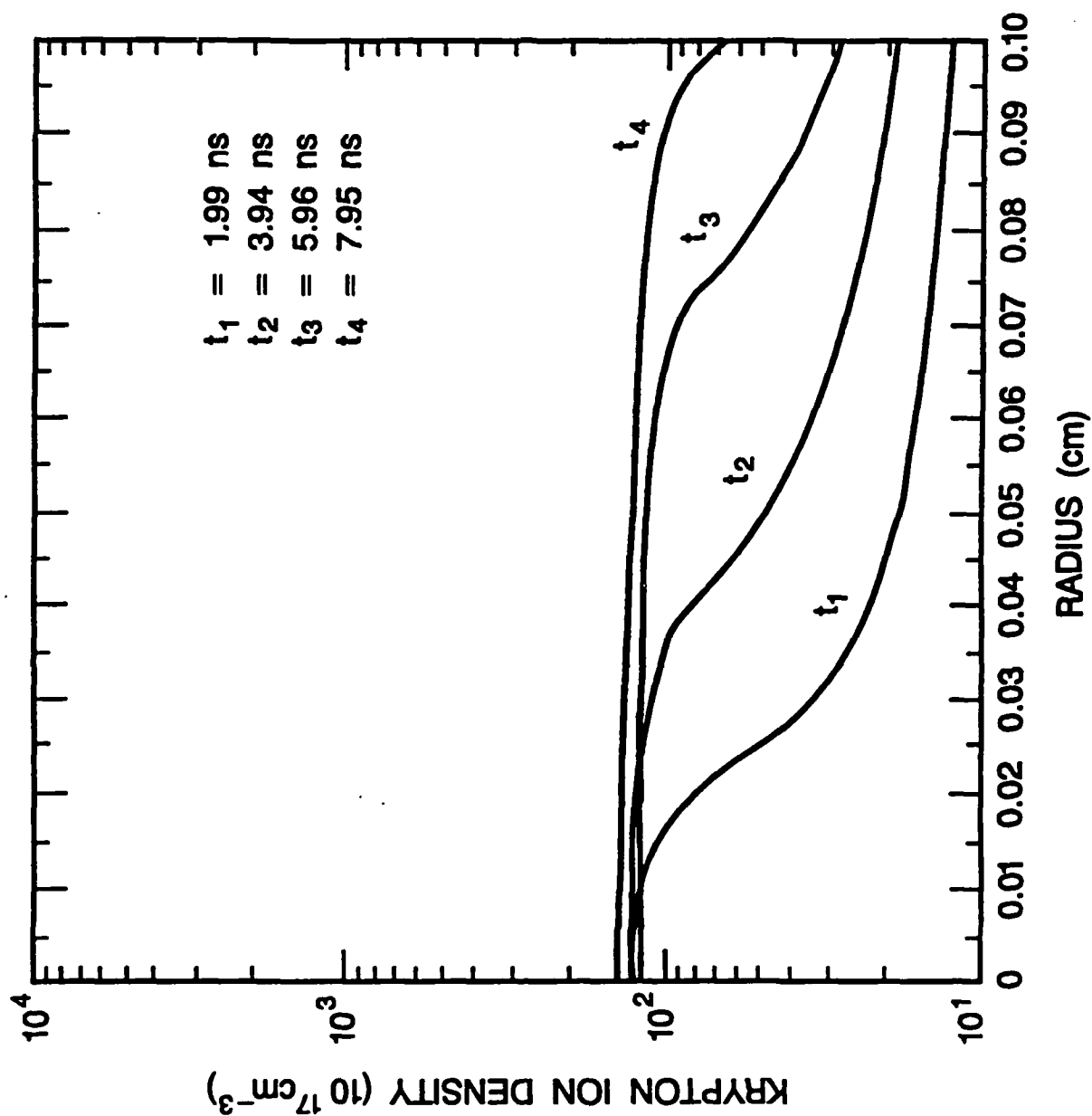


Fig. 4a

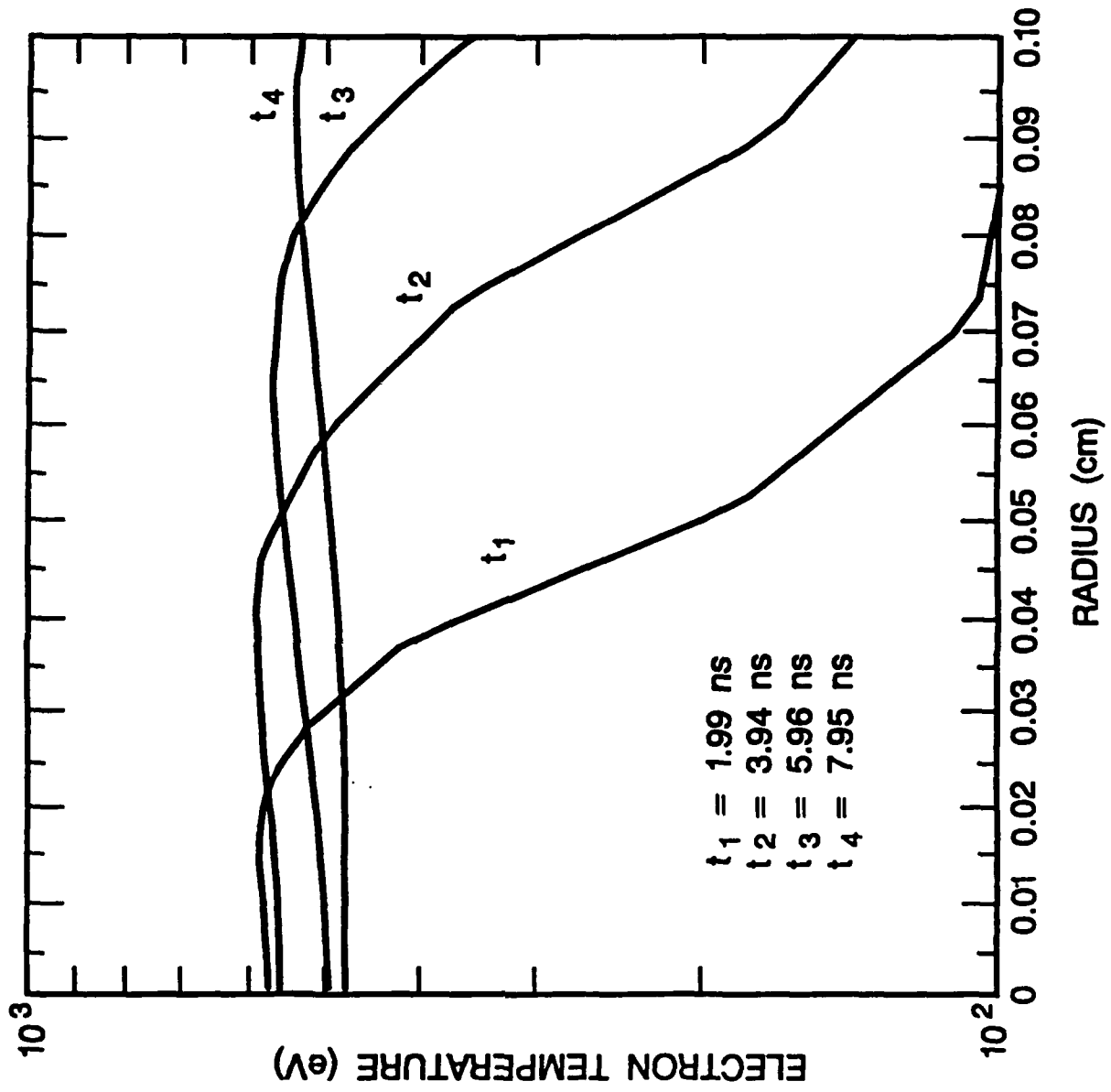


Fig. 4b

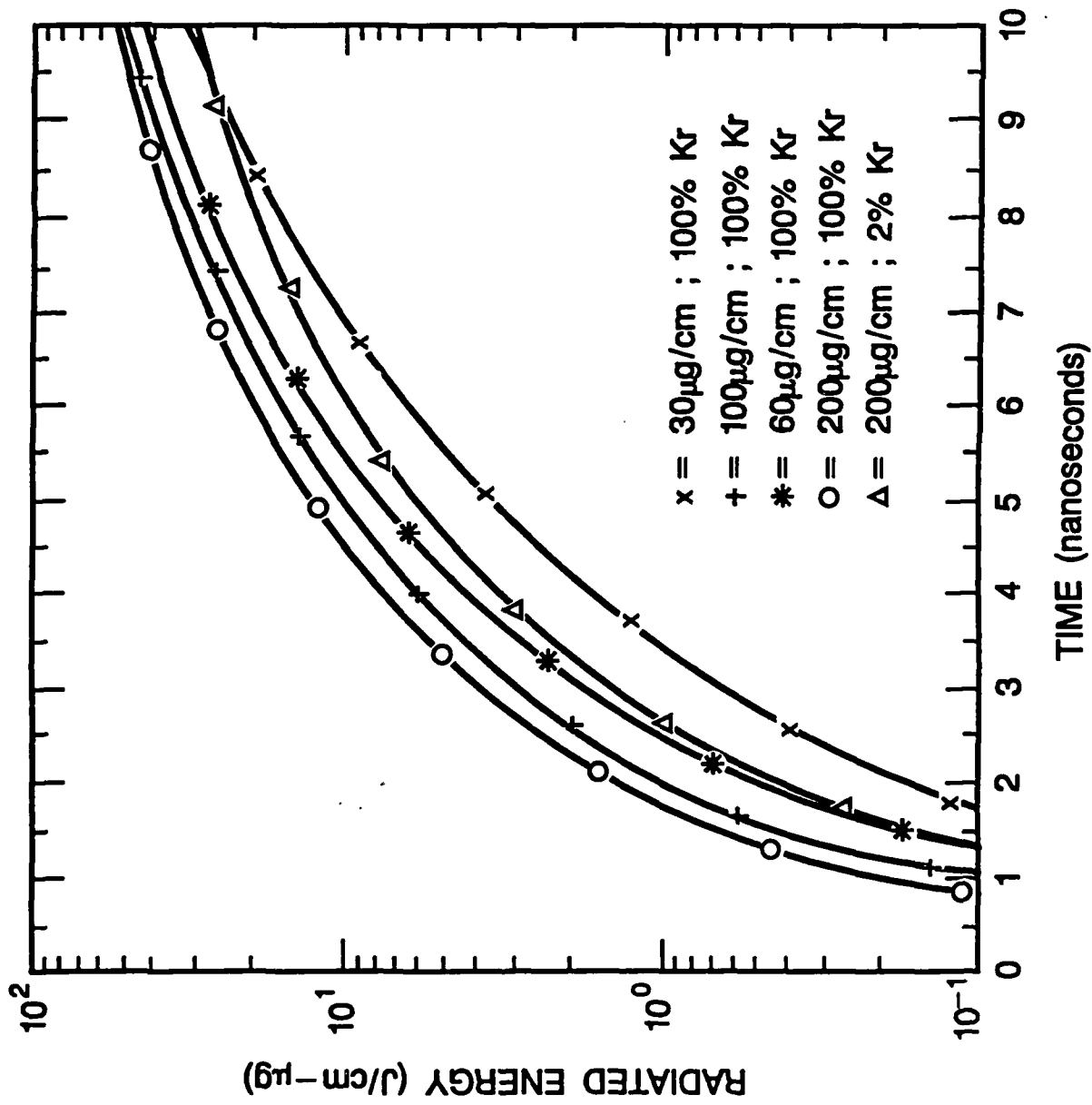


Fig. 5

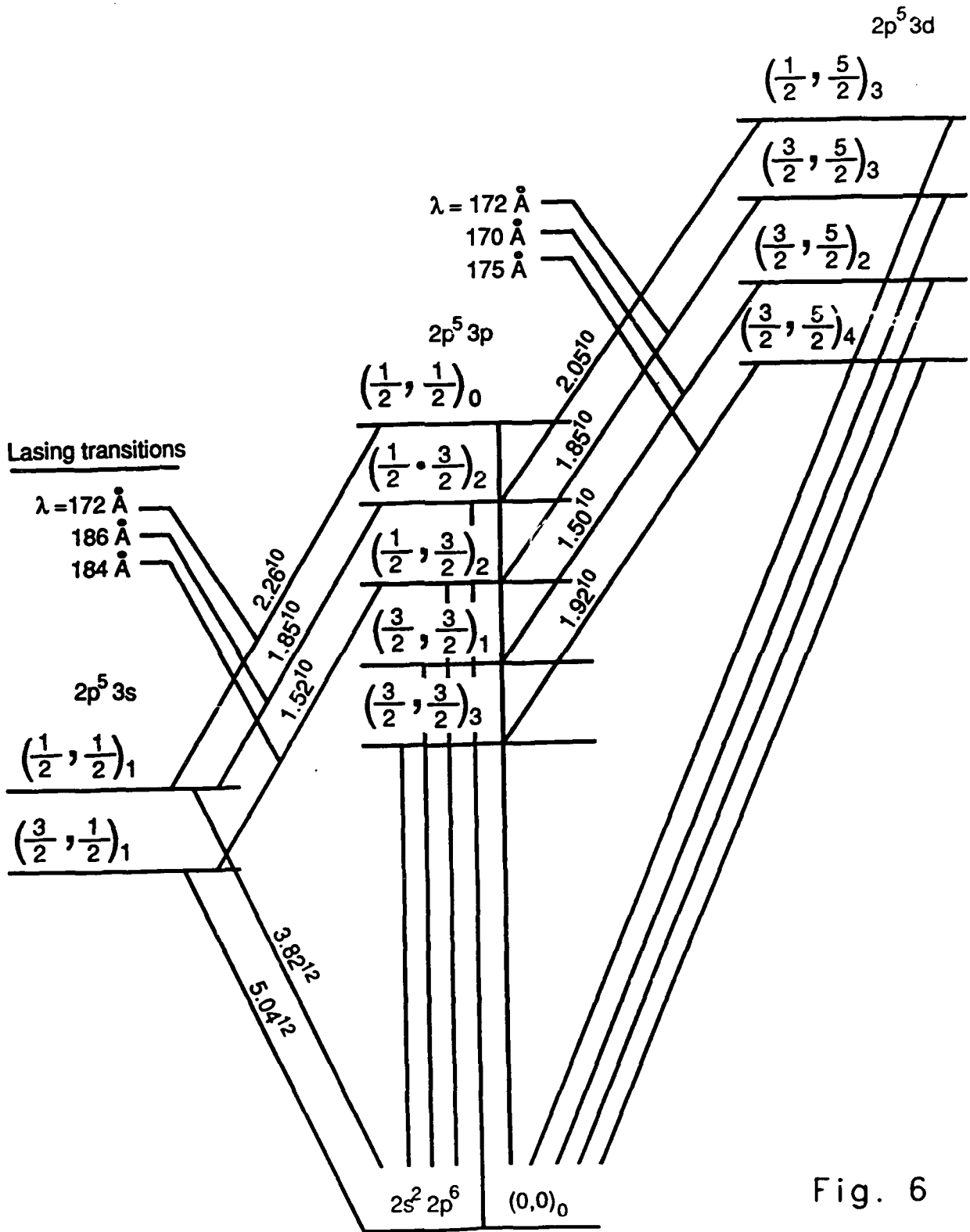


Fig. 6

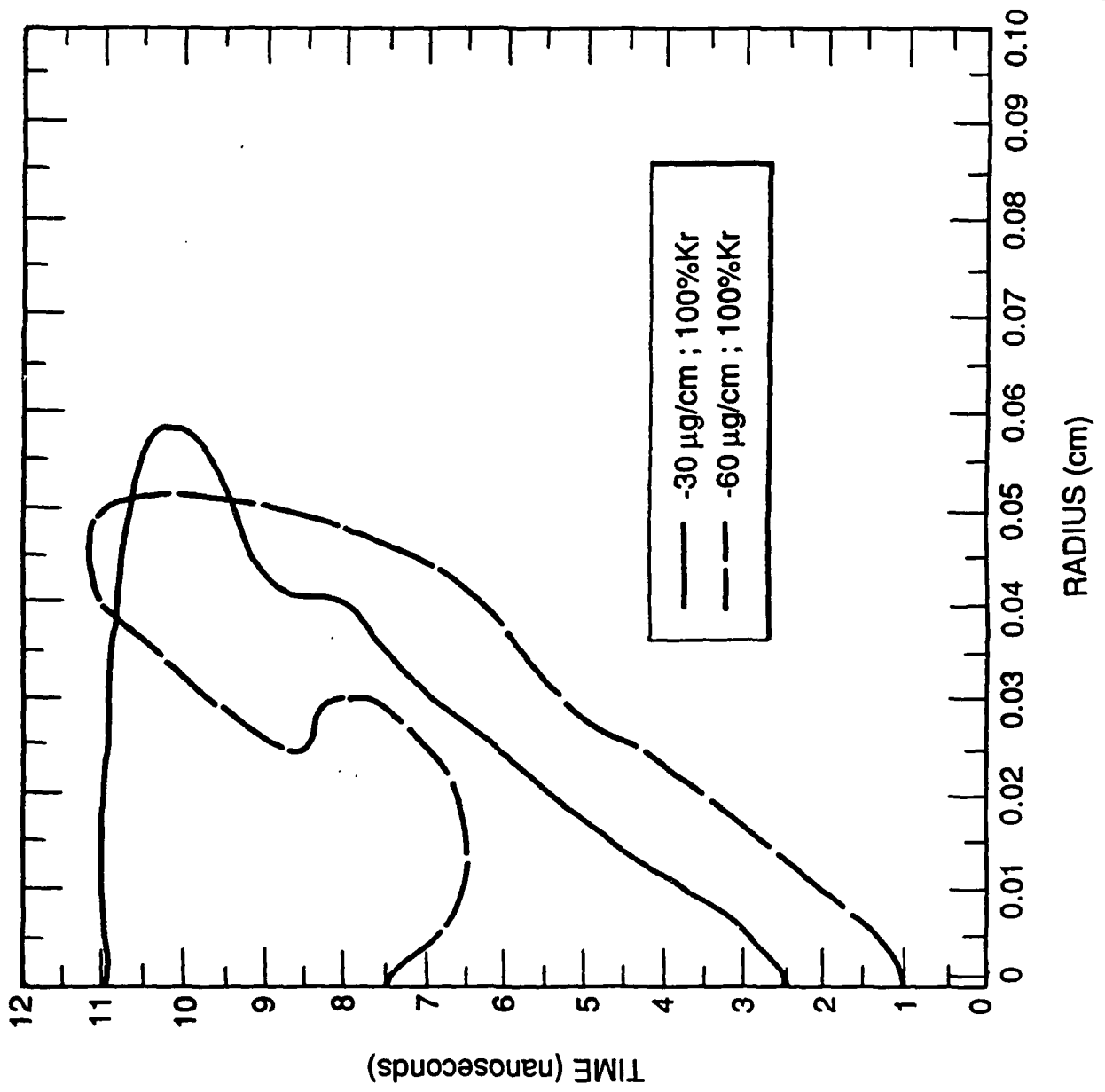


Fig. 7

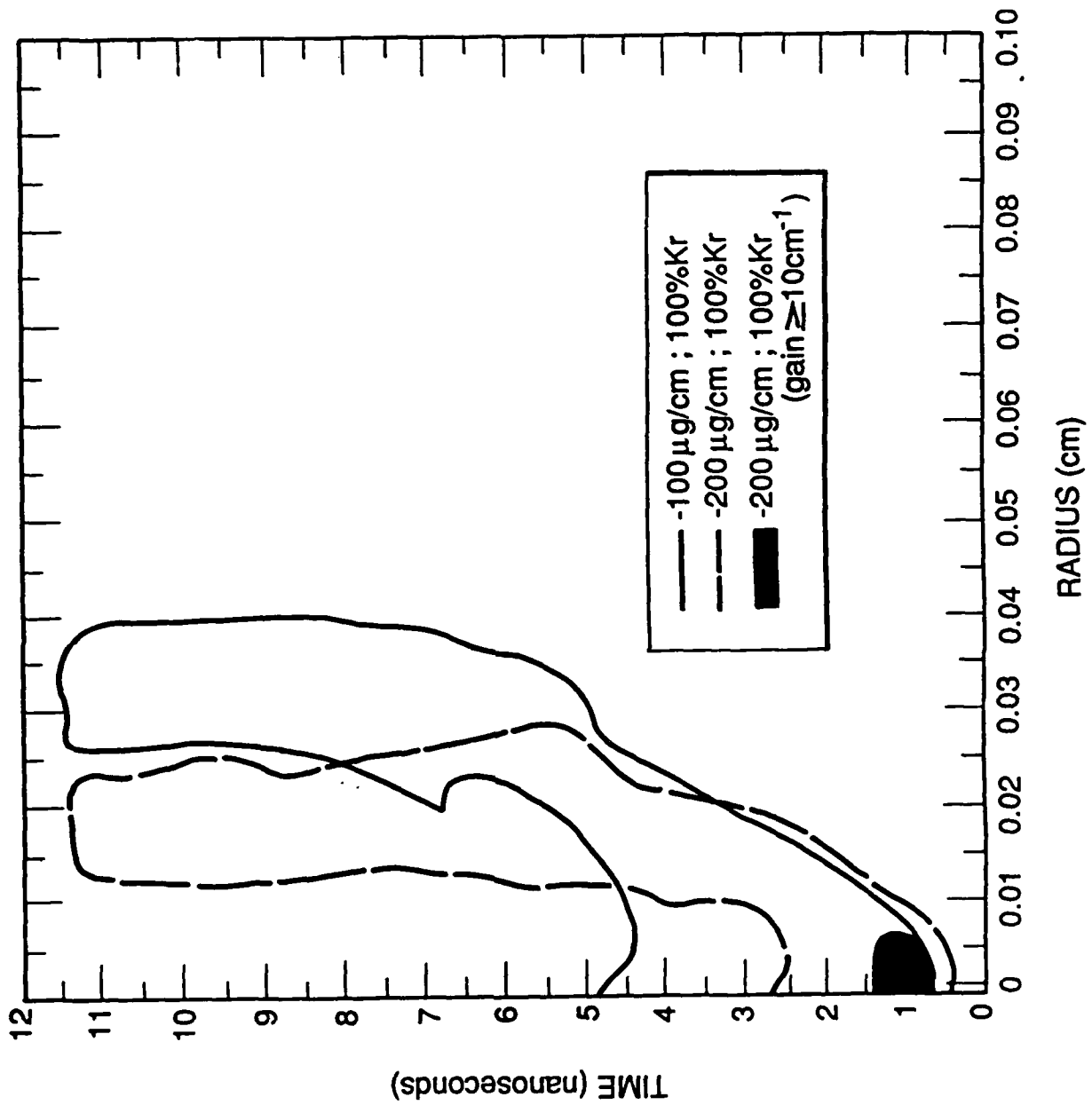


Fig. 8

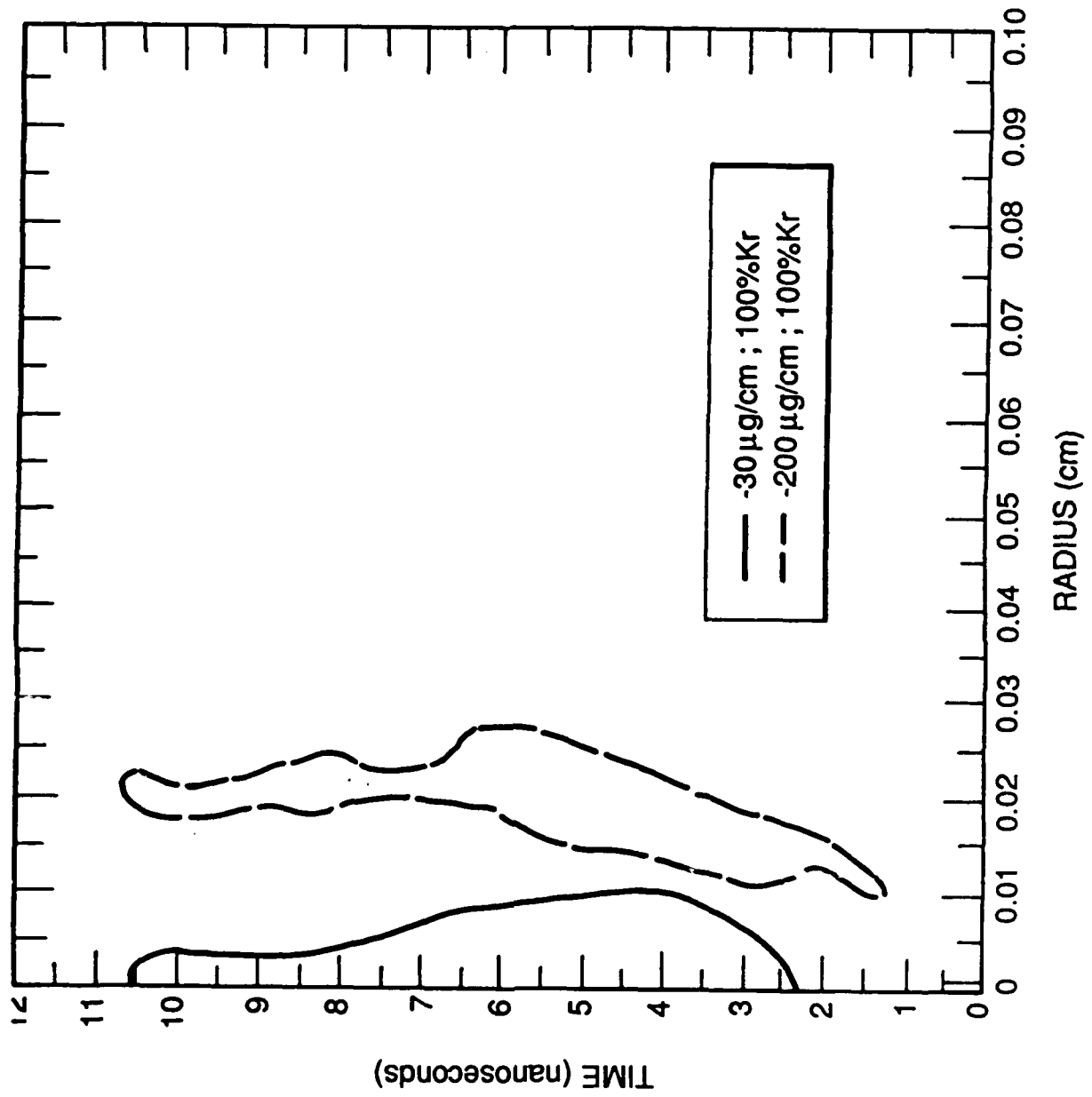


Fig. 9

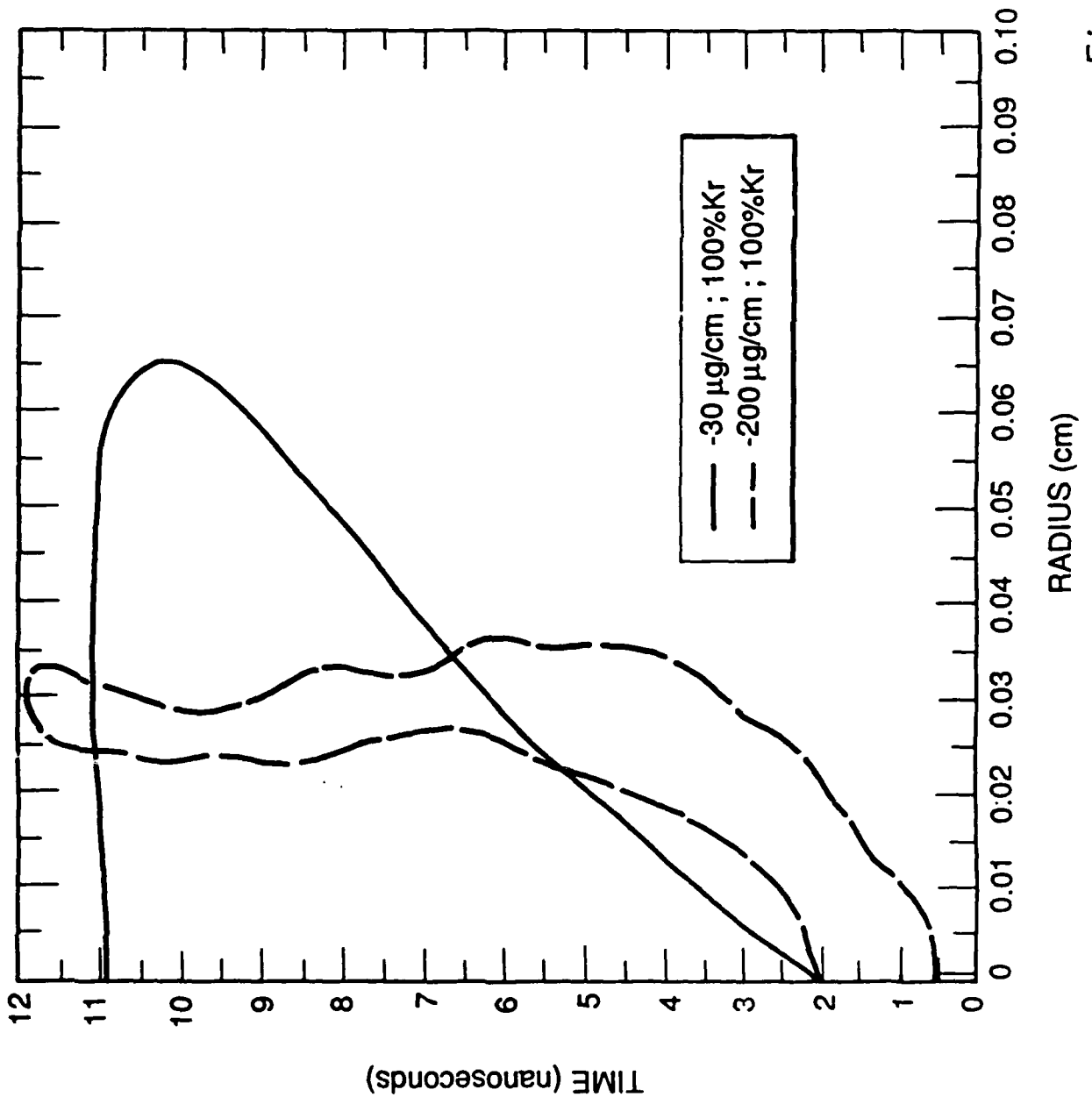


Fig. 10

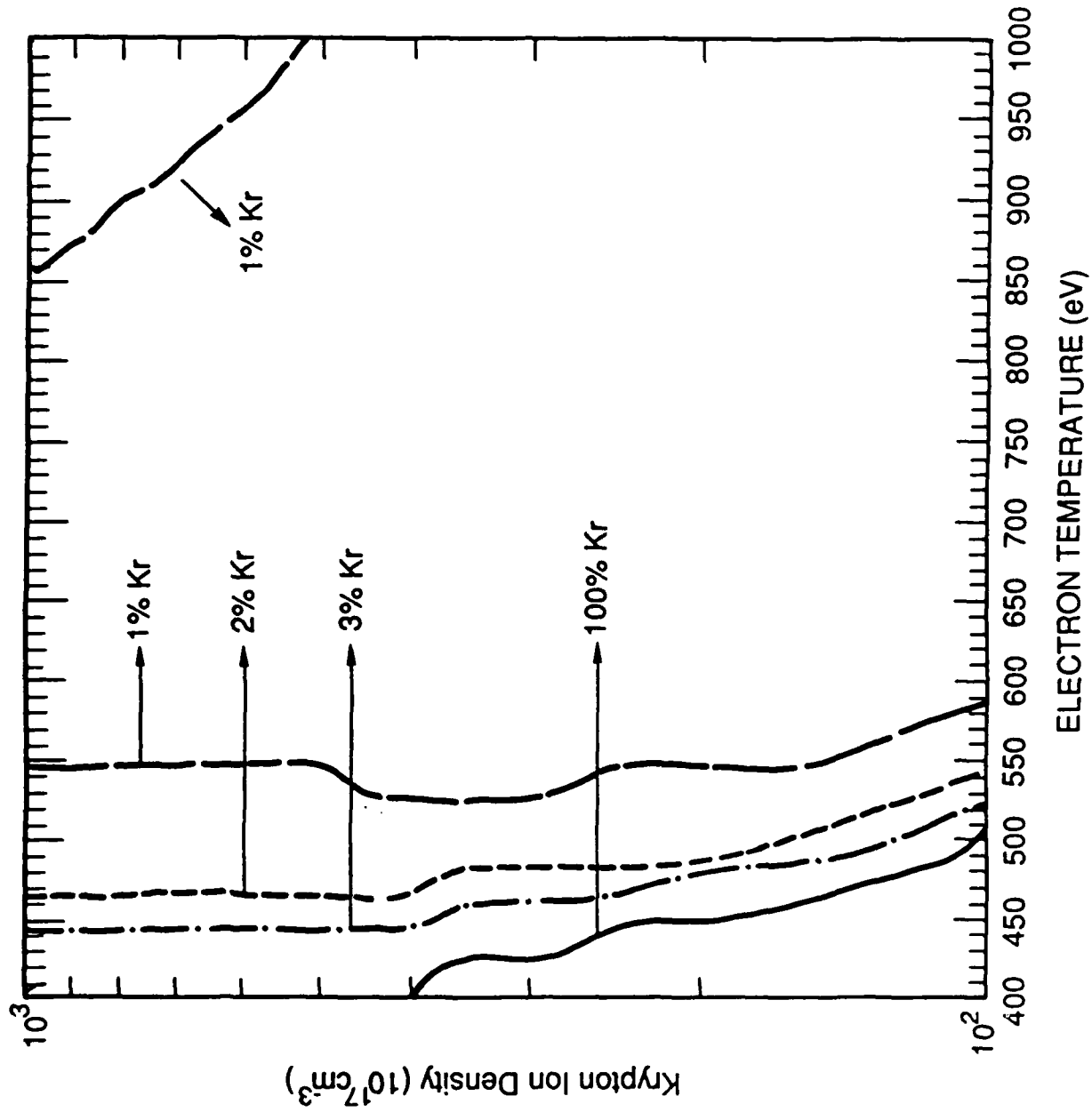


Fig. 11

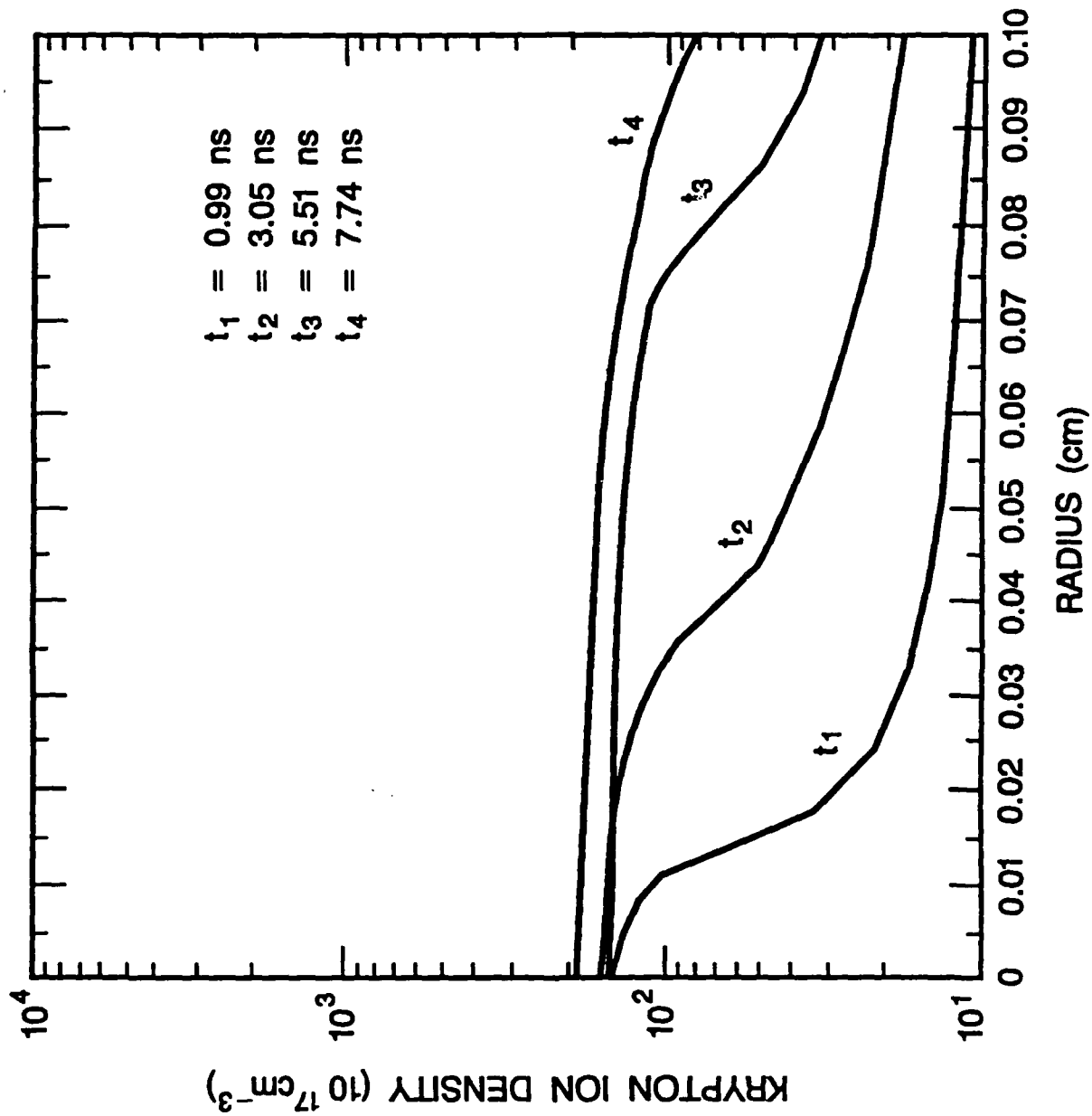


Fig. 12a

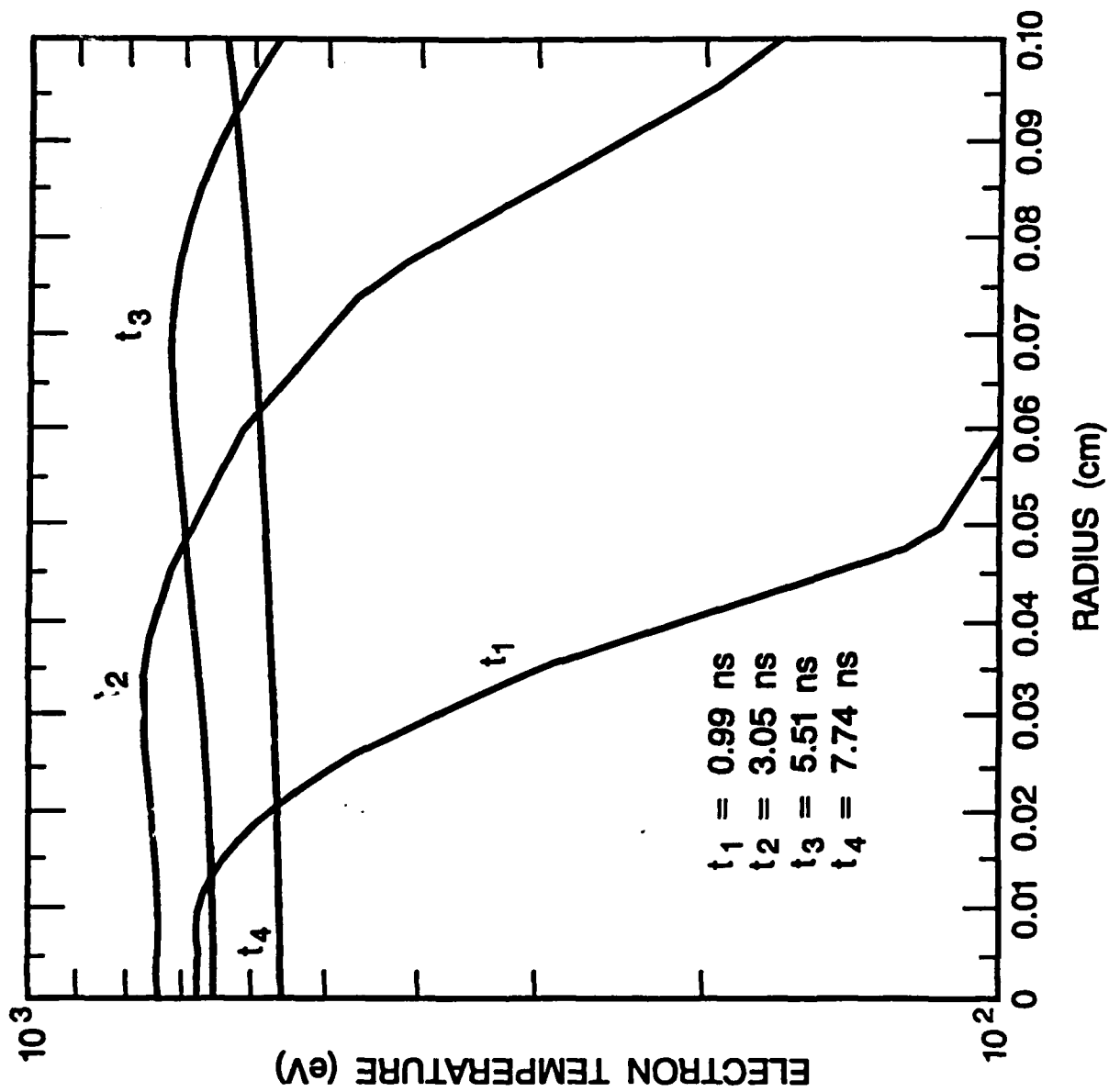


Fig. 12b

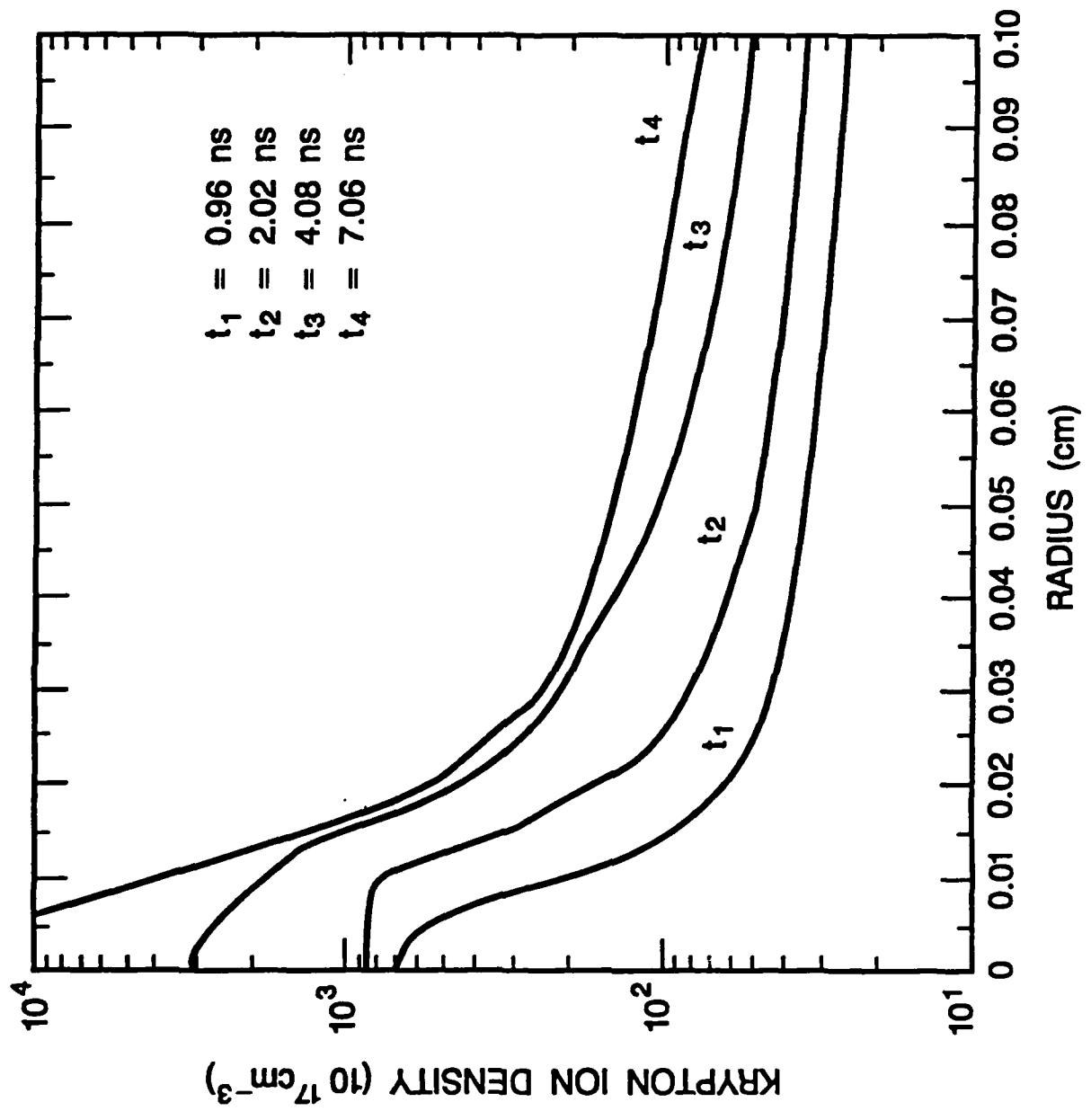


Fig. 13a

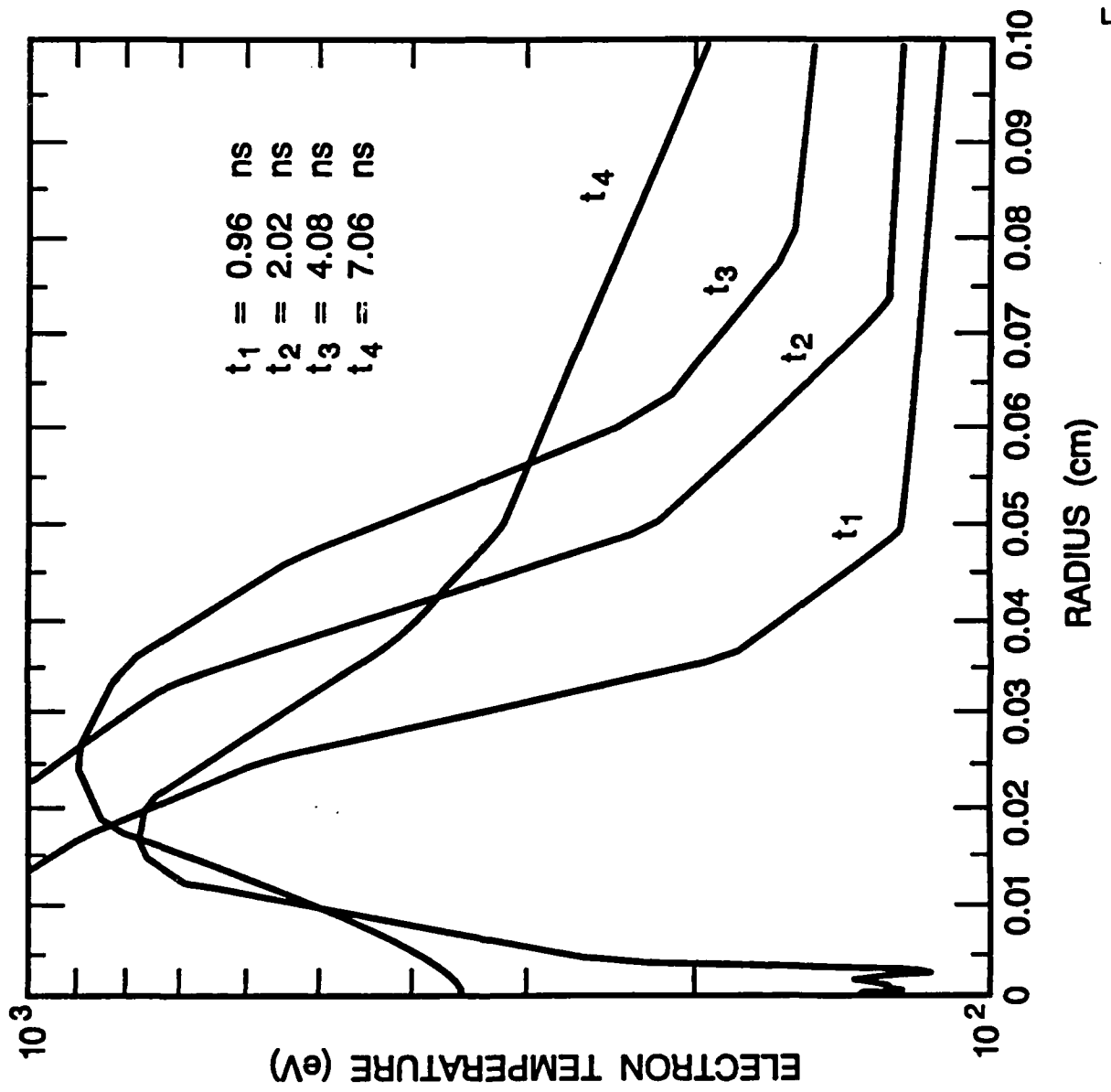


Fig. 13b

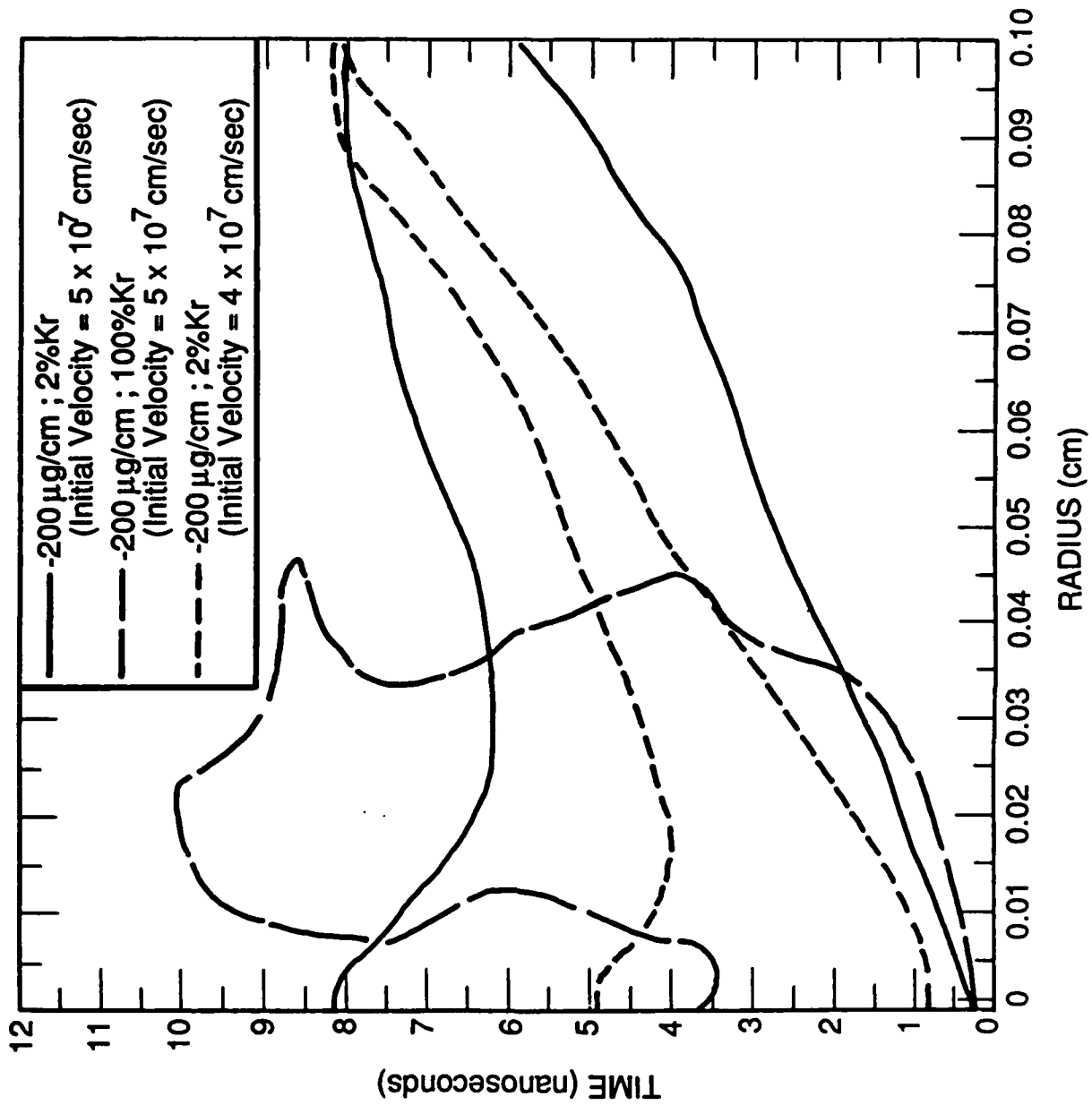


Fig. 14

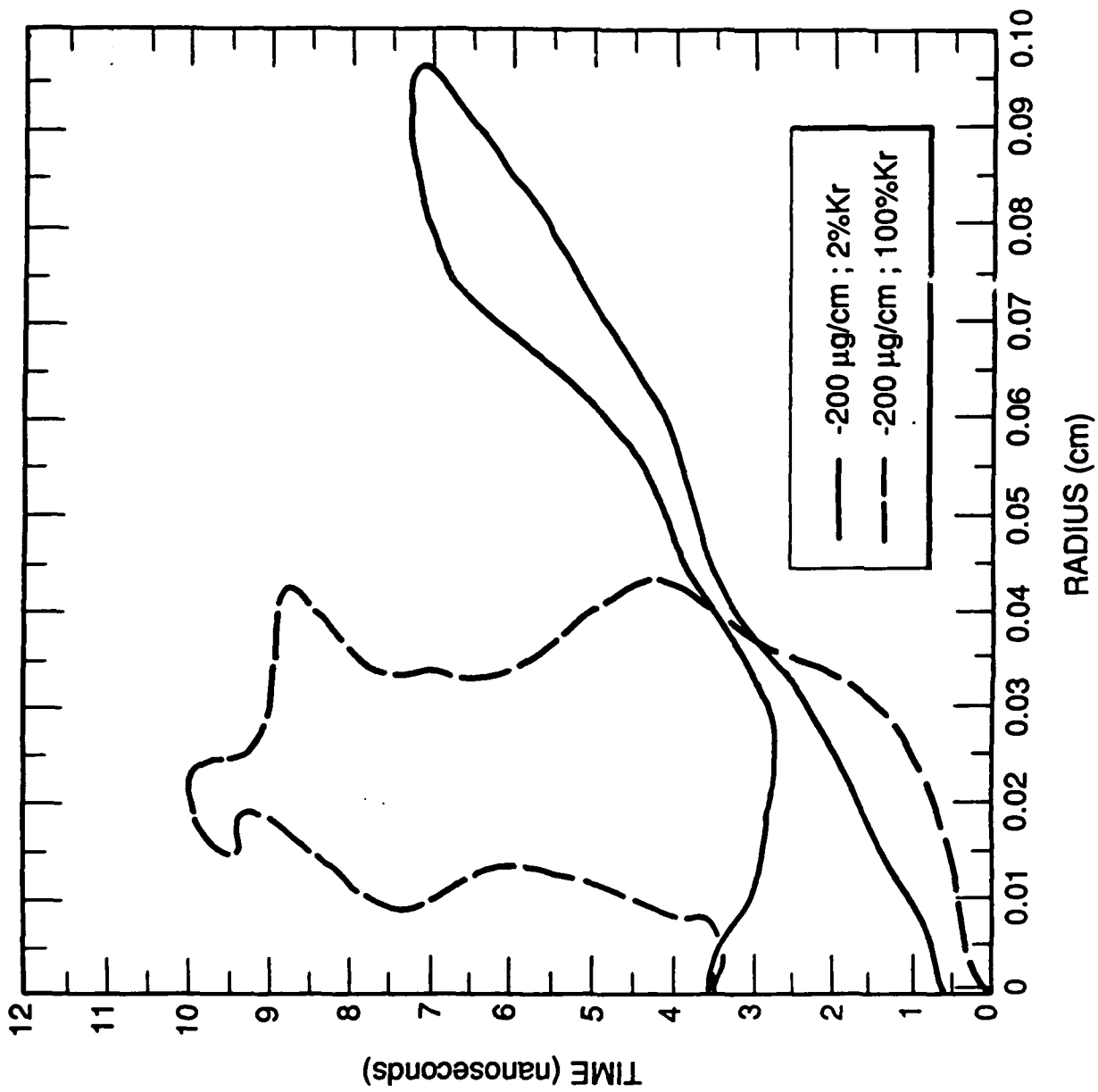


Fig. 15

ANALYSIS OF PUMPING MECHANISMS SIGNIFICANTLY AFFECTING THE GAIN OF  
SOFT X-RAY LINES IN NEONLIKE SELENIUM.

A. Dasgupta, and K. G. Whitney

Naval Research Laboratory  
Radiation Hydrodynamics Branch  
Plasma Physics Division

M. Buie

University of Michigan, Dept. of Nuclear Engineering,  
Ann Arbor, Michigan 48109

M. Blaha

University of Maryland, Laboratory for Plasma Research  
College Park, Md. 20742

ABSTRACT: We present gain calculations of the most important 3p-3s ( $J=2-1$  and  $J=0-1$ ) transitions of neonlike selenium using state-of-the-art excited state couplings. The main purpose of this work is to analyze in detail the processes impacting most significantly the gain coefficients of these transitions and to determine the sensitivity of varying them on the gain. It was seen that the two most important collisional processes affecting the gain were collisional deexcitation from the excited 3d state and excitation to the  $J=0$  ( $1/2,1/2$ ) and ( $3/2,3/2$ ) levels from the ground Ne-like state. By increasing the population of the metastable 3d states to increase the pumping of the  $J=2$  3p levels, and by decreasing the direct excitation rates from the ground to the ( $1/2,1/2$ )<sub>0</sub> and ( $3/2,3/2$ )<sub>0</sub> 3p states, the relative strengths of the gain for the  $J=2-1$  to  $J=0-1$  transitions are changed drastically. These modified gains are in much closer agreement with experimental observations compared to any theoretical calculations.

## 1. BACKGROUND

Since the first demonstration of a soft x-ray laser in neon-like ions<sup>1,2</sup> several experimental and theoretical developments have occurred in order to improve calculations and measurements and achieve even a shorter wavelength x-ray laser. The 3p-3s transitions in the neon-like system were considered a good source for lasing because the populations of the  $2s^2 2p^5 3p$  metastable states readily invert compared to the  $2s^2 2p^5 3s$  states, which can decay to the Ne-like ground state in less than a picosecond. Neon-like selenium was considered to be the most promising of all the candidate ions having the highest gain. Several atomic models and schemes to explain the gains obtained in the NOVA experiment at Livermore (LLNL)<sup>1</sup> led to detailed theoretical calculations involving all of the mechanisms for creating the population inversion. The greatest difficulty that arose and puzzled physicists is the fact that the J=0-1 transitions near 183 Å and 169 Å, which were theoretically predicted to have the highest gain, measured very little or no gain at all. Recent improvements in the experimental<sup>3</sup> conditions and also better theoretical calculations<sup>4</sup> have lessened this discrepancy somewhat, but this disagreement remains a mystery.

## 2. PRESENT STATUS

In order to understand the large difference between theoretically calculated and the experimentally observed gain for the J=0-1 line,  $(1/2, 1/2)_0 - (1/2, 1/2)_1$ , both theoretical and experimental investigations on different ions such as yttrium<sup>1</sup>, molybdenum<sup>5</sup>, germanium<sup>6</sup>, copper<sup>6</sup>, Ga<sup>7</sup> and As<sup>7</sup> were carried out. The yttrium experimental result<sup>5</sup> was ambiguous because of a line coincidence between the J=0-1 and one of the J=2-1 transitions. The experimental result of molybdenum<sup>6</sup> showed results similar to selenium. However, for copper<sup>7</sup> considerable gain was seen for the J=0-1 transition.

It was agreed that a better understanding of the kinetics involved in populating the levels responsible for the lasing transitions was definitely necessary. In the atomic models used, collisional excitation was thought to be the most important process in populating these levels. Although other ionization and recombination processes were included, only a rough estimate of them were taken into account in the kinetic calculation. It was also thought that even though the  $J=0$  upper states were populated mostly by collisional excitation, the  $J=2$  upper lasing states were populated more by dielectric recombination (DR) from fluorine-like ground state than by direct excitation from the neon ground state. Thus DR was seen to have a significant effect on the gain calculation of the lasing levels and the inclusion of the DR rates into the kinetic model seemed absolutely essential<sup>8,9</sup>. However, such inclusion still did not explain the "J=0" mystery. Previous calculations included only a ground-to-ground DR rate. We calculated the DR rates from the ground state and  $\Delta n=0$  excited state of the fluorine-like ion to each specific excited state of neon-like selenium. Thus in our CRE (Collisional Radiative Equilibrium) calculation, we used detailed and actual state specific DR rates. Recently, the theoretical group at Livermore<sup>4</sup>, also improved their calculation by including state specific DR rates to each of the lower and upper lasing levels. This new calculation when compared to their new improved measurement<sup>3</sup> is in much closer agreement. The better agreement resulted because of improvement and increase of the gain of the  $J=2$  lines compared to the  $J=0$  lines. The gains for the  $J=0$  line also decreased in the new calculations. Reanalysis of the gain of the  $J=0-1$  line in the measurement showed a noteworthy gain of  $2 \text{ cm}^{-1}$ .

It was also shown that inner-shell ionization<sup>10</sup> of sodium-like ions could be comparable to electron excitation from neon-like ions. In fact inner-shell ionization did produce population inversion favoring the  $J=2-1$  inversion over

the J=0-1. This was definitely in the direction of the experimental findings. However, for this calculation, we have not taken into account any contributions from inner shell ionization of Na-like ion. This is justified by the fact that at the temperatures of concern in a CRE calculation, the fraction of sodium-like selenium ions is much less compared to the fraction of neon like or fluorine-like selenium ions.

We have also included resonance excitation (REX) from the neon-like ground state to the 3s and 3p excited states in our kinetic calculation. To the best of our knowledge, none of the published theoretical calculations mention the inclusion of REX in their work. In a previous calculation, resonance excitation seemed to have a significant effect on the gain for the total 3p-3s gain coefficient. However, when we included state specific resonance excitation rates in the gain calculation, they did not seem to change the gain coefficients much for the multiplet J - J transitions.

Very recently substantial gain has been measured for the J=2-1 transition of neon-like strontium<sup>11</sup>. The J=0-1 transition, analogous to the J=0-1 at 183 Å, was not observed due to a wavelength overlap with a Na-like Sr line.

### 3. CALCULATIONAL MODELS

Our theoretical model has been developed with an emphasis to include and understand the processes responsible for population inversion in the laser scheme. This stems from our efforts to calculate the gain coefficient for the lasing lines measured experimentally, and to analyze the reasons behind the relative strengths of the J=0-1 and 2-1 lines in the experimentally observed and theoretically calculated gain coefficients. As mentioned earlier, the two J=2-1 lines in the NOVA experiment at LLNL<sup>3</sup> were measured to have the highest and

almost equal gains. Until recently<sup>4</sup>, the shorter-wavelength J=2-1 line was predicted to have a much higher gain<sup>12</sup>. Also the J=0-1 line near 183 Å showed a measurable gain only in the recent LLNL experiment<sup>3</sup> whereas theoretical calculations still show maximum gain for this transition. So all of our efforts went into detailed analysis of how each of these levels were populated or depopulated. As mentioned by Whitten et al.<sup>12</sup>, inclusion of 3p-3p collisions tend to equalize the gain of the two J=0-1 lines. Our gain calculation involves a CRE calculation of the populations of all ionization stages including a detailed calculation of all neon-like excited state abundances of interest. In calculating the kinetics of neon-like selenium, we have included 19 excited states. These states include all the multiplet levels of the 3s and 3p states as shown in Fig. 1, as well as a lumped 3d state, the inner shell excited 2s2p<sup>6</sup>3s, 2s2p<sup>6</sup>3p, 2s2p<sup>6</sup>3d states, and the n=4 state. We also show in this figure the important lasing lines and the wavelengths for the transitions.

The processes connecting these levels are collisional excitation, collisional deexcitation, radiative decay, dielectronic recombination from the fluorine-like ionization stage, and resonance excitation. Fig. 2 shows an energy level diagram for one of the J=0 and J=2 upper lasing level pairs that summarizes the strengths of the three most important pumping mechanisms that populate them from the fluorine-like and neon-like ground states and the 3d excited state. The dark arrows indicate which of the two rates from each of these states is the strongest. We notice that this J=0 level is pumped strongly only by collisional excitation from the ground Ne-like state. The J=2 level, however, is populated preferentially both by collisional deexcitation from the 3d excited state and by recombination (DR) from the F-like ground state. The population of the 3d excited states thus most directly affects the population of the J=2 level. This 3d excited state is directly populated by collisional excitation from the Ne-like ground state, and by direct and cascade recombinations as indicated in the figure. It is depopulated in our model by a

strong radiative decay to the ground state since we lump the 3d multiple states into one state in our calculation. Energy levels and radiative, as well as autoionization, rates as needed for dielectronic recombination and resonance excitation rates were calculated using the HFR (Hartree-Fock with relativistic correction) method of R. D. Cowan<sup>13</sup>. The DR rates populate the J=2 levels of the 3p multiplet much more strongly than they do the J=0 levels. Thus inclusion of accurate and state specific DR rates (for each excited multiplet level) into the rate equations was done in order to determine their importance in obtaining closer agreement with experiment. This had been claimed by London et al.<sup>4</sup>. We have taken into account a complete set of doubly excited states in calculating the DR rates<sup>14</sup>. For low lying doubly excited states, these DR rates were explicitly calculated. For higher Rydberg states we have lumped the states and we noticed that the DR rates fell off as  $1/n^3$  where n denotes the principal quantum number of the Rydberg electron. The resonance excitation (REX) rates were calculated in the resonance approximation following Cowan<sup>15</sup>. They were calculated in a way that was very similar to the DR rates. The REX rates to the 3s lasing levels are much larger than those to the 3p lasing levels and the inclusion of these rates, therefore increases the 3s populations and decreases the calculated gain coefficients. Since the calculated gains tend to be much larger than the experimentally measured gain, the mechanism of resonance excitation definitely moves the calculation in the direction of experiment.

It is seen in Fig. 2 that deexcitation of the 3d excited levels to the 3p multiplet is stronger for the two J=2 levels than for the J=0 levels. Therefore it is important to calculate these rates accurately in order to explain the experimental observation. There is strong radiative decay from only the  $^3D_1$  and  $^1P_1$  levels of the 3d excited states to the ground state. Since we have lumped all of the levels of the 3d states into a single state in our model this reduces the populations of the 3d states that do not decay to the ground state and are metastable. This in turn gives us lower deexcitation pumping of the 3p states

and hence lower gain coefficients for the  $J=2$  transitions. By decreasing the radiative rate and thereby increasing the 3d population we can get a much better estimate of the pumping rate to the 3p levels. In this work we concentrated on those atomic processes which influence the gain most significantly. The results of these investigation are shown in the next section.

The collisional excitation rates from the neon-like ground state are taken from Zhang et al.<sup>16</sup>. The collisional ionization rates from the 3s sublevels are obtained from Golden et al.<sup>17</sup> and the ionization rates from the 3p and 3d sublevels are taken from Moore et al.<sup>18</sup>. We have used the relativistic distorted wave 3s-3s, 3s-3p, 3p-3p, 3s-3d and 3p-3d coupling rates calculated by P. Hagelstein and R. Jung<sup>19</sup>. All of the above collision cross sections that were used in our calculations are recently calculated and are considered state-of-the-art.

We have obtained the excitation and deexcitation, ionization and recombination rates by integrating the cross sections over a Maxwellian electron distribution function for the appropriate temperature. These were then used in the CRE calculations to obtain the ionization abundances and excited state populations. The gain coefficient for a particular transition was then easily found as a function of ion density at a specific electron temperature or as a function of electron temperature at a specific ion density.

#### 4. RESULTS

The collision strengths for the 3p multiplet levels as obtained from Ref. 16 are shown in Fig. 3. We notice that these strengths are largest for the  $J=0$  and  $J=2$  multiplet lasing levels of the 3p excited state. However, the collision excitation rate to the  $J=0$  levels are much larger than those to the  $J=2$  levels.

This accounts for the large calculated gain coefficients for the two  $J=0-1$  lines as will be shown later. The collision strengths for other levels of the  $3p$  state fall off very rapidly with energy as also shown in Fig. 3. We have thus focused our attention on the processes pumping these  $J=0$  and  $J=2$  levels in order to make theoretical calculations of the sensitivity of the gain calculations on these atomic processes.

Fig. 4 shows four  $3p-3d$  collision strengths as obtained from Ref. 19. As mentioned before, this figure shows that collisional deexcitations to the  $J=2$  levels are much larger than those to the  $J=0$  levels. A detailed description of the dominant couplings between the  $3d$  and  $3p$  states is shown in Fig. 5. In the CRE gain calculations, the  $3p$  states are populated much more by collisional deexcitation than radiative decay from the  $3d$  states. Note that the  $J=0$   $3p$  states are strongly coupled to the only two  $3d$  states that strongly radiate to the ground state. The  $J=2$  states are strongly coupled to metastable  $3d$  states. Thus the reduced populations of the decaying  $3d$  states will tend to increase the  $J=0-1$  gain compared to the  $J=2-1$  gain in our calculation.

In Fig. 6 we show how dielectronic recombination (DR) feeds the most important upper and lower lasing levels<sup>14</sup>. We can clearly see how the  $J=2$  levels can receive substantial population directly from the fluorine-like ground state via dielectronic recombination when these states are highly populated. A similar result holds for DR recombination from the  $\Delta n=0$  F-like state. The rates to the  $J=0$  levels of the  $3p$  state are comparable to the rates to the  $J=1$  levels of the  $3s$  lower state and are much smaller than those to the  $J=2$  levels. This should tend to increase the gain of the  $J=2-1$  transition and somewhat reduce the  $J=0-1$  gain when the population ratio of the F-like to Ne-like ground state is increased as pointed out in Ref. 12.

As explained at great length in Ref. 14, our DR rate calculations involve a large number of doubly excited states. We have also included additional autoionization to excited states of the initial ion. Our DR rates agreed very well with the detailed multi-configuration Dirac-Fock (MCDF) calculation of M. C. Chen<sup>20</sup>. However, Chen reports only total ground-to-ground rate coefficients and as already mentioned we needed very accurate DR rates to each of the multiplet levels of the 3s and 3p excited states. When we added our individual DR rates and obtained a total ground-to-ground rate, it was in very close agreement with Chen's rate.

We have also included resonance excitation (REX) rates to each of the multiplet levels of 3s and 3p states in our atomic model. These level specific REX rates were also compared with those of Chen<sup>21</sup>. For the 3s multiplet levels our rates compare quite well with Chen's. Our calculated REX rates to the multiplet levels of 3p excited state are lower than those of Chen. Even though we included these very detailed and accurately calculated REX rates in our CRE calculation, there was more effect on the gain calculation of the total 3p-3s transition due to the inclusion of these rates than there was for the multiplet J-J transitions.

Our somewhat simplified but complete model of 19 singly excited states of Ne-like selenium gave the relative strengths of the different pumping mechanisms populating the J=0 (1/2,1/2) 3p level as a function of temperature shown in Fig. 7. Fig. 8 shows how the J=2 (1/2,3/2) 3p level is populated by these same processes. When we compare Figs. 7 and 8, we see that in CRE the J=0 level is pumped overwhelmingly by collisional excitation from the ground state; whereas, the J=2 level is populated competitively by collisional deexcitation from both the 3d and n=4 states. The strength of the DR pumping rates to both these levels are smaller than either the collisional excitation from the ground state or deexcitation from higher states including collisional cascade from n=4

excited state, which is originally fed by DR and 3-body recombination. It is evident from these figures that collisional excitation from the ground state, the most important mechanism for populating the J=0 upper laser state, has a much larger pumping rate than DR, which is an important mechanism populating the J=2 upper state. This will explain the much larger gain for the J=0-1 transitions compared to the gain of J=2-1 transitions in this model. The pumping rates from other processes such as collisional cascade from the 3s, 3p and 3d inner shell states and radiative decay from the 3d excited states are much smaller.

Neon-like selenium ions have a maximum abundance for electron densities between  $10^{19}$  and  $10^{21}$   $\text{cm}^{-3}$ , but as shown in Ref. 12, the maximum of this ion fraction varies rapidly with electron temperature  $T_e$ . In order to calculate the gain coefficient for different plasma conditions, it is necessary to obtain the fraction of neon-like selenium as a function of electron or ion density at different electron temperatures and vice versa and then obtain the gain coefficients at those plasma conditions. Our complete CRE calculations allow us to do this self-consistently. Table I lists the identifications of the most important lasing lines considered in these calculations and labeled in the following gain figures.

The variation of the gain coefficients of the lasing lines as a function of ion density at an electron temperature of 1 keV is shown in Fig. 9. The variation of these gain coefficients as a function of temperature for an ion density of  $10^{19}$  ( $\text{cm}^{-3}$ ) is also shown in Fig. 10. We see from this figure that the gain curves for all the lines tend to peak around  $T_e = 900$  eV. However the gain curves for the lasing lines at  $T_e = 1$  keV peak at different densities for different lines in Fig. 9. The J=0 lines have maximum gain at much higher densities compared to the J=2 lines. Thus when comparing experimentally

measured gains for these lines, one has to bear in mind that the plasma conditions should be measured carefully.

As mentioned earlier, we have included all the multiplet levels of the 3s and 3p excited states in our atomic model, but lumped all such levels for the 3d excited state into one level. This causes some inaccuracy in calculating the 3d population because of the metastability of a preponderance of these levels. There are strong dipole transitions to the ground state from only the  $(2p_{1/2}3d_{3/2})_{J=1}$  and  $(2p_{3/2}3d_{5/2})_{J=1}$  levels of the 12 3d multiplet states and these are coupled strongly only to J=0 states. By treating all the 12 levels as one single level and in effect allowing radiative decays from all of them, we have decreased the populations of the metastable 3d states from what they should be. Thus, the J=2 lines should be pumped more significantly by collisional cascade from these 3d levels than the J=0 lines are. Lowering the population of the 3d lumped state causes a lower gain calculation for the J=2 levels. In order to evaluate this effect, we increased the population of the 3d state by gradually reducing the radiative decay rate from this state while recalculating the gain coefficients for all the lines. The results of this analysis is shown in Fig. 11. The gain coefficients of the lines are plotted as a function of  $\epsilon$  which is defined by the equation

$$A'_{g,3d} = (1-\epsilon) A_{g,3d} + \epsilon \frac{A_{g,3d}}{10}, \text{ where } A_{g,3d} \text{ is the radiative decay rate to the}$$

ground state and  $A'_{g,3d}$  is the modified decay rate. As  $\epsilon$  goes from 0 to 1, the 3d decay rate is decreased by a factor of 10. Because the 3d to J=0 couplings are weak (Fig 4) the gain curves remain almost constant for the J=0 lines; whereas they increase with increasing 3d population for the J=2 lines. Fig 11 demonstrates the fact that an accurate calculation of the populations pumping the different lasing levels is crucial for an accurate gain determination.

In Fig. 12 we show how the gain curves for the different lines behave as we simultaneously decrease the collisional rates to the J=0 levels by a factor of three. Here the gain coefficients for all the lines are plotted as a function of  $\epsilon$  where  $\epsilon$

is defined by  $\Omega'_{J=0} = (1-\epsilon) \Omega_{J=0} + \epsilon \frac{\Omega_{J=0}}{3}$ , where  $\Omega_{J=0}$  is the collisional

excitation (CE) rate from ground to either the J=0 (1/2,1/2) or (3/2,3/2) levels and  $\Omega'_{J=0}$  is the modified CE rate. As expected the gain for the J=0 lines decrease with these lower J=0 rates significantly while the gain for the J=2 lines increases more slowly. This figure shows how an inaccuracy in calculating the collisional excitation rates of the size generally regarded as representing the limits achievable theoretically affects the gain calculation. We have incorporated both of the effects shown in Figs. 11 and Fig. 12 in our CRE calculation to obtain the gain coefficients for the important lines shown in Figs. 13 and 14. The effect of simultaneously increasing the 3d population and lowering the J=0 excitation rates from the ground state is shown in Fig. 13 as a function of density at an electron temperature of 1 keV. If we compare Fig. 13 with Fig. 9, we see a very different picture. The relative strengths of the gain coefficients for the J=2 lines compared to the gain coefficients for the J=0 lines are now reversed. In fact the J=2-1 line near 209 Å has the highest gain and the gain coefficients for the other J=2-1 line near 206 Å is close to the gain curve for the 182 Å J=0-1 transition which was always predicted to have the highest gain. The behavior of the gain curves in this figure is in much closer accord with the experimental observations than any of the calculations performed to date.

A similar change in the behavior of the gain curves is shown in Fig. 14,

where they are calculated as a function of electron temperature at an ion density of  $10^{19}(\text{cm}^{-3})$ . This figure should be compared with the curves in Fig. 10. In this case, all the  $J=2$  lines have larger gains than those for the  $J=0$  lines at their maximum. Another interesting observation worth mentioning is the fact that both the  $J=0$  and  $J=2$  curves have a maximum at around the same ion density of  $N_i = 5 \times 10^{19} (\text{cm}^{-3})$  contrary to the curves shown in Fig. 10.

## 5. SUMMARY AND FUTURE PROSPECTS

We have used an atomic model of 19 neon-like excited states and all of the important processes connecting them to calculate gain coefficients for the 3p-3s lasing transitions in CRE. The main objective of this work was not to critique previous theoretical/experimental comparisons, but to understand what the most important processes are that affect the relative magnitude of the  $J=0-1$  and  $J=2-1$  gain coefficients. Using state-of-the-art collision, DR and REX rates in our Ne-like selenium model we have reproduced all of the essential aspects of the previous gain calculations for all of the 3p-3s lasing transitions. Since the purpose of this work was to determine the sensitivity of the gain calculations to the underlying atomic processes, we did not attempt to compare in detail our results with either other theoretical calculations that were carried out to explain experimental measurements or with the experimental measurements themselves. When we make a qualitative comparison, our unmodified results are in much closer agreement with other theoretical calculations<sup>2,4</sup> compared to experimental measurements<sup>1,3</sup>. When we compare our modified gain results under similar conditions of electron temperature  $T_e$  and when the ion temperature  $T_i$  is one half  $T_e$  as shown in Fig. 14, gain in the two  $J=2-1$  lines at 206 Å and 210 Å are comparable to those of London et al<sup>4</sup>. However the relative strengths of the CRE gain in the  $J=0-1$  line at 182 Å does not compare well with those of Ref. 4. The gain obtained in our unmodified CRE calculation

for the  $J=0-1$  line gain at  $169 \text{ \AA}$  does not compare well with either other theoretical calculations or experimental measurement, but it does follow the trend of experimental results when we improve our calculation by increasing the  $3d$  population and reduce the excitation to  $J=0$  from the ground state. This is evident when we compare the results shown in Figs. 10 and 14. Thus our new calculations, with the modified  $3d$  deexcitation rate and collisional excitation rates from the ground state, as shown in Figs. 13 and 14, are definitely in accord with experimental findings. Our collision rates are the same as those used by the Livermore researchers and our DR rates compared very well with those of M. Chen<sup>20</sup>, but we could only compare total ground-to-ground DR rate. Moreover, inclusion of state specific DR rates had a minor impact in CRE on the gain calculation of the  $J=2-1$  lines in moving them closer to experimental observation in contrast to Livermore's calculations. Even though these rates were calculated in a very accurate and detailed way, variation of the gain curves as a function of these DR rates was not significant when the rates were varied by a factor of 3. In CRE in our calculation, collisional excitation pumping dominates DR pumping and so the latter will have a major influence only in a non-equilibrium plasma.

We thus intend to carry out time-dependent gain calculations to determine conditions for which the DR processes do have a large effect. Our efforts to understand how the  $J=0$  and  $J=2$  lines are populated or depopulated by different processes helped us to assess how the relative strengths of the gains of the most important lasing lines are affected as we increase or decrease their contributions. This tells us the sensitivity of the gain to the most important pumping mechanisms, but it should also motivate other researchers to more accurately recalculate or measure the rates for exciting the  $J=0$  states from the Ne-like ground state.

**TABLE I. Identification of lines with corresponding wavelengths for 3p-3s lasing transitions**

---

---

<u>LABEL</u>	<u>TRANSITION</u>	$\lambda$ (A°)
A	J=2-1	206.4
B	J=2-1	209.8
C	J=0-1	182.4
G	J=1-1	220.3
H	J=0-1	113.4
I	J=0-1	168.7

---

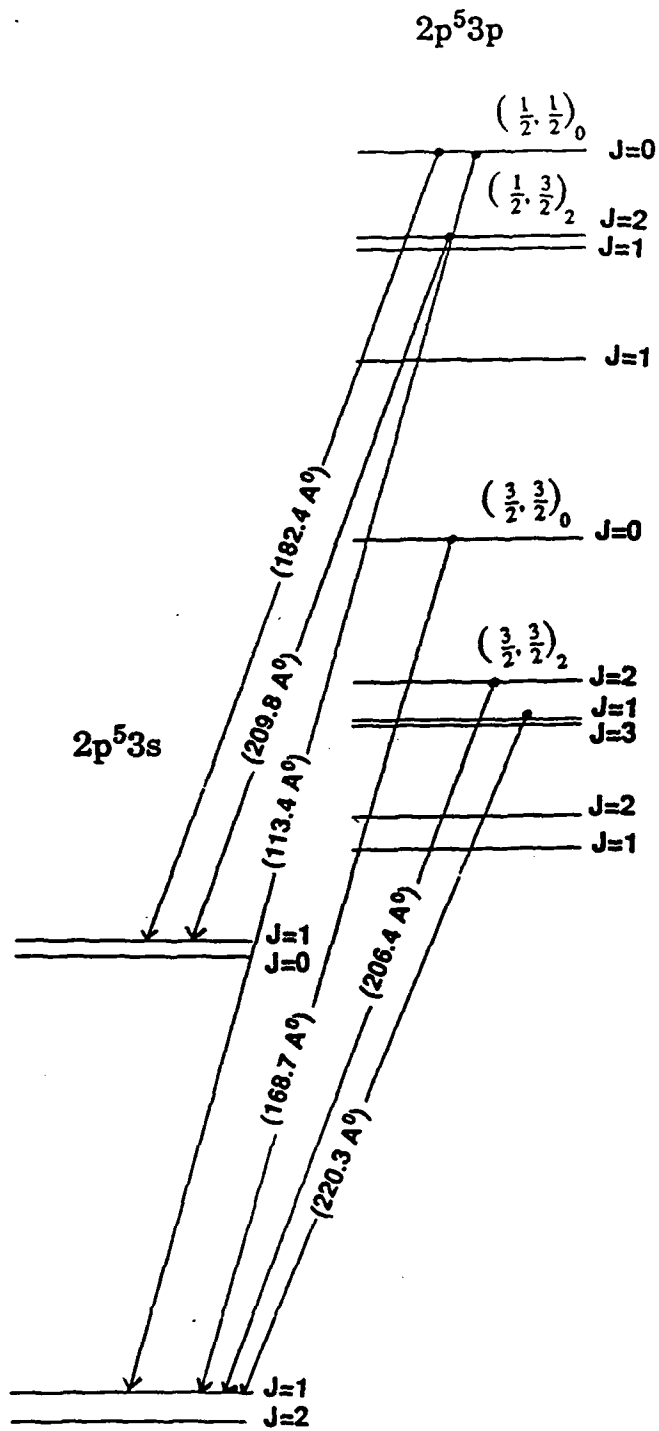


Fig. 1 Energy level diagram for the 3s and 3p multiplet levels of neon-like selenium. The strong lasing lines from  $J=0$  and  $J=2$  levels with the corresponding wavelengths are shown along with one observed transition from the  $J=1$  level.

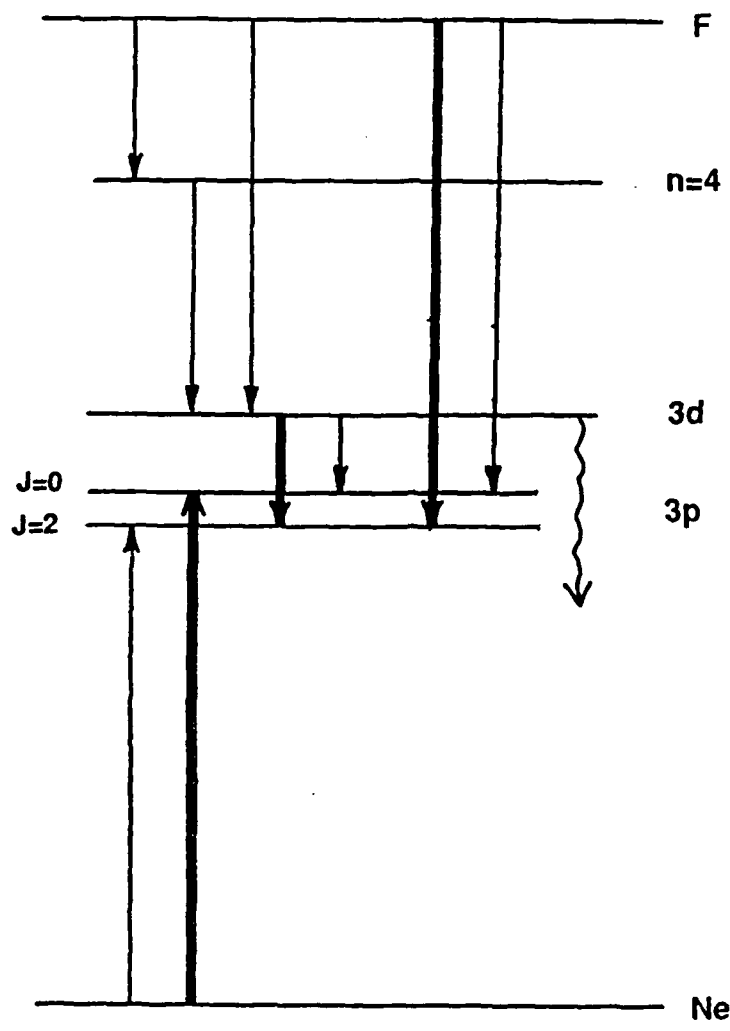


Fig. 2 Energy diagram showing the relative strengths for populating the  $J=0$  and  $J=2$   $3p$  levels from the fluorine-like and neon-like ground states and the  $3d$  excited state. The dark arrows indicate the strong pumping channels.

### COLLISION STRENGTHS OF THE 3P MULTIPLET LEVELS

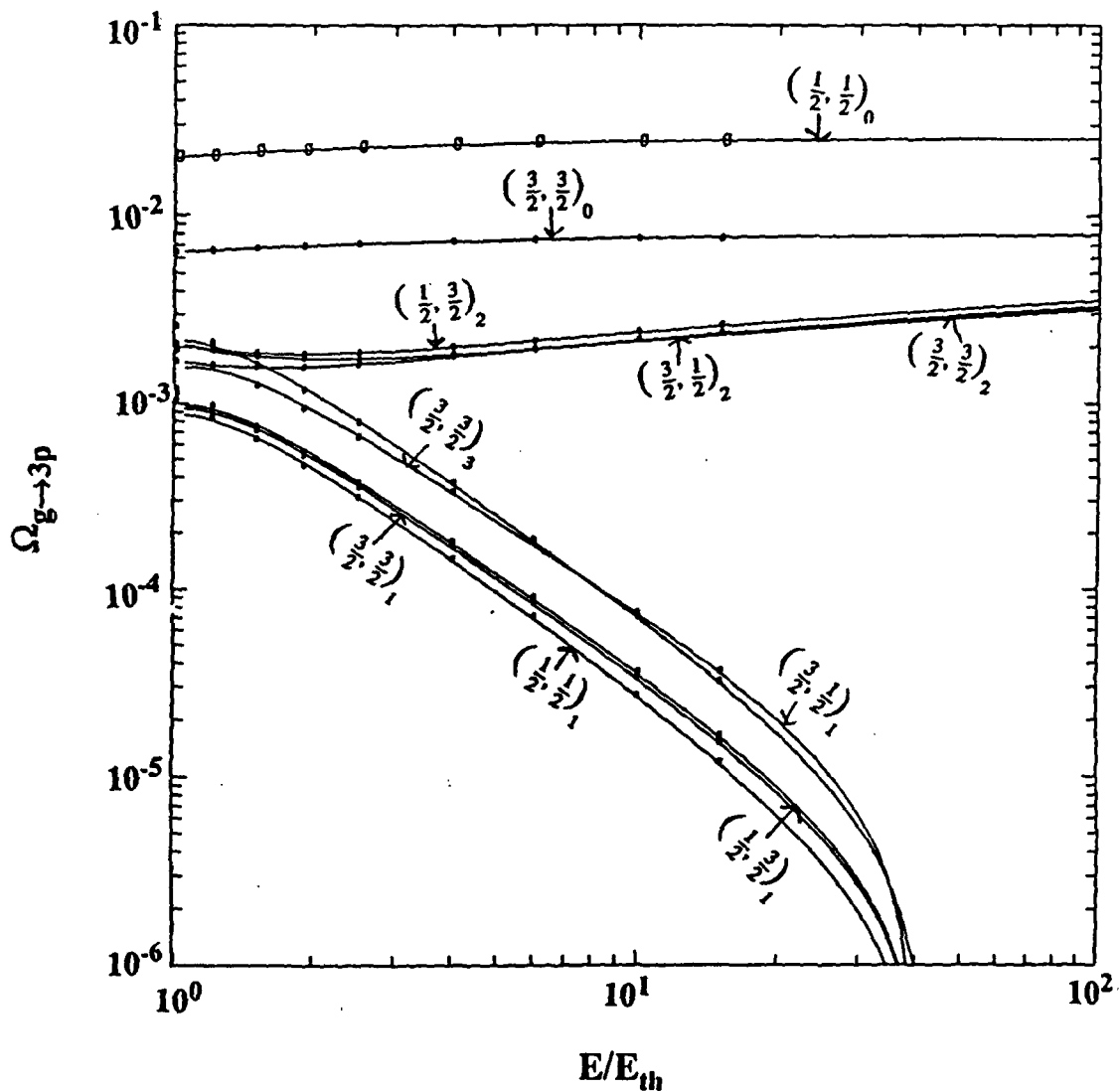


Fig. 3 Collision strengths of the ten 3p multiplet levels for excitation from the ground state of neon-like selenium as a function of electron energy relative to the threshold energy.

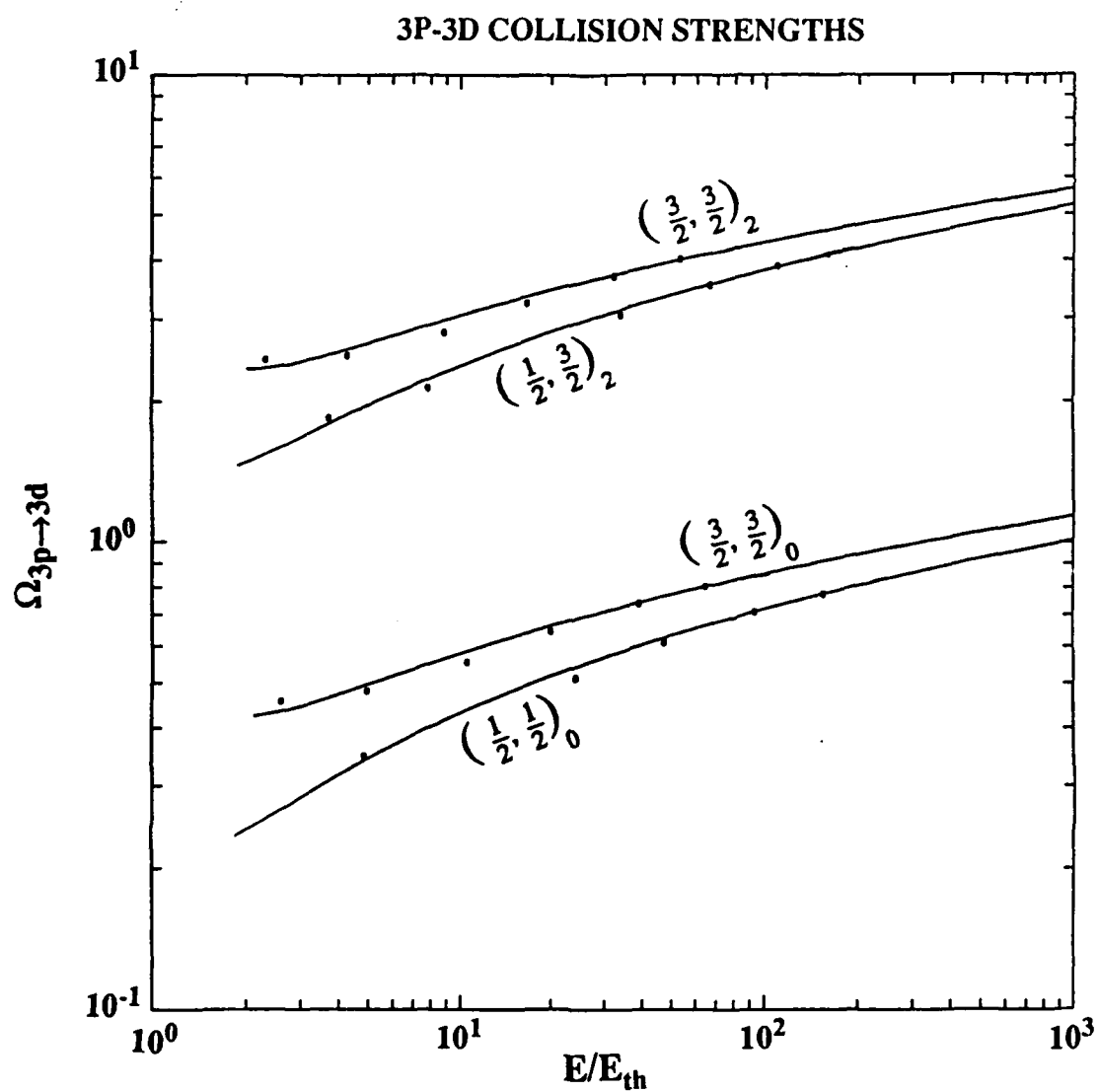


Fig. 4 Collision strengths of the important four excitations from the J=0 and J=2 levels of the 3p state to the 3d state.



DR RATE COEFFICIENTS TO UPPER AND LOWER LASING LEVELS

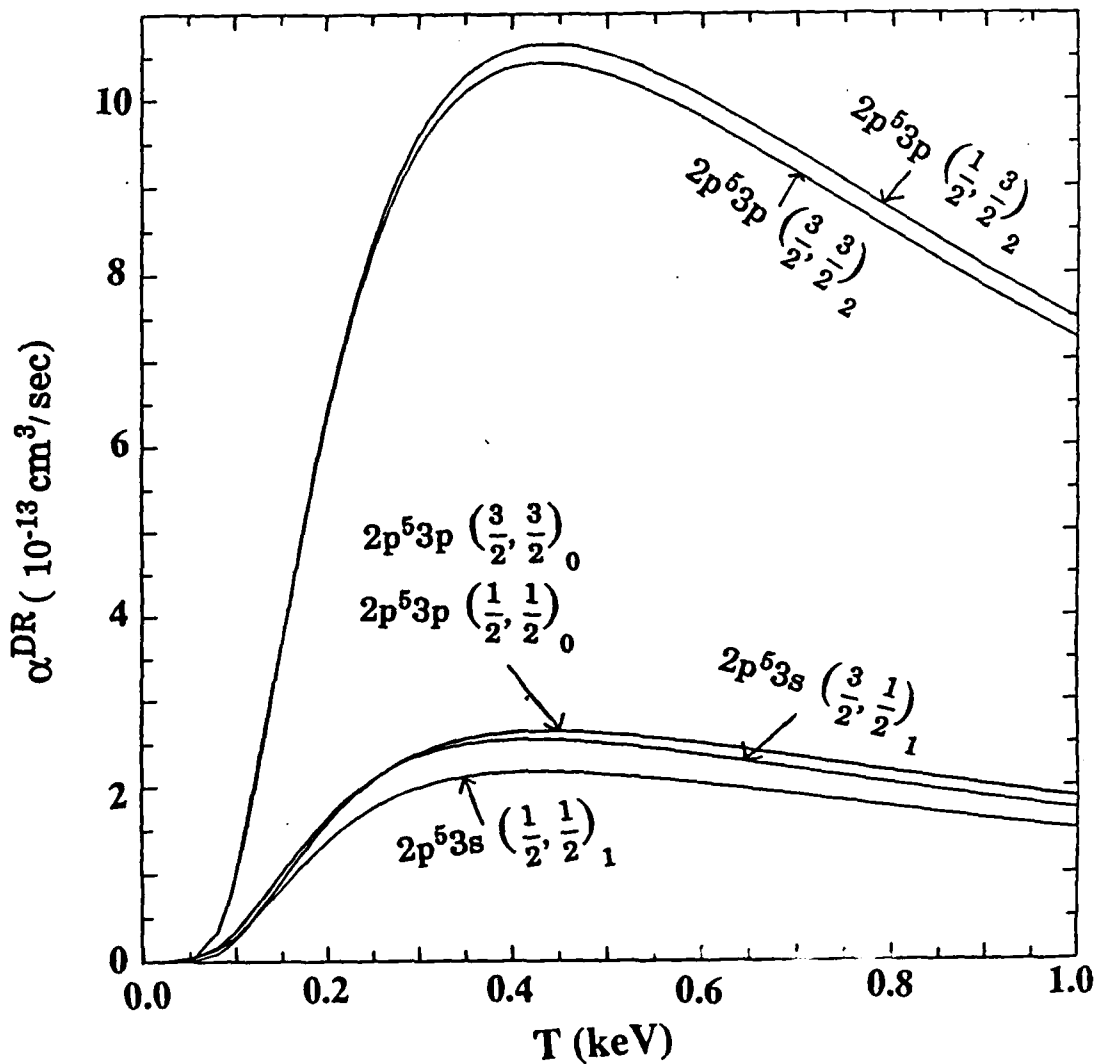


Fig. 6 Dielectronic recombination rate coefficients from the ground state of F-like selenium to the observed upper  $2p^5 3p$  and lower  $2p^5 3s$  lasing levels of Ne-like selenium.

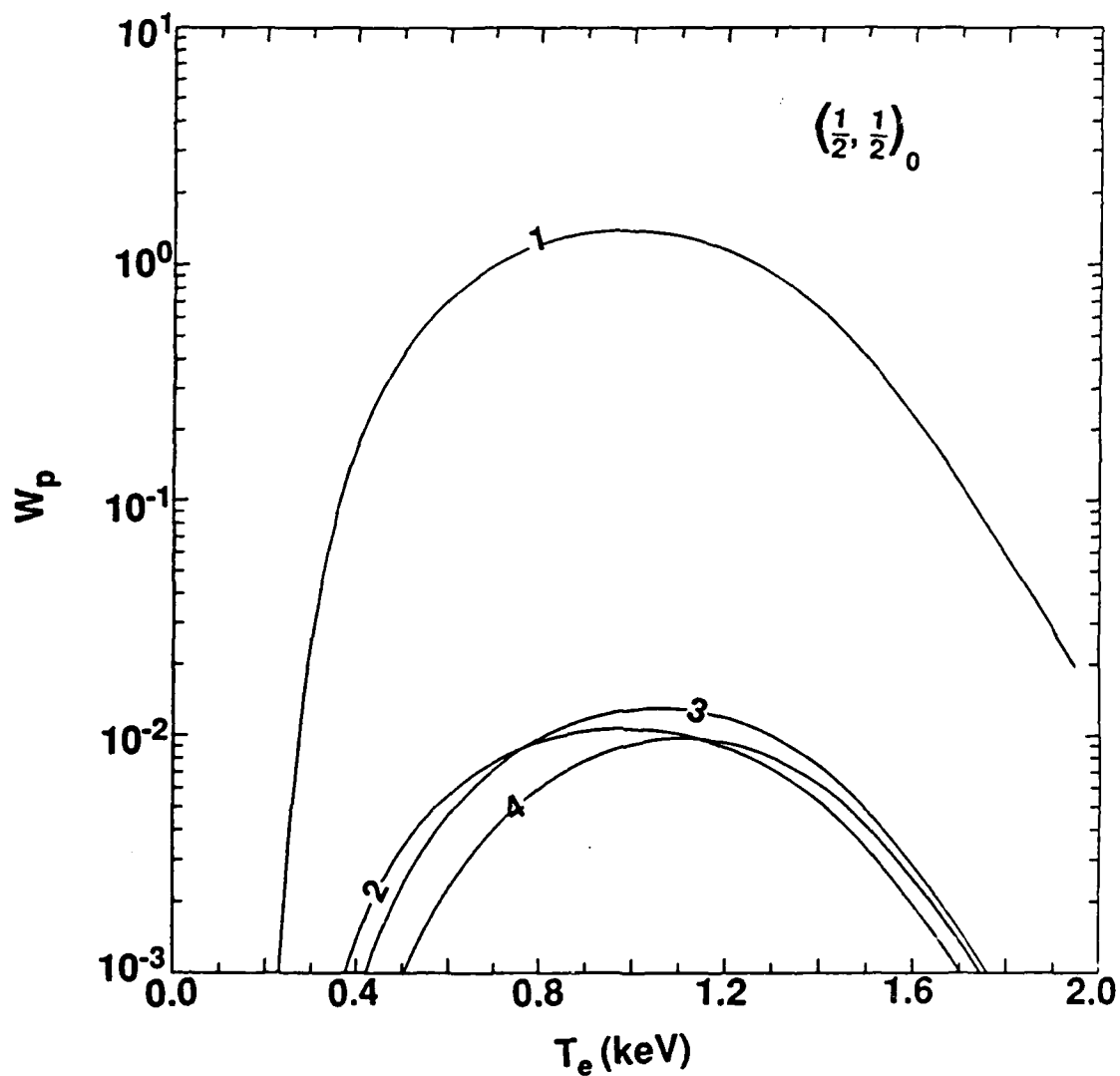


Fig. 7 Pumping rates of different processes populating the  $(1/2, 1/2)_{J=0}$  upper lasing level as a function of electron temperature. 1: collisional excitation (CE) from the neon-like ground state, 2: collisional deexcitation (CD) from the 3d excited state; 3: CD from the n=4 and excited inner shell states; 4: dielectronic recombination (DR) from the F-like ground state.

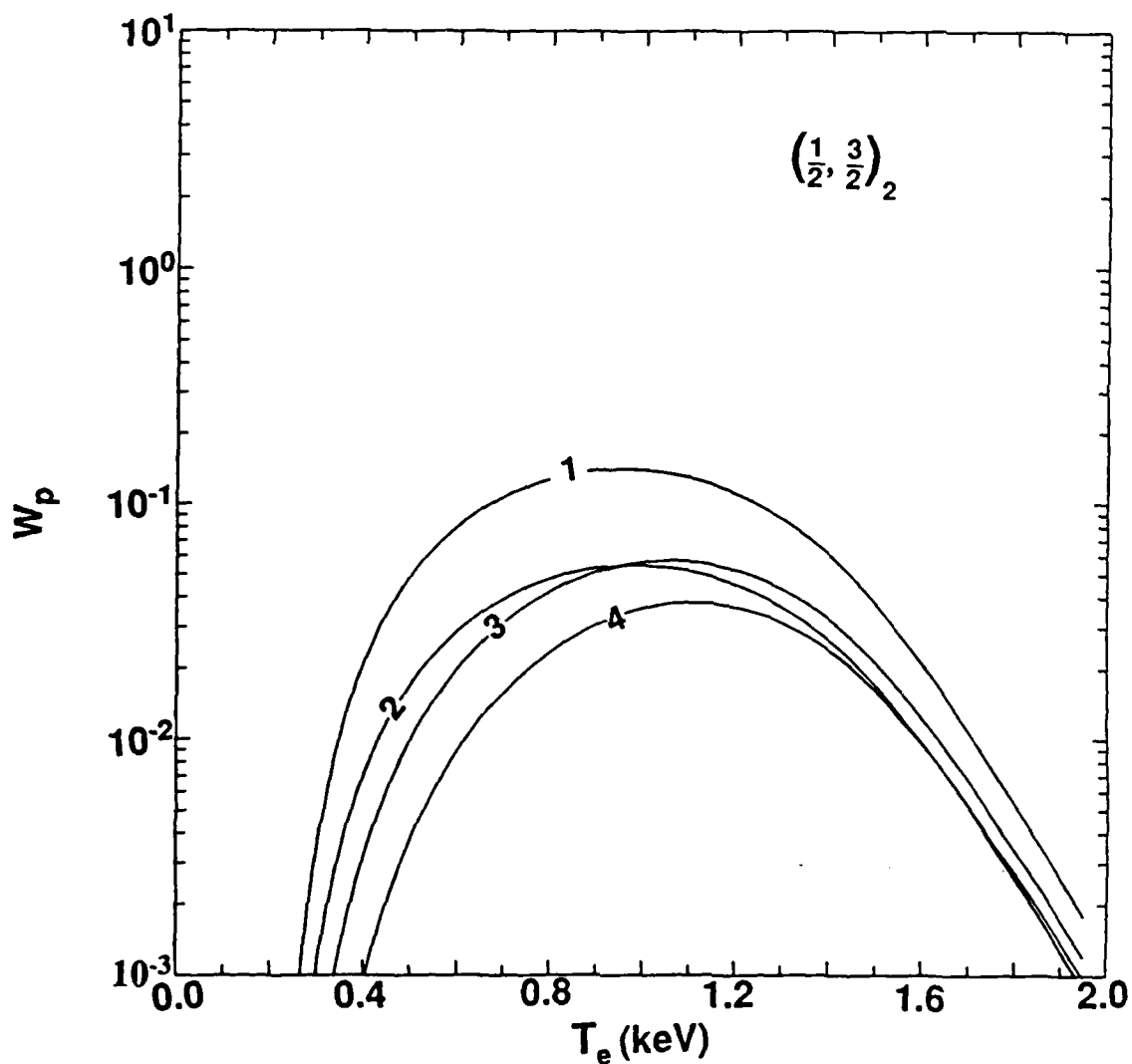


Fig. 8 Pumping rates of different processes populating the  $(1/2, 3/2)_{J=2}$  upper lasing level as a function of electron temperature. 1: collisional excitation (CE) from the neon-like ground state, 2: collisional deexcitation (CD) from the 3d excited state; 3: CD from the n=4 and excited inner shell states; 4: dielectronic recombination (DR) from the F-like ground state.

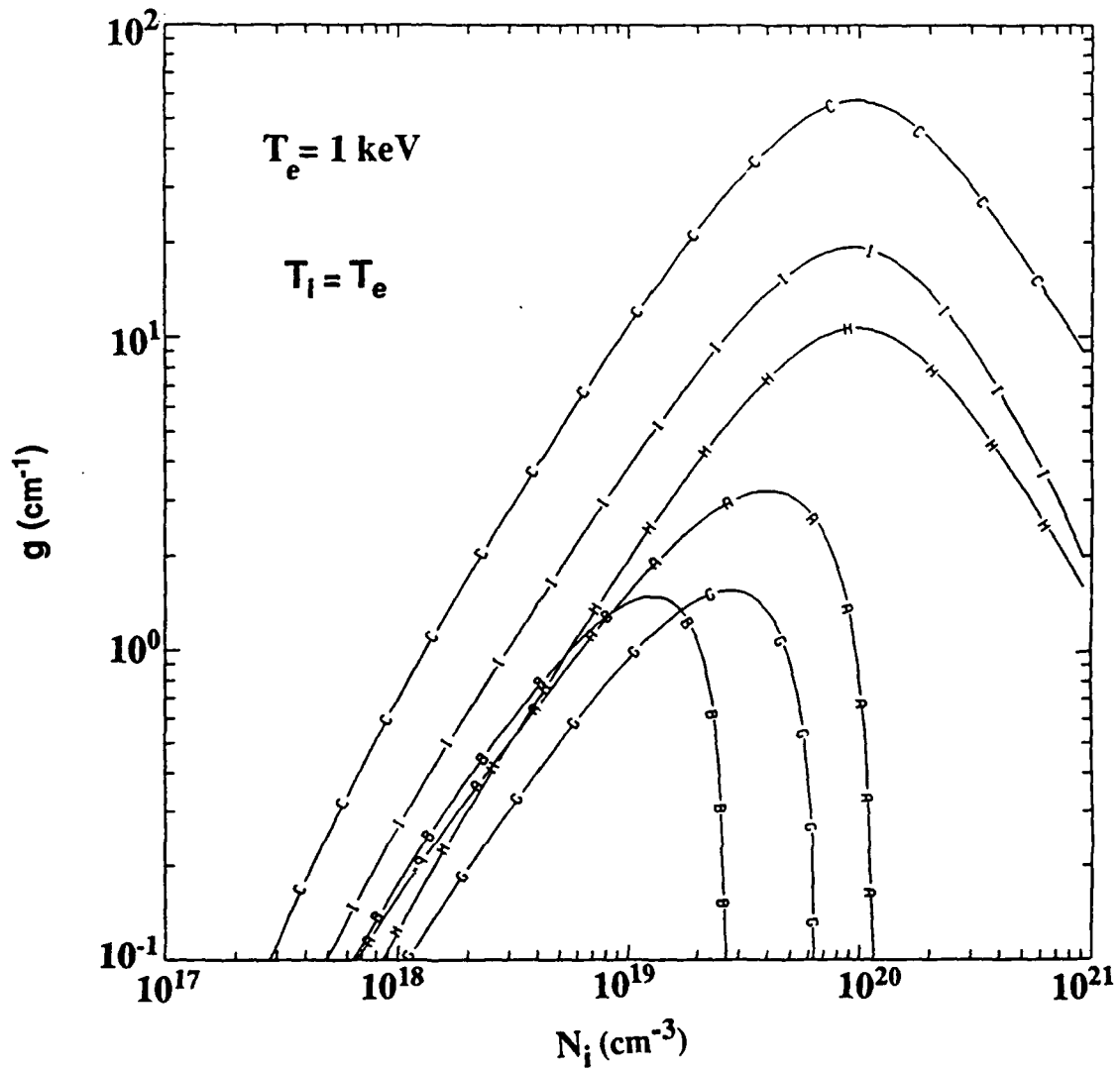


Fig. 9 Gain coefficients (in  $\text{cm}^{-1}$ ) of the most relevant  $2p^5 3p-2p^5 3s$  lasing transitions of neon-like selenium as a function of ion density. The identification of the curves corresponding to different lasing transitions are as indicated in Table I.

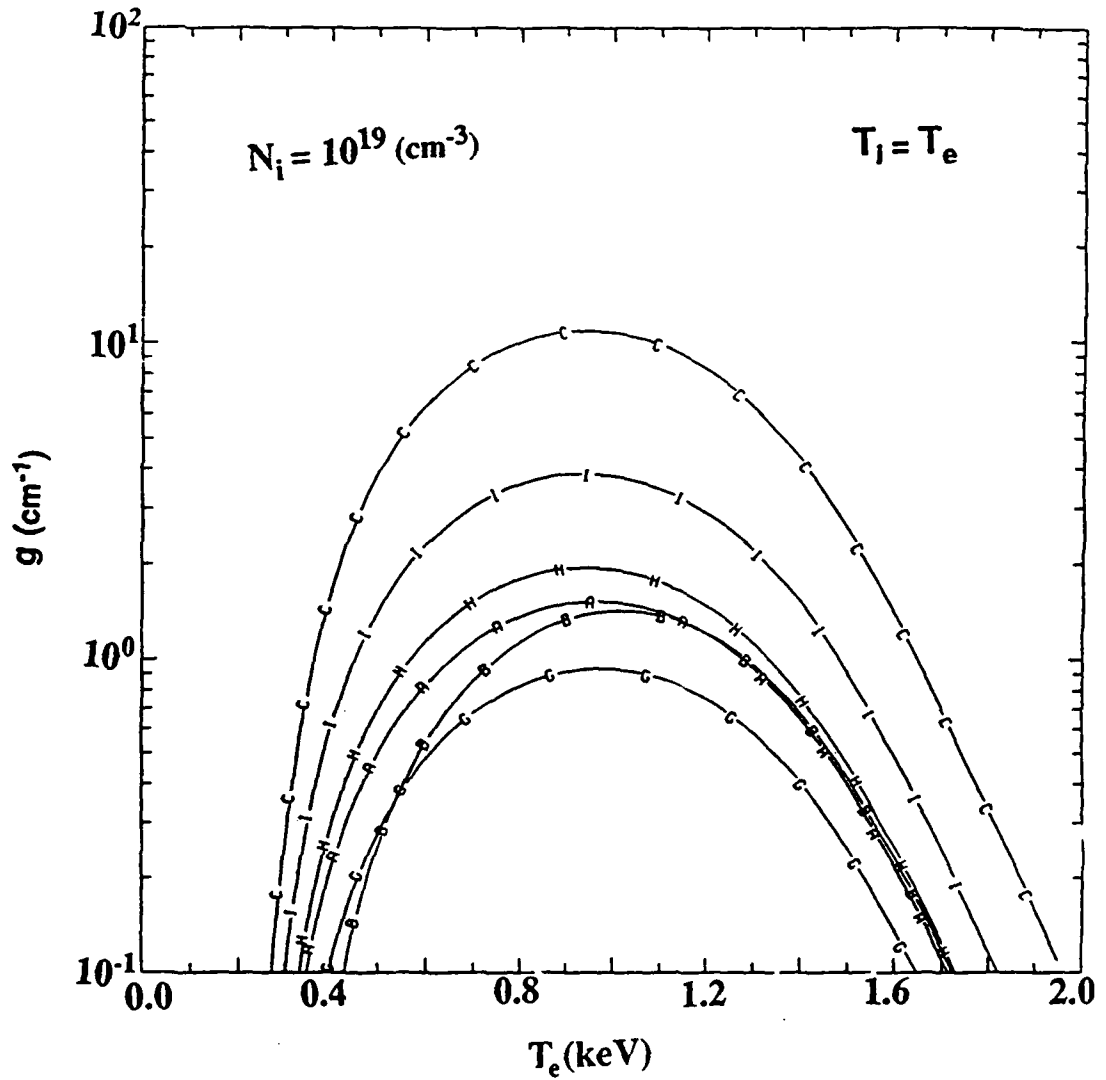


Fig. 10 Gain coefficients (in  $\text{cm}^{-1}$ ) of the six important  $2p^5 3p-2p^5 3s$  lasing transitions of neon-like selenium as a function of electron temperature. The curves are identified in Table I.

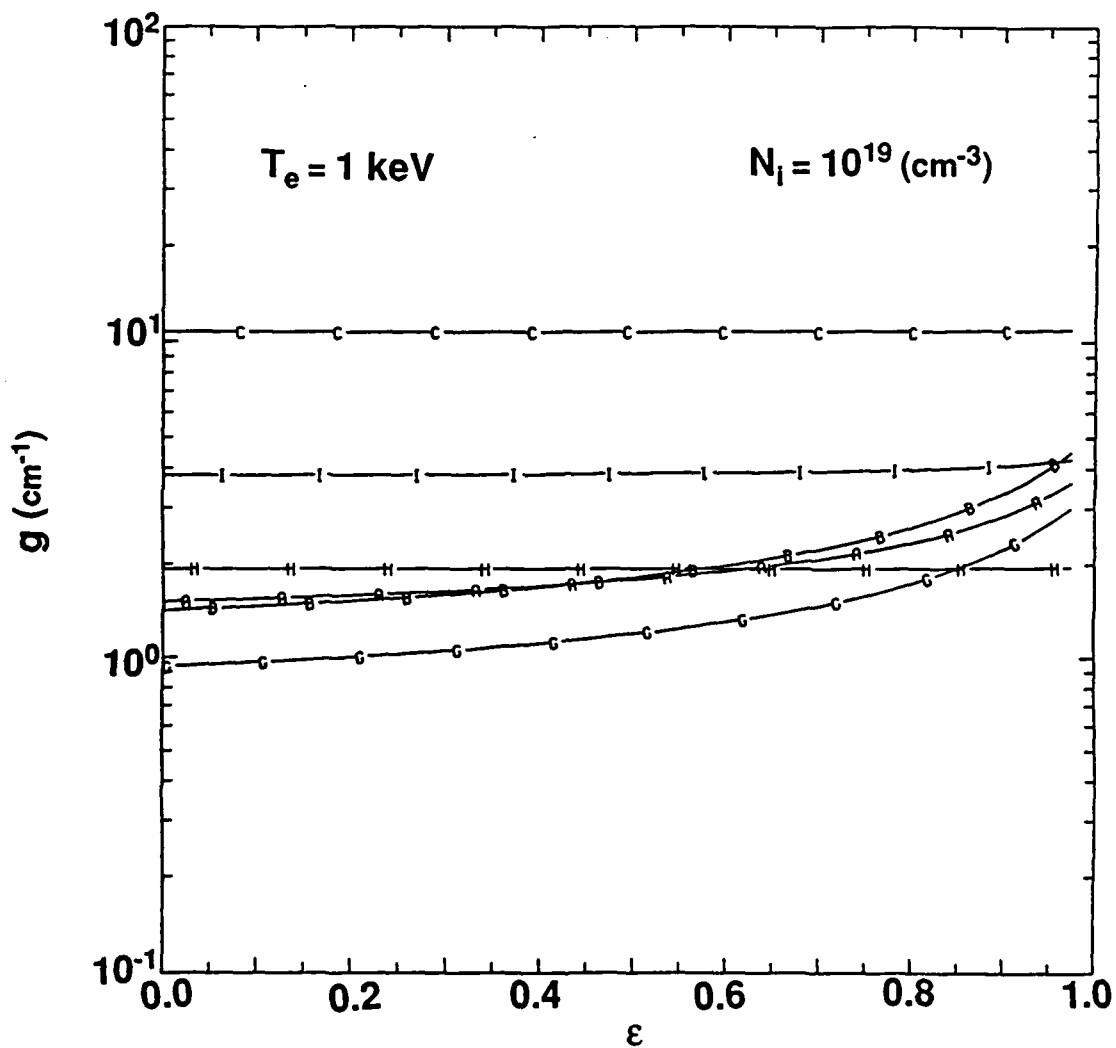


Fig. 11 Variation of gain coefficients (in  $\text{cm}^{-1}$ ) of all the six lasing lines as we increase the population of the 3d excited state by decreasing the radiative decay rate from this state to the ground state. As  $\epsilon$  varies from 0 to 1, the decay rate is decreased from its original value by a factor of 10.

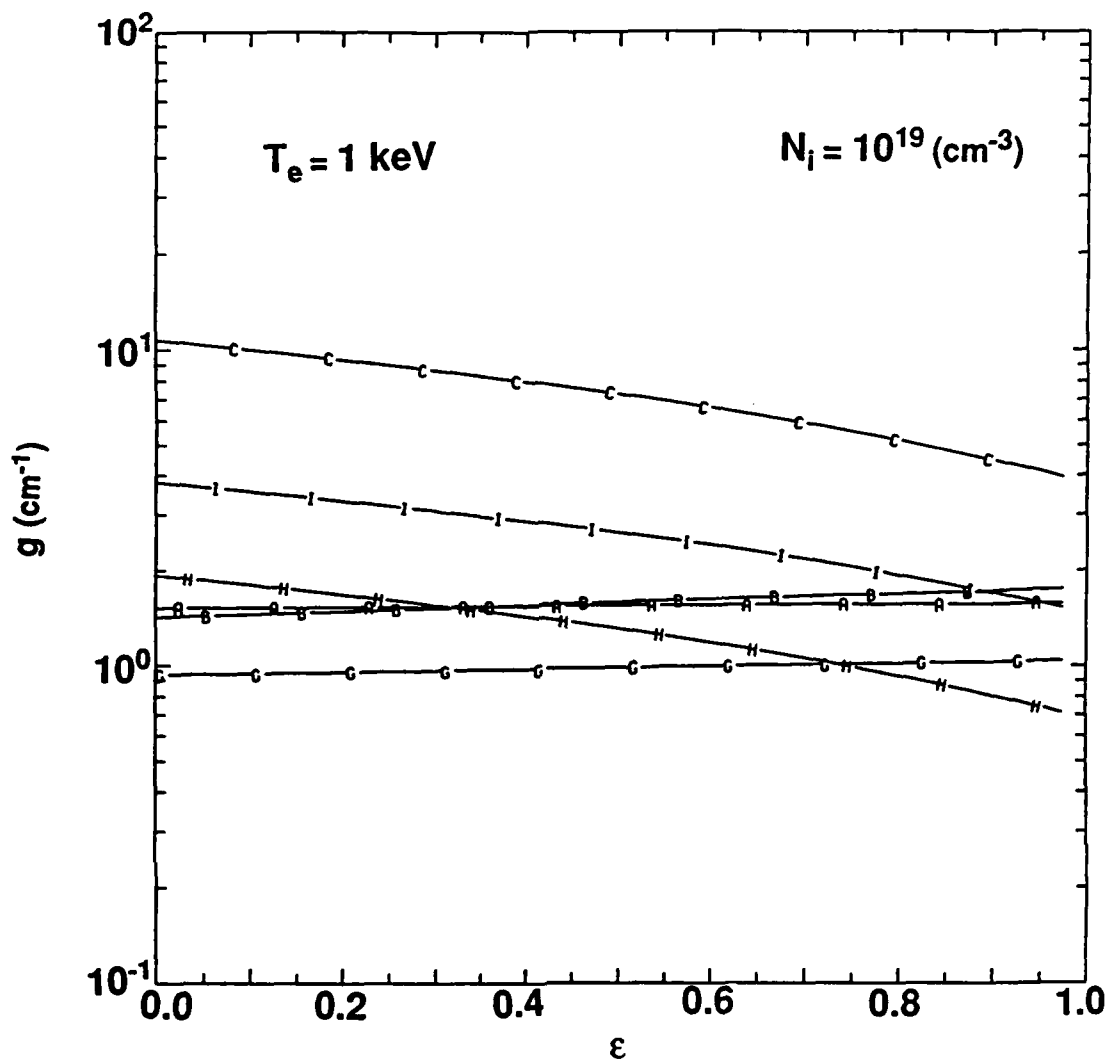


Fig. 12 Variation of gain coefficients (in  $\text{cm}^{-1}$ ) of all the six lasing lines as we decrease the excitation rates to the  $(1/2, 1/2)_{J=0}$  and  $(3/2, 3/2)_{J=0}$  levels from the ground state. As  $\epsilon$  varies from 0 to 1, the excitation rates decrease from their original values by a factor of 3.

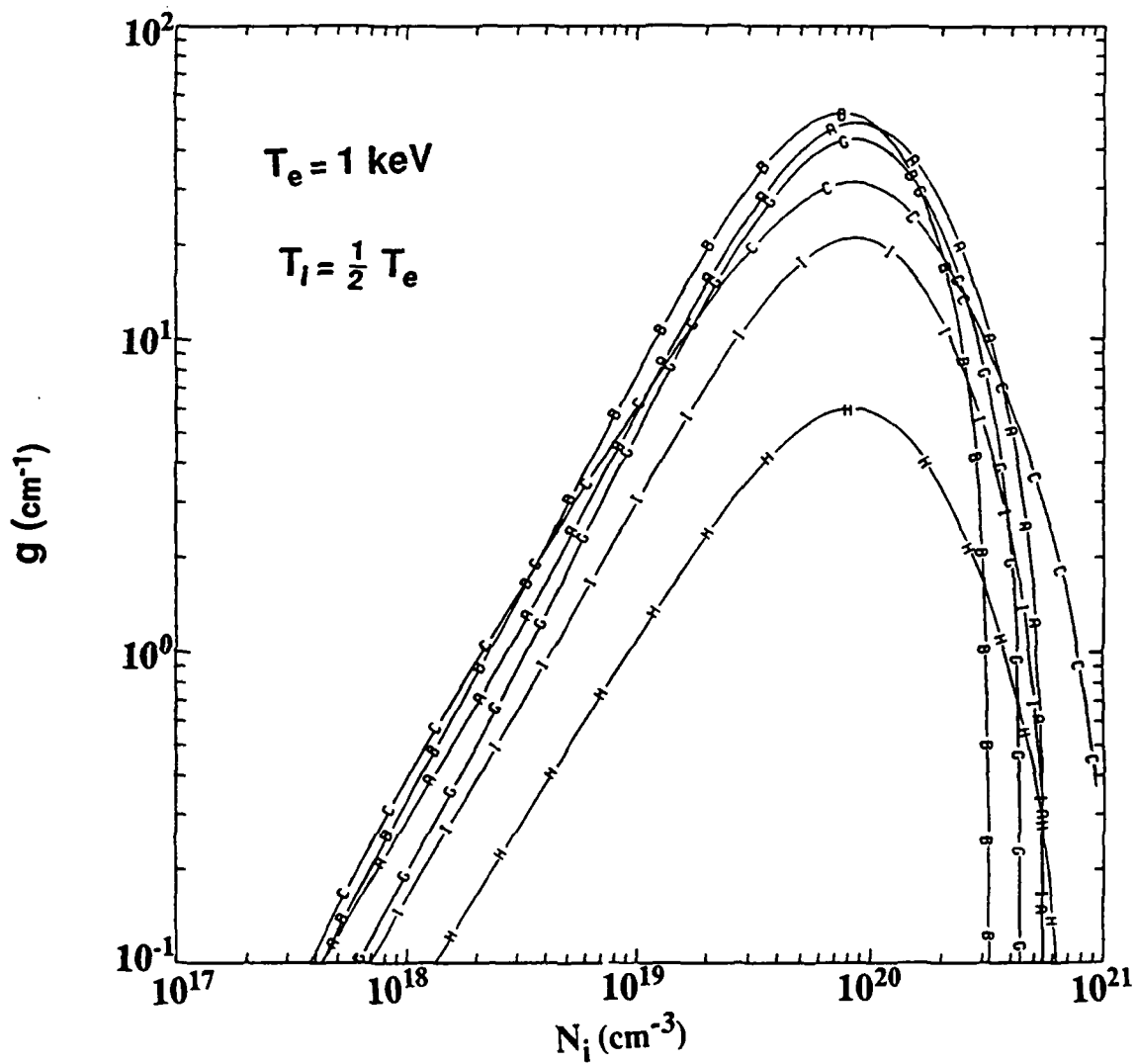


Fig. 13 Modified gain coefficients (in  $\text{cm}^{-1}$ ) of the lasing lines as a function of ion density. These new gain curves were obtained with the decay rate  $A_{g,3d}$  reduced by a factor of 10, the collisional excitation to the  $(1/2, 1/2)_{J=0}$  reduced by a factor of 3 and the CE to the  $(3/2, 3/2)_{J=0}$  level reduced by a factor of 2.

## REFERENCES

1. D. L. Matthews et al., Phys. Rev. Lett. 54, 110 (1985).
2. M. D. Rosen et al., Phys. Rev. Lett. 54, 106 (1985).
3. C. J. Keane et al., J. Phys. B., At. Mol. Opt. Phys. 22, 3343 (1989).
4. R. A. London, et al., J. Phys. B., At. Mol. Opt. Phys. 22, 3363 (1989).
5. B. J. MacGowan et al., J. Appl. Phys. 62, 5243 (1987).
6. T. N. Lee et al., Phys. Rev. Lett. 59, 1185 (1987).
7. T. N. Lee et al., Bull. Am. Phys. Soc. 33, 1920 (1988).
8. J. P. Apruzese et al., Phys. Rev. Lett. 55, 1877 (1987).
9. B. L. Whitten et al., Phys. Rev. A 33, 2171 (1986).
10. W. H. Goldstein et al., Phys. Rev. A 36, 3607 (1987).
11. C. J. Keane et al., Phys. Rev. A 42, 2327 (1990).
12. B. L. Whitten et al., J. Opt. Soc. Am. B5, 2537 (1988).
13. R. D. Cowan, 'The Theory of Atomic Structure and Spectra (Univ. California Press, Berkeley, 1981).

14. A. Dasgupta and K. G. Whitney, Phys. Rev. A 42, 2640 (1990).
15. R. D. Cowan, J. Phys. B 13, 1471 (1980).
16. H. Zhang et al., Atomic Data and Nuclear Data Tables 37, 17 (1987).
17. L. B. Golden et al., J. Phys. B 11 (1978).
18. D. L. Moores et al., J. Phys. B 13 385 (1980).
19. P. Hagelstein and R. K. Jung, Atomic data and Nuclear Data Tables 37,  
121 (1987).
20. M. C. Chen, Phys. Rev. A 34, 1079 (1986).
21. M. C. Chen, Phys. Rev. A 40, 2292 (1989).

Prospects for X-Ray Lasing in Ultra Short-Pulse  
Laser/Plasma Interactions

J. Davis\*, R. Clark\*, J. Les\*, D. Roelant<sup>+</sup>

Introduction

The idea of heating a plasma to high temperatures and densities and observing how it recombines has long been of interest as a possible means of creating a population inversion leading to gain in some of the hydrogen-, helium-, and lithium-like excited state transitions. Considerable effort both theoretically and experimentally has been devoted to explore the requirements necessary to generate plasma conditions conducive to producing inversion and gain. Static calculations based on ionization dynamic models using prescribed temperature and density profiles provides some measure of the systems ability to support inversion and gain but avoids the real issue of whether it is feasible to generate a plasma with the desired behavior ie, can the plasma cool fast enough for recombination to overpopulate the upper hydrogenlike levels on time scales short compared with other radiative and collisional processes. When the heating is due to the absorption of energy from an intense high powered laser beam interacting with a planar target the plasmas' primary cooling mechanisms are convection, conduction, and radiation. Numerical simulations suggest that the plasma cools primarily by expansion and radiation since conventional thermal conduction is too slow in redistributing the energy to create rapid changes in the temperature profile needed to support population inversions.

It has also been determined that free adiabatic expansion will cool the plasma faster than purely radiative cooling. Naturally, since both processes occur, the total cooling rate will be enhanced over free expansion. In addition, higher Z elements are more effective radiators than lower Z elements but because of their higher mass expand more slowly. Hence, to augment adiabatic cooling lower Z materials are more efficient. A detailed comparison of radiative and adiabatic cooling has been made by Thornhill, et. al.<sup>1</sup>

In this study we investigate the physics of an intense high powered subpicosecond laser pulse interacting with a planar fluorine target to determine the feasibility of creating a population inversion and gain in the 3-2 transition of hydrogenlike fluorine. The results are preliminary in the sense that the atomic model describing the ionization dynamics of the level populations is based on a limited number of excited states. All the ground states of neutral and ionized fluorine along with an excited state manifold containing all levels up to and including principal quantum number  $n=5$  are maintained. This limited number of excited levels cannot provide an adequate representation of the complete effects of recombination but can indicate trends and provide guidance on the feasibility of the proposed lasing scheme. In addition, a simple model is adopted to describe the blowoff plasma, i.e., after the self-consistent radiation hydrodynamics model is employed to produce the initial early time conditions generated by absorbing the laser energy, the plasma is assumed to undergo free adiabatic expansion. The motivation for this assumption is that if inversion and gain are to occur, they most likely will occur under these conditions. We

will perform more complete numerical simulations using a fuller model in a forthcoming study.

## Results and Discussion

Preliminary calculations have been performed describing the evolution and behavior of a laser generated plasma produced by a KrF 600 fs laser pulse with an intensity of  $3 \times 10^{16}$  watts/cm<sup>2</sup> incident on a planar fluorine slab. The laser energy is assumed to be absorbed by the target by inverse bremsstrahlung at the critical surface and then deposited in a skin depth of about 200 angstroms. The results are based on numerical simulations using a fully selfconsistent 1-D non-LTE radiation hydrodynamics model<sup>2</sup> to generate the initial plasma conditions. After the initial plasma forms the blowoff plasma is then represented by free adiabatic expansion in the absence of radiative cooling. The log of the mass density (g/cc) is shown as a function of position and time in Fig.1. This density history is obtained from the full radiation hydrodynamics model. The position of the initial surface of the slab is located at 5 microns. As the slab plasma heats and ablates, a low density blowoff is formed while a shock wave is produced and propagates into the slab. The shock can be seen in the upper left corner of the figure. Even on a time scale comparable to this very short laser pulse there is considerable motion. The variation of temperature with time and distance as predicted from the full model during the early phases of the heating and expansion is shown in Fig.2. The dotted curve shows the outer edge of the ablating plasma. Temperatures of about 2 keV are achieved over a fairly broad range of plasma extending from nearly solid density to the outer edge of the expansion. In

Fig.3 the log of the mass density is shown as a function of time and position for an adiabatic expansion. A solid density fluorine slab at an initial temperature of 2 keV is allowed to expand in an adiabatic fashion, ie the adiabatic solution is imposed. The solution is shown for times between 2.4 and 4.0 ps. It will become apparent from the calculations that densities of about  $10^{-3}$  of solid must be reached before population inversion and gain can be achieved. The population of the  $n=3$  state of hydrogenic fluorine is shown as a function of temperature and mass density in Fig. 4. The plasma, initially in equilibrium at  $T=2$  keV was cooled ( at a linear rate ) to the value  $T=4-1000$  eV, respectively as the plasma density was held fixed. Various timescales for the cooling were experimented with, but the results were relatively insensitive over a range of 1 to 100 ps. This situation arises because of an almost unlimited supply of long-lived fully ionized fluorine. The population inversion of the 3-2 levels in hydrogenic fluorine is shown in Fig. 5 as a function of temperature and density. The inversion was obtained at fairly low densities, ie around  $10^{-3}$  solid at temperatures less than about 400 eV. Inversions of 1.8 are achieved over the parameter space shown. The dotted contours reflect population ratios (  $f_u g_1 / f_l g_u$  ) that are less than unity, i.e., not inverted. Finally, the calculated gain in the 3-2 transition is shown as a function of temperature and density in Fig.6. The dotted counters represent negative values of gain, ie opacity. The gain is confined to a narrow region of the figure which is dominated by low temperatures and densities. The main conclusion is that it is feasible to obtain gain in the 3-2 transition provided the plasma can evolve to the desired conditions. Also, since we convinced ourselves that inversion and gain can be

achieved under ideal conditions, we are currently in the process of expanding and incorporating the expanded atomic model into the non-LTE radiation hydrodynamics model and are preparing to perform numerical simulations to map out the inversion and gain parameter space.

#### Acknowledgements

This work was supported by SDIO/T/IS.

#### References

\* Radiation Hydrodynamics Branch, Naval Research Laboratory  
Washington, D.C. 20375

+ Berkeley Scholars, P.O.Box 852, Springfield, Va. 22150

1. Thornhill, J.W., Apruzese, J. Giuliani, and Roelant, J. Appl. Phys. 68, 33 (1990).

2. Duston, D., Clark, R., and Davis, J., Phys Rev A 31, (1985).

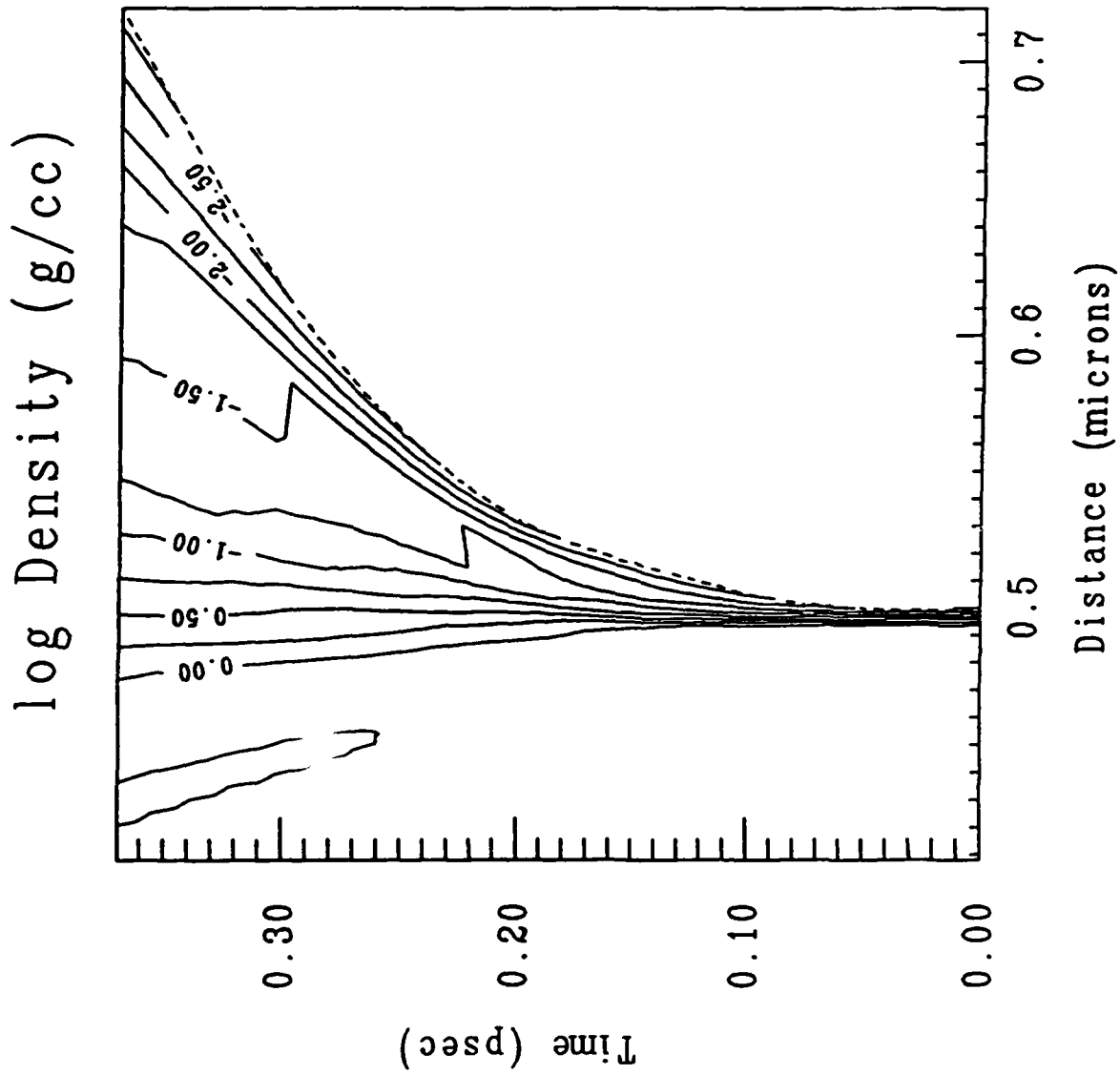


Figure 1: Mass density as a function of position ( $\mu$ ) and time (ps). Full radiation hydrodynamic model. Initial edge of slab is at  $5\mu$ .

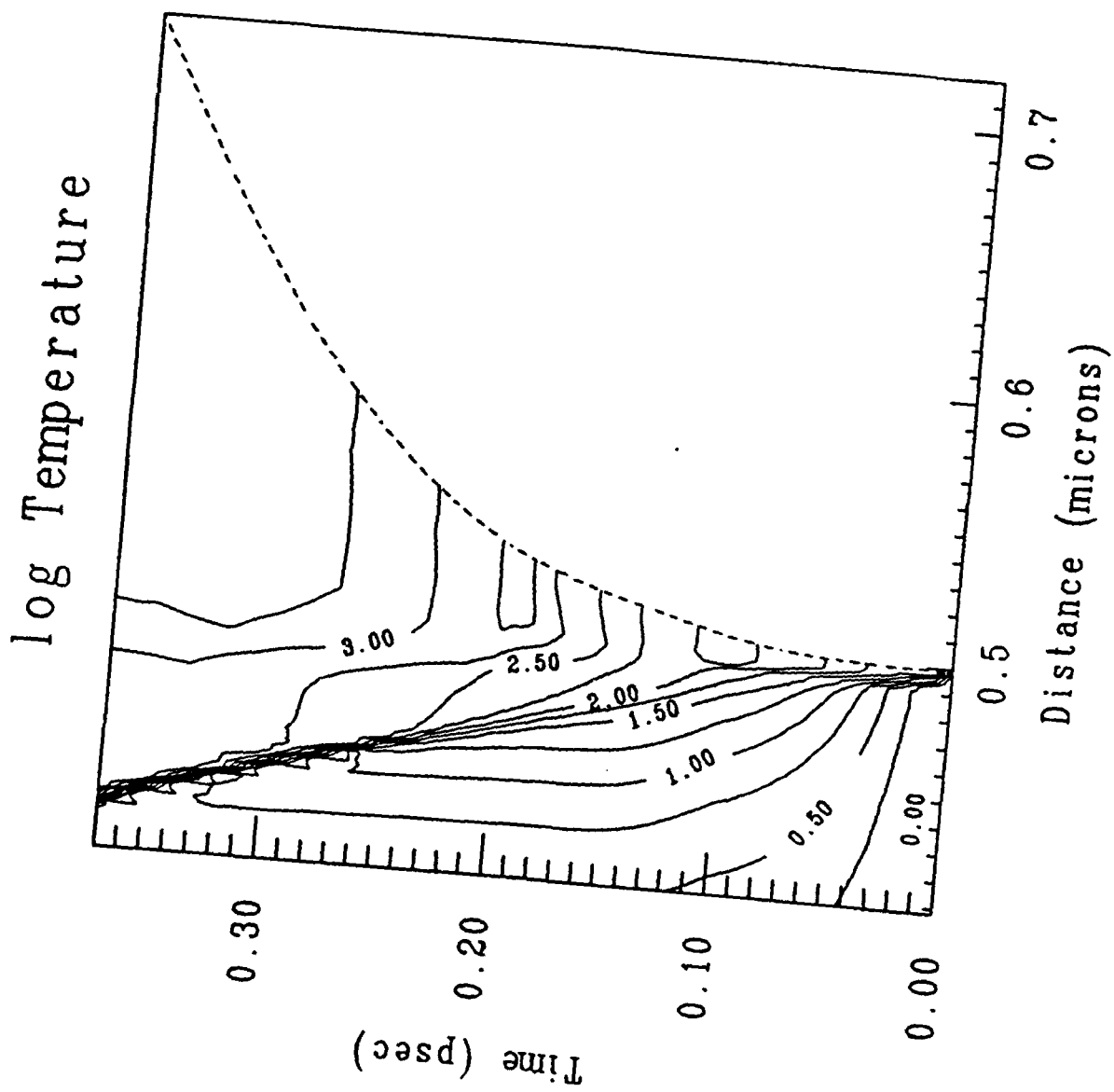


Figure 2: Temperature as a function of position and time. Full model.

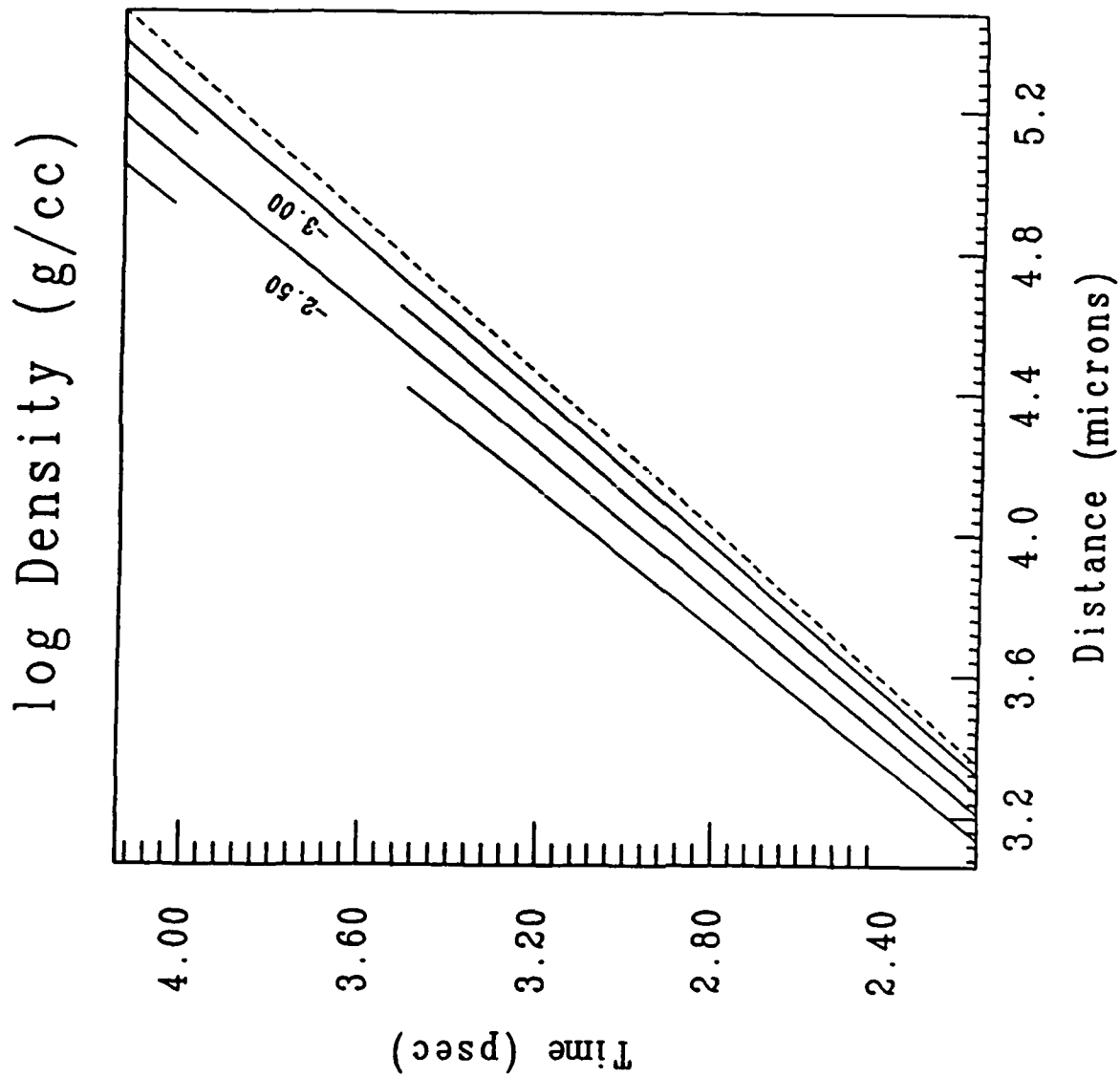


Figure 3: Density as a function of position and time for an adiabatic expansion. Results shown for  $t=2.4-4.0$  ps.

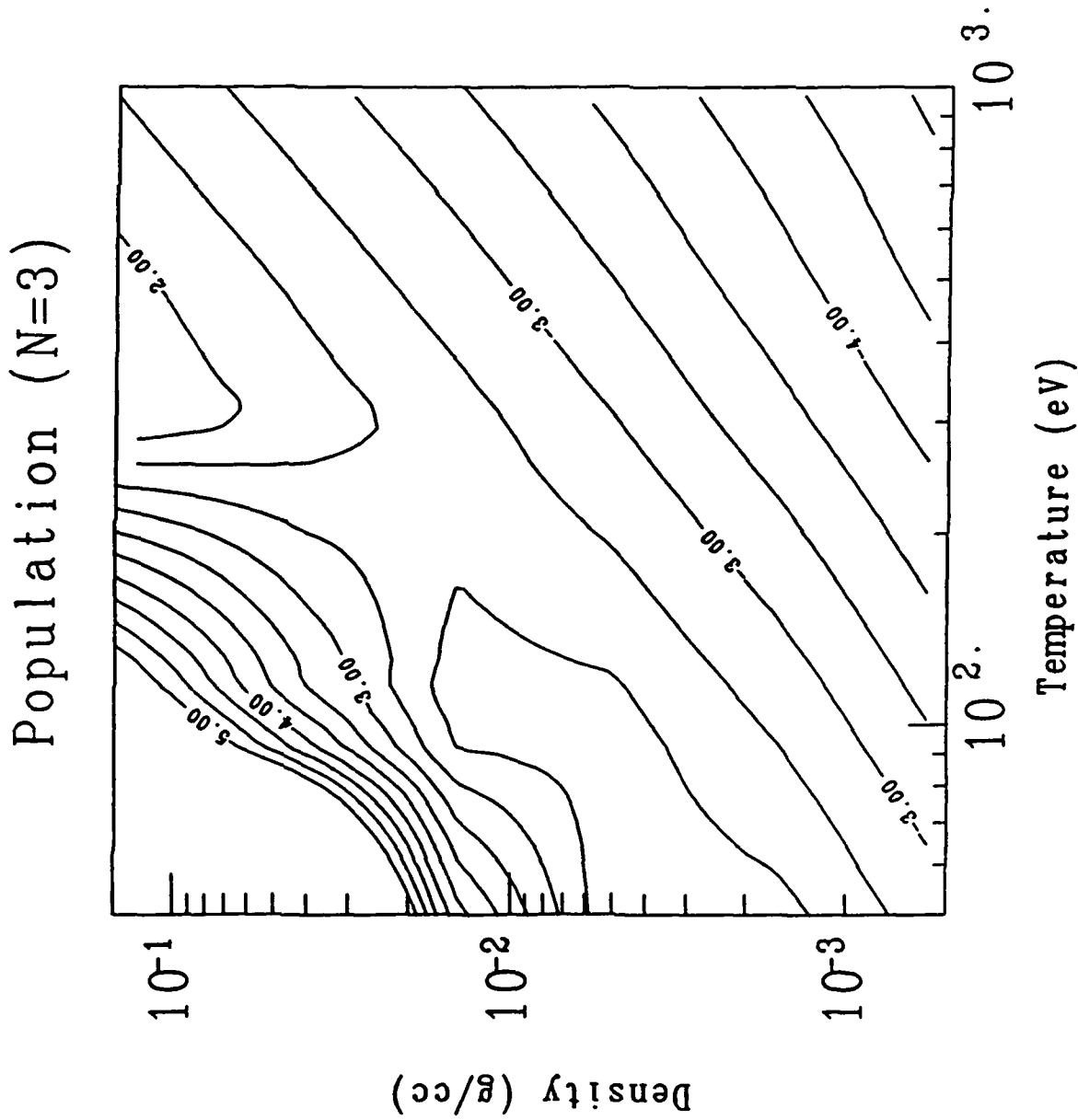


Figure 4: Population of H-like  $n=3$  state as a function of temperature and density. Results obtained parametrically for a linear temperature profile starting at 2 keV and falling to temperatures shown for times between 1 to 100 ps.

# Inversion (3-2)

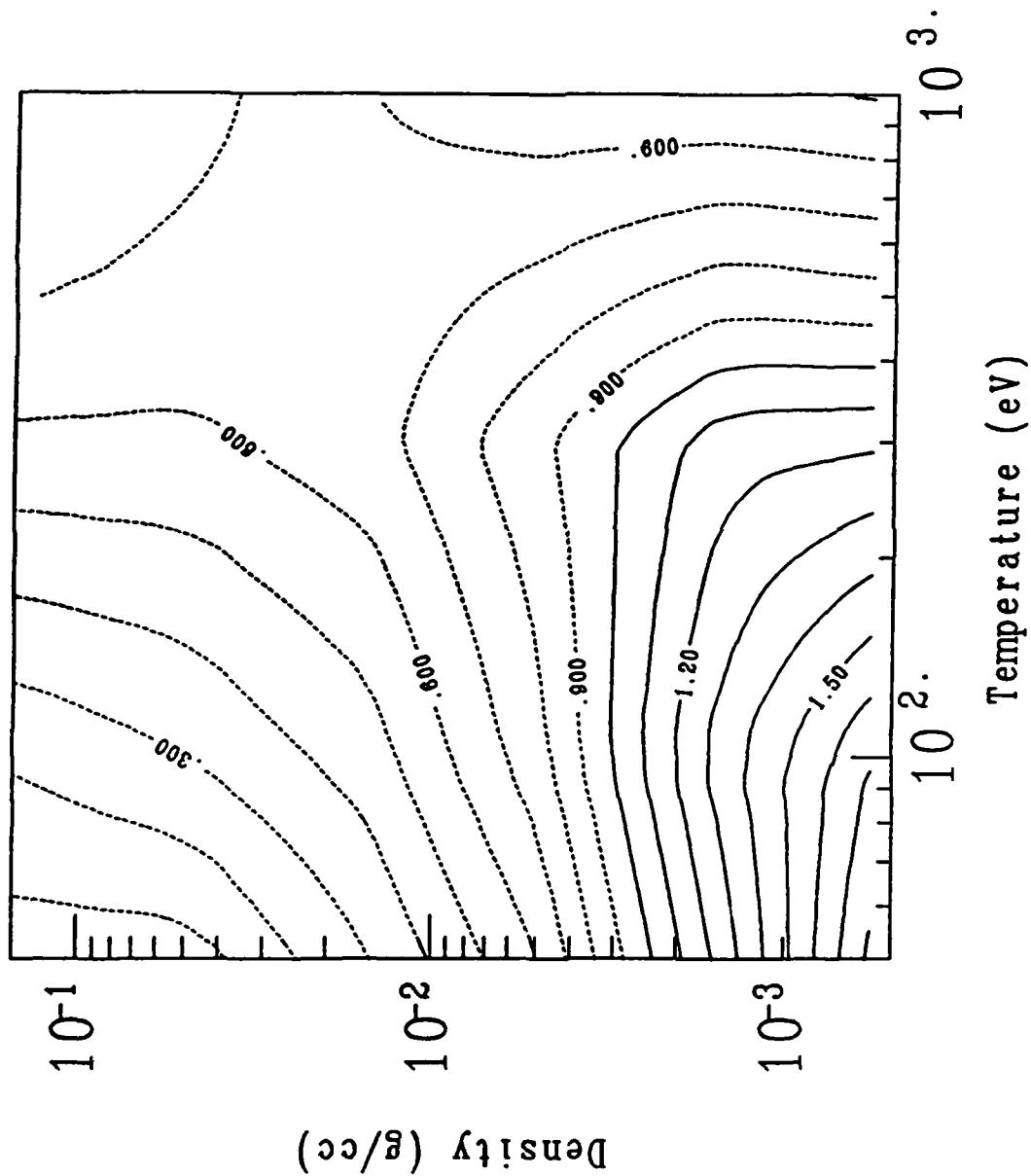


Figure 5: Population inversion of the  $n=3$  to  $n=2$  states in H-like fluorine as a function of temperature and density. Dotted (....) contours reflect ratios less than unity.

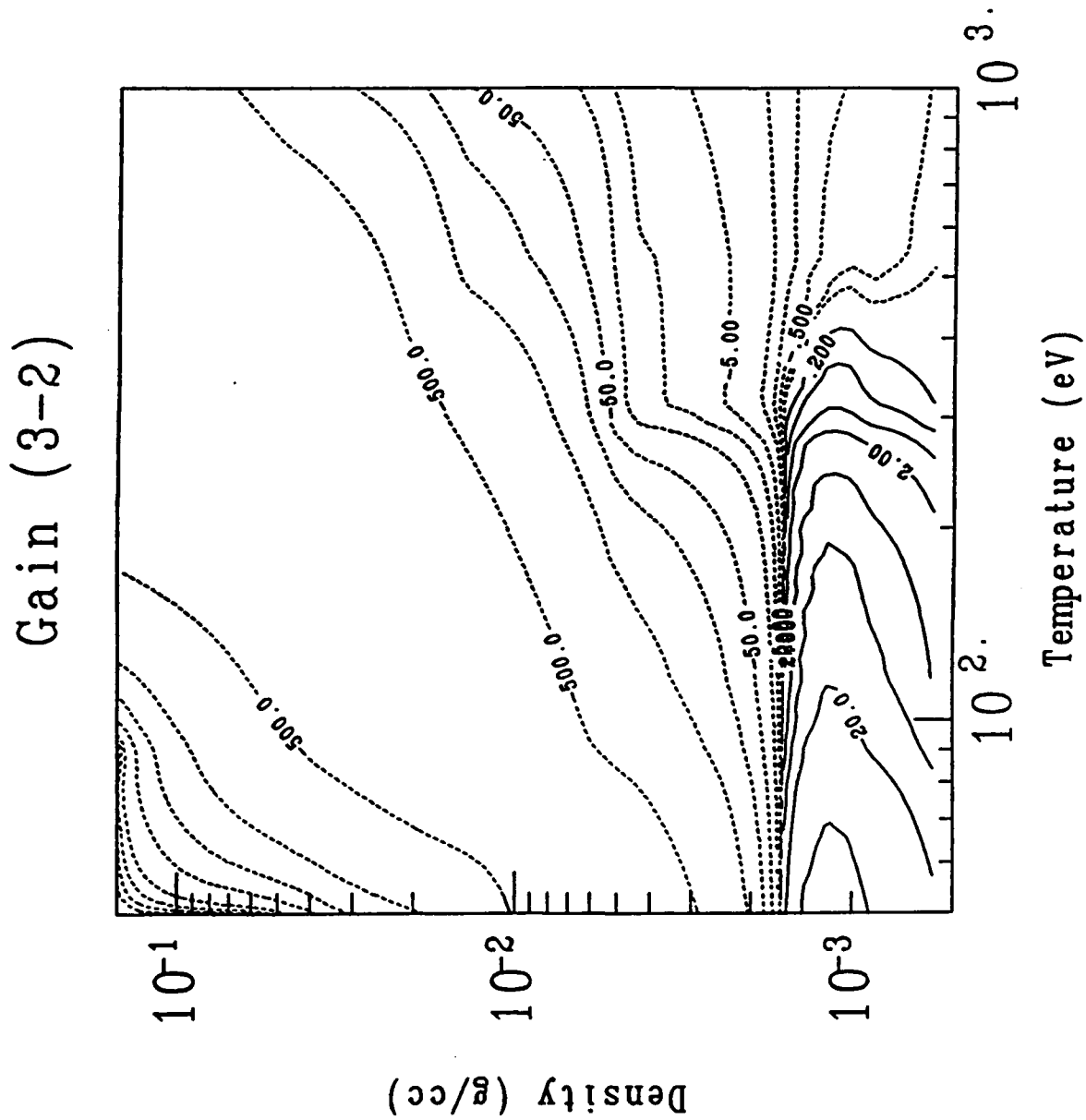


Figure 6: Gain in the  $n=3$  to  $n=2$  transition of H-like fluorine as a function of temperature and density. Dotted profiles indicate opacity.